Turning a Length of Oil Absorbent
A Numerical Simulation

N.J. van der Kolk

Delft University of Technology

TU Delft Delft University of Technology

Challenge the future

Turning a Length of Oil Absorbent
A Numerical Simulation

By

N.J. van der Kolk

in partial fulfilment of the requirements for the degree of

Master of Science
in Marine Technology

at the Delft University of Technology,
to be defended publicly on Thursday September 25, 2014 at 4:30 PM.

Supervisor:	Prof.dr.ir. R.H.M Huijsmans
Thesis committee:	Prof.ir. J.J. Hopman
	Dr.ir. J.A. Keuning
	Ir. P. Naaijen

TU Delft Delft University of Technology

This research was made possible by the financial support of the Ship hydromechanics department. I am grateful for the opportunity to pursue an academic thesis subject at the University. I thank the staff of the towing tank for their assistance in designing and carrying out the open water experiment. Finally, I have had the pleasure of working closely with Cesar and Etienne of the Protei group and I am grateful for all their effort.

On a more personal note, I would like to thank my aunt Baj and my uncles Bart Jan and Andrew for taking me in during the holidays, and my whole family for their support during this study.

N.J. van der Kolk
Delft, September 2014

Contents

1

Introduction

“Even the best safety efforts cannot prevent occasional oil spill accidents on the sea.” [1]

The work presented here it is in support of a novel method for oil-spill cleanup. An autonomous sailboat is envisioned sailing back and forth across an oil slick while towing a long segment of oil-absorbent material. In order to remain on the slick, the vessel will need to be able to execute turns of approximately 180 degrees. The behavior of the towed oil absorbent during these turns is the focus of this thesis. The tow force profile during such a turn and the absorbent track are essential design parameters.

Problem Statement

Investigate the physical process of towing oil absorbent through a turn. Develop a dynamical model that can faithfully reproduce the behavior. Perform a numerical implementation of the derived equations of motion and use this simulation to assess the feasibility of the Protei concept.

Outline

The absorbent will be modeled as a cable system using the lumped parameter technique. This amounts to performing the spatial discretization before formulating the system equations. The numerical modeling of towed cable systems received study in the field of oceanography. Existing studies for submerged cables are of limited applicability because the present system floats on the surface. Cable systems present modeling challenges. For example a chief material characteristic is the inability to support compressive loads. It is assumed that cable tension remains nonnegative during the u-turn maneuver. The equations of motion are derived using Kane's method. This is a modern approach to dynamics that seamlessly integrates constraint forces. Fluid forces are determined using the Morrison drag formula, using coefficients derived from a short series of open-water experiemnts.

Equations for the internal tension are derived to verify that the assumption for compression is respected. Other numerical properties of the system are examined, including the influence of controller gain, geometric scaling, and spatial discretization. A stability requirement is determined by inspection. System response is tuned using results from the experiments. Simulation results are presented to demonstrate the capabilities of the model. Characteristics of the absorbent system during a turn are detailed using the time evolution of system variables, as well as variations in system response for the parameter L/r.

Some time was devoted to evaluating the Protei vessel, a bio-inspired concept, and research findings are summarized for the interested reader. Recognizing that the Protei vessel is in the prototyping phase, a brief design exercise was carried out to develop a placeholder vessel with maximum driving force and maneuvering capabilities to cope with the absorbent. It will be used to arrive at a hypothetical sail-driving force for input to the numerical model. The feasibility of the Protei concept is assessed using the towing force profile of the placeholder vessel. A maximum length for the oil absorbent is calculated.

Oil Spills and Oil Spill Remediation Techniques

There are many examples of marine oil spills all over the world. The effect of any oil spill or leak is highly detrimental to the marine environment and marine economy. In case of a spill, the responsible party is liable for the costs of remediation and possibly the cost of any damages.

The process of spreading will form a round spill in the absence of wind or current, with heavy, thick oil at the center and a thin slick extending over the surrounding area. The slick is continuous until a terminal thickness is reached and then it will break into patches. The terminal thickness is related to the viscosity of the oil and may be between 0.1 and 8 mm. It has been observed that oil surfacing from a subsea blowout in large buoyant plumes will generate a film that may be 10 times thinner than those formed by surface leaks. In the presence of wind or current forces, the slick will take a roughly ellipsoidal elongated shape. Two-dimensional models of the water surface are accurate for light wind conditions without breaking waves, and predict that an offshore oil slick will drift at approximately 3.5% of the wind speed. For higher wind speeds, oil will be dispersed into the water column. In some examples oil which is entrained in the water column is transported directly against the wind. A layer of oil spread thinly on the surface will be subject to chemical and mass transfer processes known as weathering. Evaporation and emulsification, where the oil properties (viscosity, density) are dramatically affected by changing water content, are key to assessing the lifetime of a spill. Also, oil mass is gradually dispersed into the water column at a rate that depends on the sea state.

1.1 Oil Absorbent Segment

The average cost of cleaning a crude oil spill is €2,000 per barrel [2]. The available remediation techniques include physical removal, use of chemical agents such as dispersants and solidifiers, controlled burning, and bioremediation. The properties of a specific spill, such as the quantity of oil, the weather conditions, and the surrounding environment will determine which approach is best. Generally speaking, each method will come with adverse effects on the environment and a trade-off is made between the effects of an oil spill and the side effects of the cleanup operation. This is encapsulated in the net environmental benefit metric. For example, it is the conclusion of a report by Dave and Ghaly [2] that chemical dispersants are the most effective remediation technique, but these authors acknowledge that the long-term impact of these chemicals on the ecosystem is unknown. Difficulty with the proper disposal of oil-laden absorbent is identified as a detractor.

Protei Concept

The Protei autonomous sailboat is being developed by an international collaboration in response to difficulties encountered in oil spill clean-up, where efforts to remove a thin slick from vast stretches of the sea have proven lacking and hazardous for human operators. The Protei is envisioned sailing back and forth across the oil slick while towing a long segment of oil-absorbent material. By traversing the slick perpendicular to the wind direction, oil at the surface will be carried into the absorbent material. Several Protei may be deployed in a swarm so that large stretches of sea can be swept quickly. The Protei system is not intended to replace existing mechanical techniques such as oil containment booms and skimming. The Protei is intended for situations where the risk to human operators is high or where the physical extent of the slick is so great that existing methods would be ineffectual.

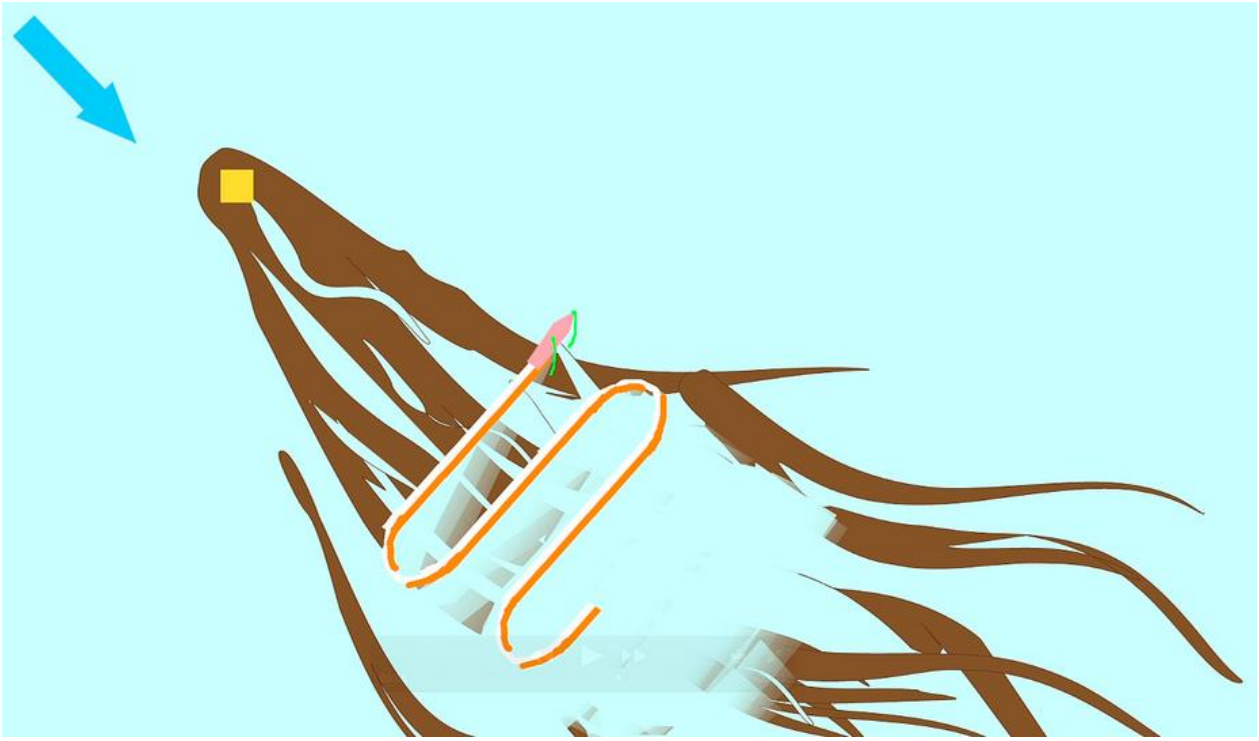

1.2 Protei Concept

The Protei vessel will sail long legs across the oil slick, performing large, sweeping turns while towing a length of oil absorbent. The amount of resistance generated by the oil absorbent is not clear, nor is the path followed by oil absorbent during the approximately 180 degree turns. This is a great unknown for the Protei design effort.

Roughly speaking, during a turn there will be a balance between the internal, cable-like tension caused by frictional drag along the oil absorbent and the normal component of the fluid forces acting along the segment that is in the bend. During the first phase of the turn, when the greater portion of oil absorbent is on the original course with drag contributing to a maximum tension, one expects the cable to track inward toward the center of the turn in order to achieve a sufficient normal flow component. The internal tension of the absorbent in the bend will decrease as the length of absorbent on the original course becomes shorter. Correspondingly, the necessary normal flow velocity will reduce and the absorbent will follow more faithfully its course around the bend. The feasibility of such a turn will impose a limitation for the length of the oil absorbent. Also, the Protei vessel may need to be able to operate with a large tow angle.

2

Literature Study

The dynamical problem of towing long cables is the subject of extensive study in the fields of oceanography, oil and gas exploration, and for military applications. The work includes fundamental mathematical studies, numerical investigations, and experiments using models and full scale measurements.

The consequences of the free surface boundary condition will be examined. The oil absorbent is floating on the surface This is a significant discrepancy for any comparisons made with the submerged cable system. The Morison equation will be introduced along with the definition of coefficients of drag.

Diverse numerical techniques that have been applied to towed cable system over the past 50 years will be reviewed. Finally, a theoretical motivation for Kane's method is given. The mathematical details and implementation are given in the following chapter.

Towed Cable Systems

The towed-cable system is conceptually similar however there are some difficulties when drawing parallels with the oil absorbent under study here. Firstly, the cable array systems are towed below the surface at some depth. In fact maintaining a predictable depth for the oceanographic or surveying instruments is a primary objective in many studies. The oil absorbent, being towed on the surface, is restricted to motions in that plane, but will be subject to complex, non-linear effects associated with the free surface. The oil absorbent is also significantly shorter and stouter, with a maximum length of approximately 100 m in contrast with a typical sonar cable length of 6000 m, and the diameter of 20 cm in contrast with a typical sonar cable diameter of 5 cm. Despite these discrepancies, the existing studies remain a valuable source of physical insight for the basic process of pulling a long and flexible body through a turn.

The early work by D. A. Chapman [2], which included steady-state and dynamic simulation results, provides the foundation for many subsequent studies [3] [4] [5] [6]. Most strikingly, Chapman was able to identify a critical turning radius at which the towed system exhibits a dramatic change in response. Below this critical radius the tow system effectively collapses resulting in a large increase in vehicle depth and a decrease in 'fish' turning radius

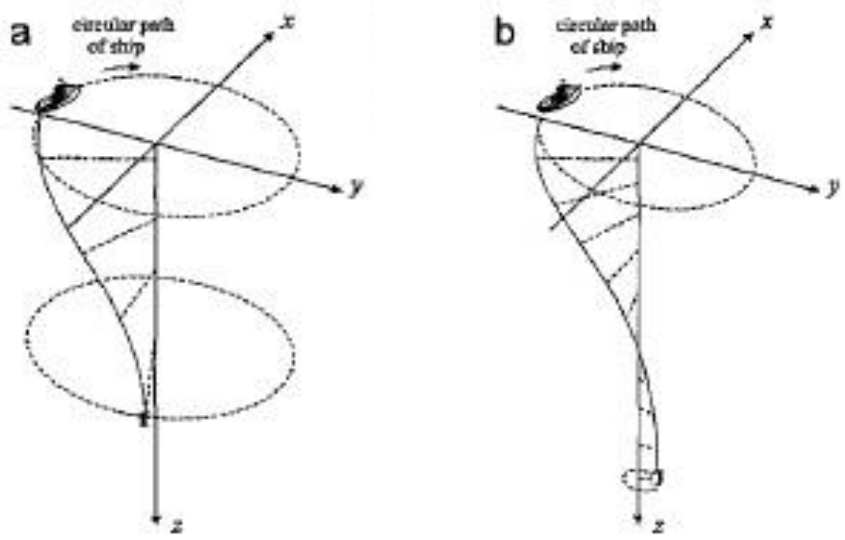

2.1 Submerged cable system

The submerged cable studied by Mr. Chapman and others has negative buoyuancy and comes to an equilibrium state in the vertical plane depending on the forward speed. One can think of the cable as 'flying' due to the drag component in the vertical direction. Hens, the cable needs to sink at lower speeds to maintain equilibrium. The oil absorbent floating on the surface is confined to the X-Y plane, and rather than caching excess cable underwater, the oil absorbent may go slack somewhere along its length. The trailing segment that has not yet turned will have zero velocity.

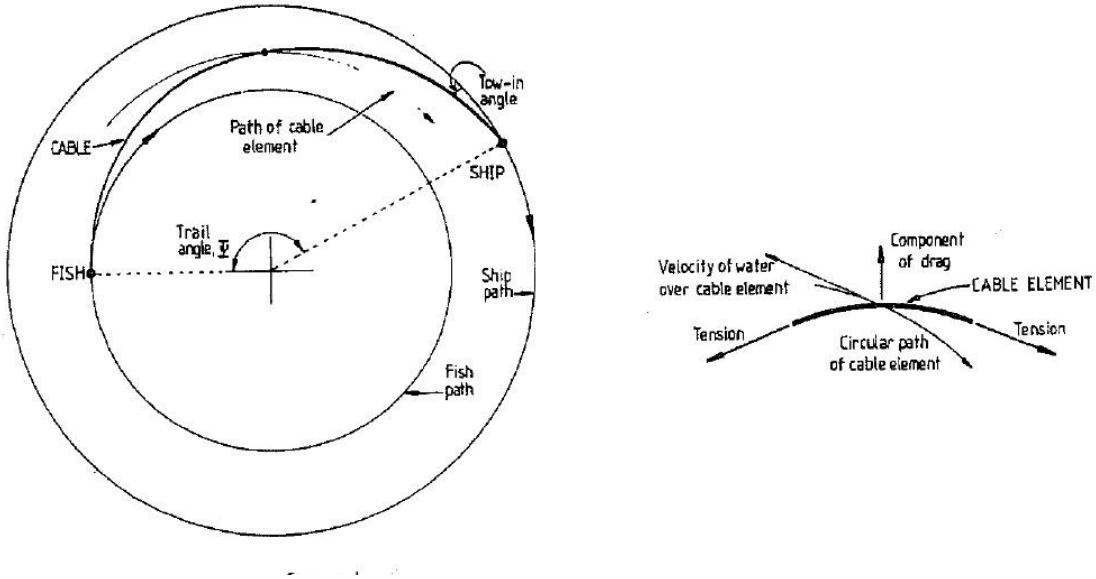

2.2 Physical motivation for tow-in angle

The system under study was an oceanographic instrument towed at the end of a long cable, as in figure 2.1. The path of the towed cable and fish, or instrument package, is shown in the figure. Starting at the ship, the tow-in angle is defined. The origin of this tow-in angle can be traced to the circular path of the turn and the resulting curvature of each cable element. Shown in detail is the attitude of the cable element with reference to its circular path. An equilibrium of forces necessitates a normal component of drag in order to oppose the cable tension. This requires a cross flow component, meaning that the cable cannot follow the ship path. The cable will adopt a profile such that the drag created by crossflow balances the effect of the curvature as seen in the detail, resulting in a spiral and the tow-in effect. Under the assumption that the ratio between the normal fluid drag and frictional drag is constant, the cable will take the shape of a logarithmic spiral (Chapman states that centrifugal forces in the system are at least two orders of magnitude smaller than the hydrodynamic forces and can therefore be neglected. [1]). This idealization does not account for decreasing internal tension along the cable, which will cause the tow-in angle to fair toward zero at the end of the cable.

Chapman identifies two distinct regions: large radius turns that represent a slight perturbation from the straight tow equilibrium, and the small radius turns where the cable profile collapses, accompanied by a large increase in depth. The boundary between these regions is a critical turning radius, related to the cable length, cable weight per meter, and towing speed. The abrupt variation of system characteristics is described by the mathematics of catastrophe theory. The critical radius is in fact a bifurcation point, or a fold in the curve where a small perturbation may precipitate a dramatic change of state. Across the range of cable lengths, weight, and normal drag coeffcient, the critical turning radius is greater than 25% of the cable length, implying that the absorbent system, assuming it exhibits similar behavior, should have the properties of the collapsed system.

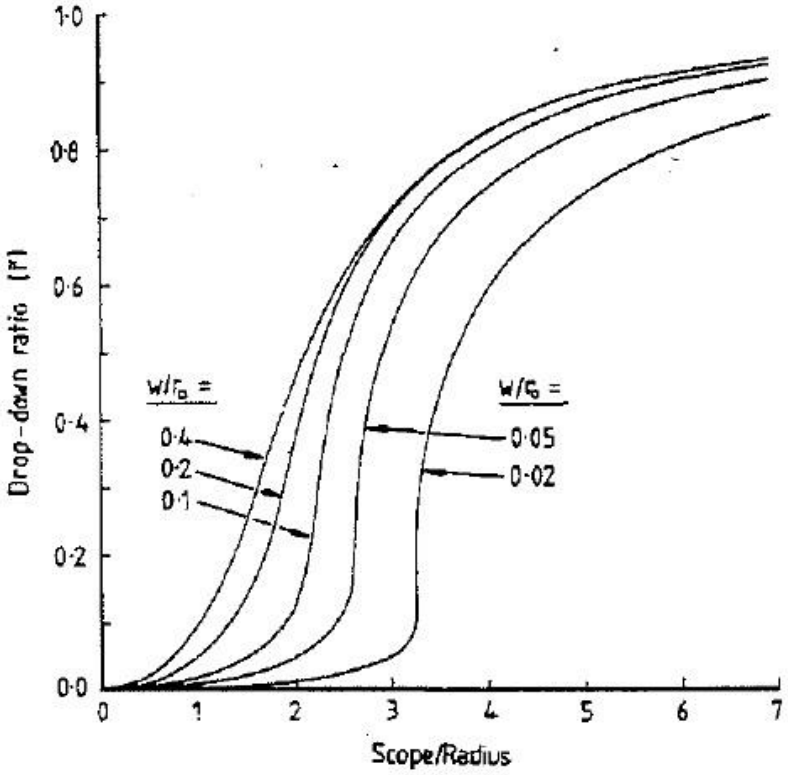

2.3 Submerged system response for varying L/r

The behavior of the towed system for broad and tight turns is plotted the firgure above, using a set of curves for varying cable properties. The figure is made using the the drop-down ratio for the Y axis, which is the ratio between the equilibrium towing depth and the deepest depth reached during the turn, and the ratio of length/radius for the X axis. The parameter w/r_0 is the ratio between the gravitational and the normal drag forces on the cable. Consider the towing vessel making a turn that spirals inward, so that the scope/radius gradually increases. Following the curve for $w/r_0 = 0.02$, as the radius decreases, the bifurcation point is reached for scope/radius=3.2, where the system shifts abruptly to the collapsed profile with a much larger drop-down ratio. If the ship track begins spiraling outwards again from this second configuration, the cable would retain the collapsed profile until scope/radius=3.15, this being the hollow in the double-back. This system therefore exhibits hystorisis.

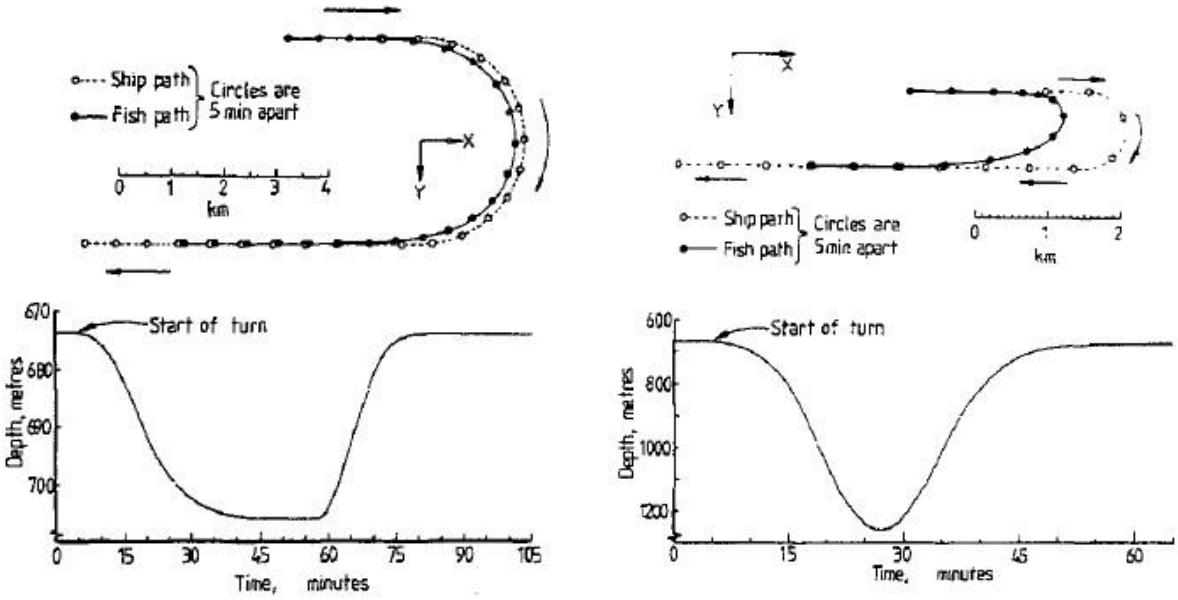

2.4 Transient response for submerged cable system

Simulation results presented by Chapman are shown above for the case of a broad turn and a tight turn. The lower figures give the depth of the fish, which is loosely interpreted here as a measure of the tension in the oil absorbent. For the absorbent system, being confined to the surface plane, any excess cannot be 'deposited' underwater. Rather than sinking to a deeper depth, the absorbent on the surface will come to a standstill (for sufficiently large scope/radius) before getting jerked around the bend to the new course.
The limiting case for a zero-radius turn for a submerged cable is a suspended vertically with depth equal to the length of the cable and with zero tension in the X-Y plane. Due to the transient nature of the turn this steady-state configuration will not be reached unless the vessel carries out an endless amount of turns at the origin. For the limiting case of zero radius turn, the segment which is changing direction will have zero tension. A chief property of cables and the absorbent is the innability to transmit forces other than tension. For the floating oil absorbent, the drop-down ratio is interpreted as the reciprocal of internal tension, where a value of one indicates slack cable. By interpreting the fish depth as a measure of the tension in the cable, it is possible to relate the conclusions in these studies to the floating oil absorbent.

INERTIAL FORCES OF CYLINDER + FLUID MASS | BENDING STIFFNESS | TENSION STIFFNESS DUE TO LONGITUDINAL DRAG

$$m\frac{\partial^2 y}{\partial t^2} + M\left(\frac{\partial}{\partial t} + U\frac{\partial}{\partial x}\right)^2 y + EI\frac{\partial^4 y}{\partial x^4} + \frac{\partial}{\partial x}\left\{\left(\frac{1}{2}c_T\frac{M}{D}U^2(L-x)\frac{\partial y}{\partial x}\right)\right\}$$

DAMPING TERM DUE TO TRANSVERSE DRAG

$$+\frac{1}{2}c_N\frac{MU}{D}\left(\frac{\partial}{\partial t} + U\frac{\partial}{\partial x}\right)y = 0$$

Where:

- m is cylinder linear mass
- M is fluid linear mass
- D is cylinder diameter
- E is cylinder elastic modulus
- I is cylinder radius of gyration
- c_T is longitudinal drag coefficient
- c_N is transverse drag coefficient

2.5 Linearized Paidussis equation for submerged cables

Kennedy makes some simplifications to the cable equation to arrive at a linear system which can be represented by a transfer function. [2] He investigated the Paidoussis Equation, which is a linearized momentum equation for the transverse dynamics of a cable in water. The system is simplified by considering only the X-Y plane, by linearizing the convection term using the tow velocity, and by making a small angle assumption for the cable – fluid angle. It has been demonstrated that Paidoussis' Equation is valid for angles less than 3 degrees, so this assumption is violated in all but the broadest turns.

In the remainder of Kennedy's investigation, a cross-track excitation with a range of frequencies is applied at the tow point and the propagation of this wave is studied. The results are summarized as the transfer function, where the response of the trailing end is shown for varying frequency. Mr. Kennedy was able to identify distinct regions of the excitation frequency for which the dominant terms of the model equation differ. This result is included in the figure of transfer function in figure 2.6.

For the circular towing vessel path under study here, the excitation frequency, ω, is interpreted using the angular speed of the turn, U/r. With the fluid speed, U, and the cable length L, the non-dimensional frequency reduces to the same scope/radius ratio as in Mr. Chapman's analysis:

$$\frac{\omega L}{U} = \frac{\frac{U}{r}L}{U} = \frac{L}{r}$$

Kennedy concluded that for dimensionless frequencies (or L/r) less than 10, the behaviour of the towed system is determined by the hydrodynamic forces. Such behaviour is termed water pulley behaviour, where the cable is forced into its circular track by normal drag as if it were turning over a pulley. This is exactly the behavior under study here.

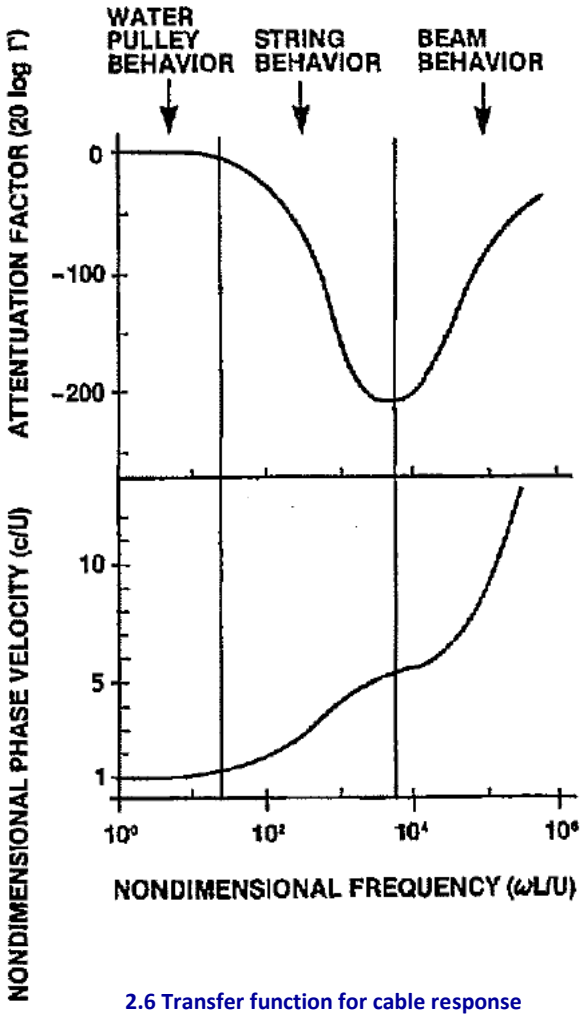

2.6 Transfer function for cable response

Resistance Estimate- B.E.P.

Estimating the resistance of a length of oil absorbent was the subject of a recent bachelor thesis project. This group of students pulled different lengths of oil absorbent through the towing tank at the ship hydromechanics department. Their results require careful processing because some test lengths exceeded the permissible length for avoiding interactions with reflected waves from the tank wall. Also, the ballasting method may have altered properties of the absorbent. The students removed the VandoClean oil sponge and replaced it with old clothes, which was presumably detrimental to its likeness to the original material.

The characteristic length for the oil absorbent is not the total length. The motion of the absorbent while under tow, along with the action of the absorbent in waves, will interfere with boundary layer development so that the boundary layer at the tail end is no longer affected by the flow at the beginning. There are other characteristic lengths, such as the absorbent diameter, which may better serve as the scale of local flow for large angles of incidence. The radius of curvature of the oil absorbent is also a reasonable choice. It may be possible to avoid guesswork here by considering the surface to be fully rough, for which the friction coefficient is independent of the Reynolds number. The roughness height is in the range of 2 to 3 mm, giving a friction coefficient of approximately 0,01. Completing the analysis of the towing tank data with this friction coefficient returned a form factor of 0,11, in contrast to the Bachelor Thesis result of 2.8. A slender body is expected to have a form factor of 0.1. The residual resistance is calculated using the radius of curvature for the Froude length. While interpreting this data, an attempt was made to come to a sensible division of resistance components based on physical insight. Based on these modifications to the analysis, the resistance for a 100 meter length of fully laden absorbent for a speed of 1 m/s is estimated to be 263 Newton.

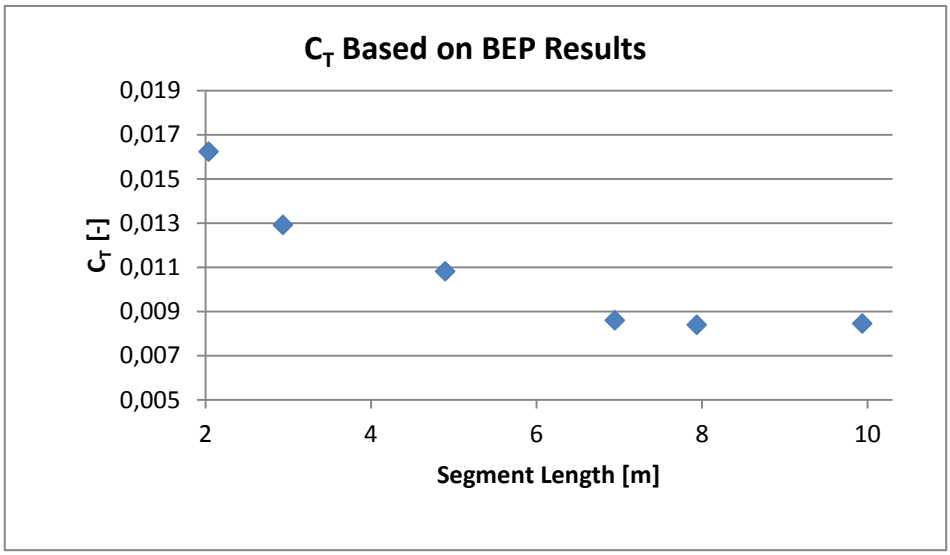

2.7 Total resistance coefficient for oil absorbent

Finally, an estimate for the tangential drag force coefficient is made based on the results from the B.E.P. experiments, yielding $C_D^{\parallel} = C_T = 0.0085$.

Free Surface Effects

In contrast with the cable systems presented above, the oil absorbent sponge floats in the water surface. This is a boundary of the fluid domain and as such it is subject to kinematic (no slip) and dynamic (force balance) boundary conditions.

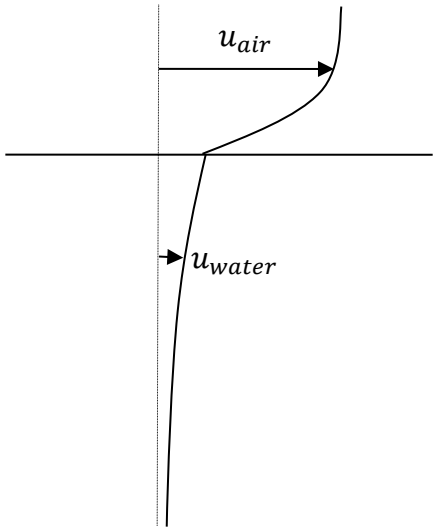

2.8 Free surface modelled as a shear layer

Strictly speaking, the interface between water and air can be treated as a shear layer. Not only does the air apply pressure to the fluid but it also exerts a shear force. This situation is shown in figure 2.8. For Newtonian fluids this force is proportional to the fluid velocity gradient. In accordance with the no slip boundary condition, the velocity of air and water is equal at the interface. The shear stress is also equal, but owing to the differing viscosities, the velocity gradient is discontinuous. The viscosity of air is much smaller than that of water, so this boundary condition is often simplified as a stress-free boundary, the free surface.

The boundary condition at the interface reads:

$$\tau_{water} = \mu_{water} \frac{\partial U_{water}}{\partial z}\bigg|_{z=0} = \tau_{air} = \mu_{air} \frac{\partial U_{air}}{\partial z}\bigg|_{z=0}$$

$$\frac{\partial U_{water}}{\partial z}\bigg|_{z=0} = \frac{\mu_{air}}{\mu_{water}} \frac{\partial U_{air}}{\partial z}\bigg|_{z=0} \cong 0$$

From the final expression, it can be seen that as a consequence of the vanishing ratio between the viscosities of the fluids, the shear stress in the fluid must come to zero at the surface, implying that the velocity gradient should also equal zero. In case turbulent stresses are also considered, the expression for shear stress takes the following form:

$$\tau = \mu \frac{\partial \bar{u}}{\partial z} - \rho \overline{u'w'}$$

The turbulent contribution, $-\rho\overline{u'w'}$, will reach zero at the interface because the vertical velocity fluctuations need to respect the kinematic boundary condition at the surface. For the submerged cables presented in the previous section, the system is well removed from the free surface and as a result the fluid is able to support viscous and turbulent shear stresses.

Any contribution to the radial force provided by the normal fluid drag is produced by stresses that develop in the fluid. Consider now the oil absorbent that is confined to this surface layer. Fluid behavior due to an obstacle such as the absorbent segment is complex. A turbulent wake will form behind the obstruction, and due to the proximity to the free surface, many simplifications which were possible in the submerged case based on symmetry considerations, are no longer valid. Simulation with computational fluid dynamics tools is necessary for a thorough evaluation of flow patterns. In proximity of the surface, it should be expected that the diminished capacity for shear stresses will result in a smaller normal fluid force component.

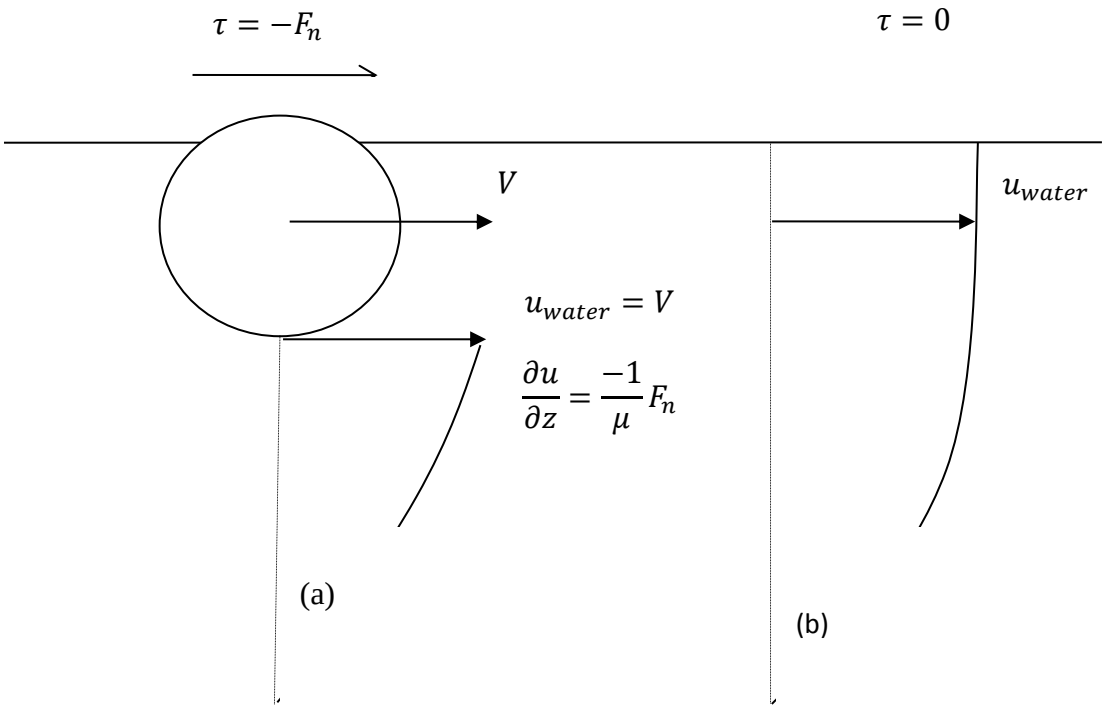

2.9 Development of simplified fluid velocity profile

As outlined above, while the absorbent is towed through a turn, the path that it follows through the water will depend on the radial force generated by normal fluid drag along the length of the oil absorbent. The oil absorbent velocity is decomposed into tangential and normal components so that a two-dimensional case can be examined. As shown in figure 2.9(a), a cross section of the absorbent will have a velocity relative to the fluid, V, and will impart a shear force on the fluid, $-F_n$. The attention is on the forces acting on the fluid, so F_n,the normal fluid force acting on the absorbent, is exchanged for its equal and opposite counterpart, $\tau = -F_n$. Although the complete flow pattern is too complex to predict analytically, some physical insights can be gained by restricting attention to the u-component of the fluid velocity. The kinematic and dynamic boundary conditions dictate the flow speed and gradient as shown.

For locations immediately adjacent to the oil absorbent, the stress-free boundary condition must again be satisfied, as in figure 2.9(b). The fluid at the surface will move with velocity of the absorbent due to the divergence-free assumption and because the vertical flow component is not included. In the absence of the

absorbent, the stress-free condition at the surface must again be satisfied, so the velocity gradient at the surface is zero. The evolution of the flow pattern shown in (a) occurs as the absorbent cross-section enters the velocity profile shown in (b). The shear force is continuous between these instances because of the linear relationship between stress and fluid strain and because the fluid is continuous, implying that the maximum normal force attainable in proximity to the water surface is limited by the velocity gradient of the boundary layer profile (b) at the absorbent draft. In reality, the contributions due to the vertical fluid velocity gradient may be of the same order, and the turbulent stresses in the wake of the cylinder will also have a role. The simplified case presented provides the physical insight in support of a normal drag coefficient that varies with the absorbent draft. It does not give a quantitative basis for estimating this variation with draft. A computational fluid dynamics approach is recommended if a more detailed analysis is desired.

Modeling of Fluid Forces

The Morison equation is a broadly accepted way to model the fluid forces acting on a body. This method it assumes a quadratic relationship between flow speed and drag force, similar to expressions for skin friction, bluff body drag, lift produced by an airfoil, and any number of other fluid forces. The Morison equation describes situations with oblique flow by dividing the incident flow into tangential and normal components and then determining the fluid force using separate drag coefficients for the tangential and normal force. The Morison equation is given below:

$$\vec{F}^{drag} = \frac{1}{2}\rho_w A^{\parallel} C_D^{\parallel} |u^{\parallel}| \vec{u}^{\parallel} + \frac{1}{2}\rho_w A^{\perp} C_D^{\perp} |u^{\perp}| \vec{u}^{\perp}$$

Both terms in the expression above includes a relevant surface area. For the tangential component, this will be the wetted area, and for the normal component, the frontal area. For consistency, the diameter is sometimes used as a uniform ‘drag area’, in which case the tangential drag coefficient is scaled by π, giving the same result.

An important simplification made by decomposing the fluid velocity and subsequently evaluating the fluid drag forces independently is to assume that these forces are not related to angle of incidence. In fact it is easy to imagine a situation, for example if a cylinder is slightly inclined to the flow, where flow patterns will differ substantially from the reference case where the cylinder is at right angles to the flow. Evaluating the Morison equation for fluid drag will return a normal fluid force that is equal to the drag force generated by a cylinder that is normal to the flow. The process of separating the incident flow into components does not capture the dependence of flow patterns on the orientation of the cylinder with respect to the flow. The normal component returned by the Morison equation is simply the drag force due to a cylinder in normal flow with a reduced speed.

The determination of coefficients of drag based on the reference cases, a cylinder aligned with the flow and a cylinder perpendicular to the flow, is problematic because of the reasons outlined above. A loading function, f, was introduced by researchers such as Buckham [4] to better model the influence of the angle of incidence on the fluid force. Including this nonlinear contribution was not possible in this work. The coefficients of drag are the primary tuning parameter for the numerical model.

Numerical Modeling

Ocean cable structures have received substantial attention in the last 50 years as the computational ability of computers has increased. These systems bear close similarity to the floating oil absorbent under tow. Generally, the solution approach can be divided into finite element methods or the approximation of governing equations using finite differences or lumped parameters.

The cable introduces nonlinear material and geometric behavior. The inability of the cable to support compressive loads is a fundamental characteristic of the material that must be represented faithfully. Secondly, the distributed fluid force along the cable will result in a catenary shape. An increasing externally applied load will stiffen the cable catenary. This geometric nonlinearity is a key property of the catenary and must be present in the model.

The application of finite element methods to the cable problem stems from early efforts where a static problem is solved. Commonly the evolution between successive static solution in time is modeled by a series of small perturbations. The finite element method is applied for example in the work of Ketchman and Lou [5], who were able to simulate cable behavior in the vertical plane for straight tow in 1975. The finite element modeling included strain and bending stresses, giving an element matrix with six degrees-of-freedom. In their conclusion, these authors acknowledge that the bending stiffness does not play an important role for many systems. According to Delmer et al, the inherently dynamic nature of cable problems and the prevalence of large deformations makes them ill-suited for finite element analysis [6].

2.10 Cable element with 6 d.o.f.

More recent studies prefer the finite difference or lumped parameter approach. In the lumped parameter approach, mass and externally applied forces are concentrated at nodes. This method differs from finite differencing in that the separation between the nodes is discrete. The finite difference approach is an approximation of an infinitesimally small differential element, so that the equations of motion for the continuous system are discretized. In the lumped parameter approach, the equations of motion are derived after the system has been discretized. It has been shown that these approaches are entirely equivalent, assuming similar physical assumptions [7].

In an early example of the finite difference approach, three-dimensional simulations of maneuvers were published by Ablow and Schechter in 1983 [7]. A balance of forces at some point along the cable provides the differential equation for the cable system, and gives three dynamic equations. Cable strain was included in this model, leading to three compatibility relations, and six equations in total. In the solution procedure, the mass matrix needs to be inverted, and here the authors identify the fundamental difficulty of coping with situations where the cable tension crosses zero. The inefficacy of cables in compression is not present in their modeling, which is mathematically limited to situations where the cable is under tension.

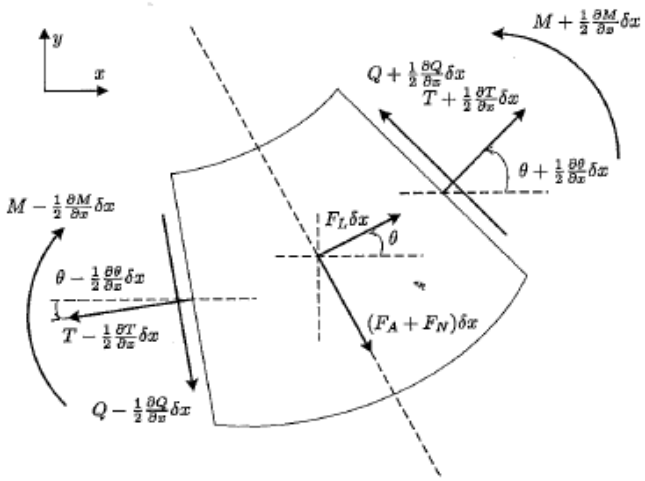

2.11 Differential cable element

The difficulty of modeling slack cables can be understood by recalling the speed of wave propagation along the cable, which is proportional to $\sqrt{T}$. As the tension decreases, the propagation speed for disturbances, and related energies, will become slower. Eventually, energy cannot be transmitted past a point with zero tension, and energy will build rapidly. In these regions, energy transfer due to the bending stiffness of the material becomes relevant, providing a means for transferring energy past the critical point.

The Woods Hole Oceanographic Institute Cable (WHOI Cable) simulation is a recent modeling effort that is broadly applicable to submerged cable problems. Both material and geometric nonlinearities outlined above are included. The difficulty encountered with slack cables is overcome by incorporating the bending stiffness. The resulting system, for the three-dimensional case, has 10 equations. It should be noted that this model is the foundation for the WHOI Cable computer program. Clearly the need for full generality, to solve diverse problems including moorings and complex towed arrays, has resulted in an increase in complexity. For example, these authors introduce secondary variables and regions of mesh refinement to control numerical artifacts which arise in the solution of the equations for curvature with low bending stiffness.

Kane's Method

The equations of motion for a lumped parameter model will be derived using Kane's method. This is a recent development in the analysis of dynamical systems, first published in the early 1960s by Prof. Thomas Kane of Stanford University. Originally termed 'Lagrange's form of D'Alembert's principle' by Kane himself, this approach to formulating the equations of motion has gained acceptance in the space industry and in the robotics industry, where ever-more-complex systems are coming within the reach of numerical simulation. The principal characteristics of Kane's method are the exclusion of non-contributing forces and the systematic way in which constraints can be incorporated. The application of Kane's method to the present problem, given in Chapter 3, will best demonstrate the principle underlying this method. The motivation that Kane provides in his textbooks is to clarify the process of formulating equations of motion using the principle of virtual work. In contrast with Lagrange's equations, Kane's method avoids the need for determining kinetic and potential energy functions and their derivatives.

Beginning with the statement of the D'Alembert's principle for a particle, and including the variation $\delta\vec{r}$ as in the derivation of virtual work:

$$\boldsymbol{F} \cdot \overrightarrow{\delta \mathrm{r}} = \mathrm{m}\mathbf{a} \cdot \overrightarrow{\delta \mathrm{r}}$$

The inner product has reduced a vector equation for three components to a single scalar equation for the energy budget of the system. To retrieve information about all degrees of freedom, the kinetic and potential energy of the system is subjected to the least-action principle. This is a statement of the conservation of energy; that the dynamic evolution of a system from one configuration to another will always take the most efficient route such that the energy function, the Lagrangian, is minimized. When expressed mathematically, this minimization returns an equation corresponding to each spatial directional derivative, providing the basis for formulating the dynamic equations of the system.

To "avoid the vagaries of virtual work", Kane uses *the principle of activity*. Beginning in the same way as above but using particle speed instead of position:

$$\boldsymbol{F} \cdot \mathbf{v} = \mathrm{m}\mathbf{a} \cdot \mathbf{v}$$

As before, a vector equation with three degrees of freedom has been reduced to a single scalar equation. In this case, however, the evaluation of the dot product will eliminate any constraint forces in $\vec{F}$, leaving only forces which are active along the direction defined by $\vec{v}$. The essence of Kane's method is to obtain dynamical equations of motion that contain sufficient information to describe the problem while automatically eliminating constraint forces. To this end, Kane introduces generalized coordinates, $\mathrm{q_j}$, and the partial velocity, $\mathbf{v_j}$:

$$\boldsymbol{F} \cdot \mathbf{v_j} = \mathrm{m}\mathbf{a} \cdot \mathbf{v_j}$$

$$\mathbf{v_j} = \frac{\partial \mathbf{v}}{\partial \dot{\mathrm{q}}_\mathrm{j}}$$

The generalized coordinates $\mathrm{q_j}$ are a set of P independent degrees of freedom that fully describe the motion of the system. The partial velocity $\mathbf{v_j}$, should be thought of as an expression of the activity principle, in that it defines how each velocity, $\mathbf{v}$, varies with respect to each generalized coordinate.

The formal expression of Kane's equation is:

$$\sum_{i=1}^{n} m_i \vec{a}_i \cdot \frac{\partial \vec{v}_i}{\partial \dot{q}_j} = \sum_{i=1}^{n} \vec{F}_i \cdot \frac{\partial \vec{v}_i}{\partial \dot{q}_j}\,, \qquad j = 1, \ldots, P$$

For each generalized coordinate, this expression is the summation of the activity of all inertial and applied forces. The dimension of the problem has been reduced from $\mathrm{n} * \dim(\vec{v})$ to P with the definition of appropriate generalized coordinates. Describing the systematic approach to finding the generalized coordinates is left to the following chapter, where the motivation underlying the manipulations will be more easily understood.

Finally, the relationship between Kane's equations and Lagrange's equations is given for the interested reader. Following Kane [8], p.134:

$$\boldsymbol{F}\cdot\mathbf{v_j} = \mathrm{m}\mathbf{a}\cdot\mathbf{v_j} = \mathrm{m}\frac{\partial\mathbf{v}}{\partial\dot{\mathrm{q}}_\mathrm{j}}\cdot\frac{\mathrm{d}\mathbf{v}}{\mathrm{dt}}$$

$$\frac{\mathrm{d}}{\mathrm{dt}}\frac{\partial\mathbf{v^2}}{\partial\dot{\mathrm{q}}_\mathrm{j}} = 2\frac{\partial\mathbf{v}}{\partial\dot{\mathrm{q}}_\mathrm{j}}\cdot\frac{\mathrm{d}\mathbf{v}}{\mathrm{dt}} + \frac{\partial\mathbf{v^2}}{\partial\mathrm{q}_\mathrm{j}}$$

$$\boldsymbol{F}\cdot\mathbf{v_j} = \frac{\mathrm{m}}{2}\left(\frac{\mathrm{d}}{\mathrm{dt}}\frac{\partial\mathbf{v^2}}{\partial\dot{\mathrm{q}}_\mathrm{j}} - \frac{\partial\mathbf{v^2}}{\partial\mathrm{q}_\mathrm{j}}\right) = \frac{\mathrm{d}}{\mathrm{dt}}\frac{\partial}{\partial\dot{\mathrm{q}}_\mathrm{j}}\left(\frac{\mathrm{m}\mathbf{v^2}}{2}\right) - \frac{\partial}{\partial\mathrm{q}_\mathrm{j}}\left(\frac{\mathrm{m}\mathbf{v^2}}{2}\right)$$

$$\boldsymbol{F}\cdot\mathbf{v_j} = \frac{\mathrm{d}}{\mathrm{dt}}\frac{\partial\mathrm{K}}{\partial\dot{\mathrm{q}}_\mathrm{j}} - \frac{\partial\mathrm{K}}{\partial\mathrm{q}_\mathrm{j}}$$

The last expression may be recognized as the Euler-Lagrange equation, verifying that these expressions are equivalent. When deriving motion equations following the Lagrange's approach, the kinetic energy function is differentiated with respect to each variable, as above. Avoiding this step is a key feature of Kane's method.

Literature Study Overview

Existing work for submerged towed cables was presented. Some physical concepts were introduced, such as the tow-in angle, a characteristic geometric quantity which originates in the production of normal fluid force needed to provide radial force along the absorbent in a turn. Also, the dimensionless parameter L/r is defined as the characteristic length for a maneuver. The variation of the towed system response with L/r is presented, but the interpretation of these submerged results in the context of the floating absorbent was problematic.

The influence of the free surface boundary conditions on the towed floating system is investigated using a simple case. The motivation for a draft-varying drag coefficient is given. A thorough analysis of these effects may include a more elaborate testing campaign or a computational fluid dynamics approach. Fluid forces on the absorbent will be modeled using the Morrison equation. A brief review of this approach and the limitations thereof was given along with the motivation for conducting a set of experiments for determining coefficients of tangential and normal drag.

A central challenge in modeling cables and sponges is the faithful representation of material nonlinearities. It has been shown that if the model is expected to perform in a wide range of conditions and geometries, then it will need to incorporate degrees of freedom for material behavior such as sheer, strain, and bending. For the oil absorbent sponge, it is assumed that the bending stiffness negligible. Further, a model is proposed that will execute a controlled set of maneuvers for which it is assumed that the tension remains nonnegative. The material response is not modeled, leading to a simpler rigid link system. The equations for the dynamics of the absorbent system will be derived using Kane's method. A theoretical motivation was provided in this chapter to orient the reader. The full implementation, given next, will hopefully bring an understanding of the underlying mechanism at work.

3

Numerical Modeling

The numerical model is designed to simulate a turn through 180 degrees. The system will be modeled using the lumped parameter method. The dynamical equations are found by applying Kane's method. Here, only the forces that act along the allowed degrees of freedom are considered, removing the need for calculating inter-link constraint forces. In this way, the complexity of the dynamic system is reduced by limiting the degrees of freedom to the rotation of each joint.

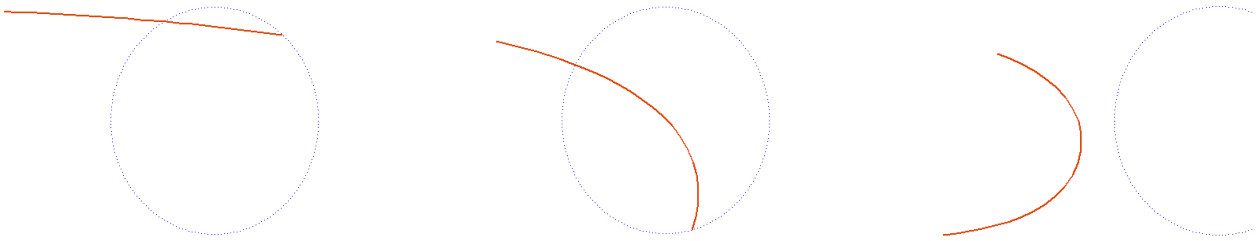

3.1 Simulated turn

The modeling of the turn is divided into two processes: the U-turn stage and the sail away stage, shown in figure 3.1. The first variable, the setup variable, is the distinguishing feature for each stage. The equations for the motion of the absorbent remain unchanged.

The towing force may be a function of time or angle to simulate a changing driving force in the sails of the Protei vessel. Fluid forces are determined based on the segment velocity and angle of flow incidence using the Morison equation.

Besides providing the derivation for the numerical model, this chapter also serves to illuminate the mechanism underlying Kane's method.

Model Setup

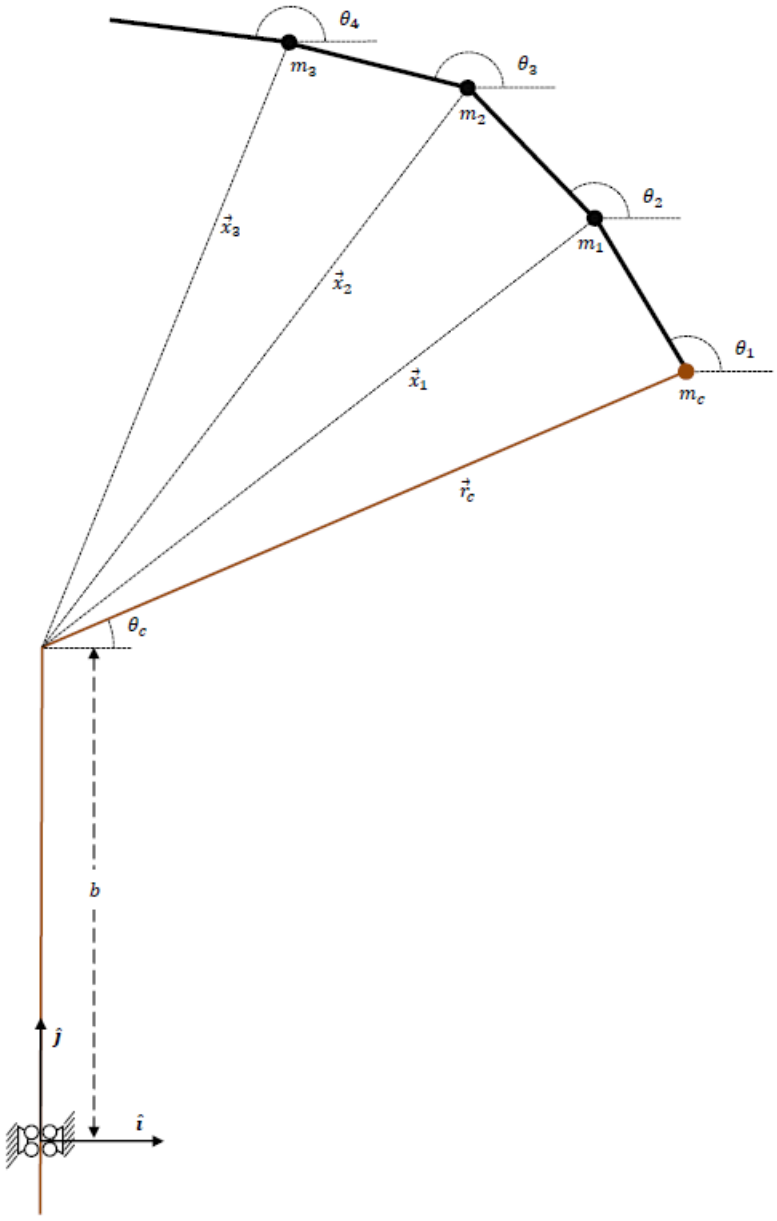

3.2 Schematic of numerical model

Shown above, the oil absorbent is divided into N segments and modeled as a serial linkage having P= $2N+3$ variables, $\{b, x_c, y_c, x_1, y_1, \ldots, x_N, y_N\}$, with r_c the pivot arm. The process is separated into two stages: the turn, followed by the exit. To model a turn of 180 degrees, the pivot arm, r_c, rotates through $\theta_c = [\pi{:}0]$ degrees. Then, with θ_c fixed, the towpoint translates in the negative $\hat{\boldsymbol{\jmath}}$ direction to simulate the exit from the turn. The model equations for the two stages differ only for b and θ_c, which are alternately fixed (no longer a variable), or serve to prescribe the path as the setup variable.

Due to constraints placed on the system, not all these variables are independent. Begin with the formal expression of a constraint, C_k. Let m_{k-1} and m_k be two adjoined point masses that are components of the oil absorbent tail. Given that the oil absorbent does not stretch, the constraint for m_k is:

$$(x_k - x_{k-1})^2 + (y_k - y_{k-1})^2 - {l_k}^2 = 0$$

This expression represents an holonomic constraint because it is integrable within the context of the least action principle, and since there exist *M=N+1* such constraints, the variable set is can be reduced to $K = P - M = N + 2$. It is a simple matter to satisfy the constraint equation by recognizing that m_k is required to move in a circle around m_{k-1} and by introducing the general coordinate θ_k to measure the angle between each segment and the $\hat{\imath}$ axis. The first and second time-derivatives of θ_k are ω_k and $\dot{\omega}_k$. From figure 3.2, the position, velocity and acceleration vectors for each absorbent segment are defined as follows:

$$\vec{x}_i = \left[r_c \cos\theta_c + \sum_{k=1}^{i} l_k \cos\theta_k \right] \hat{\boldsymbol{\imath}} + \left[b + r_c \sin\theta_c + \sum_{k=1}^{i} l_k \sin\theta_k \right] \hat{\boldsymbol{\jmath}}$$

$$\vec{v}_i = -\left[r_c \omega_c \sin\theta_c + \sum_{k=1}^{i} l_k \omega_k \sin\theta_k \right] \hat{\boldsymbol{\imath}} + \left[\dot{b} + r_c \omega_c \cos\theta_c + \sum_{k=1}^{i} l_k \omega_k \cos\theta_k \right] \hat{\boldsymbol{\jmath}}$$

$$\vec{a}_i = -\left[r_c(\dot{\omega}_c \sin\theta_c + \omega_c^2 \cos\theta_c) + \sum_{k=1}^{i} l_k(\dot{\omega}_k \sin\theta_k + \omega_k^2 \cos\theta_k) \right] \hat{\boldsymbol{\imath}} + \left[\ddot{b} + r_c(\dot{\omega}_c \cos\theta_c - \omega_c^2 \sin\theta_c) + \sum_{k=1}^{i} l_k(\dot{\omega}_k \cos\theta_k - \omega_k^2 \sin\theta_k) \right] \hat{\boldsymbol{\jmath}}$$

Mathematics of Kane's Method

A theoretical motivation for Kane's method is given in Chapter 2. In this section space is taken to develop the underlying mathematics.

Kane's equation states that:

$$\sum_{i=1}^{n} m_i \vec{a}_i \cdot \frac{\partial \vec{v}_i}{\partial \dot{q}_j} = \sum_{i=1}^{n} \vec{F}_i \cdot \frac{\partial \vec{v}_i}{\partial \dot{q}_j}, \qquad j = 1, \ldots, K$$

This is an expression of D'Alembert's principle for the dynamics of a system with *K* independent degrees of freedom. In Kane's method, the equations are multiplied by a set of vectors of partial derivatives with respect to the generalized speed $\dot{q}_j$. This is a technique called the null space method, used to confine the solution to the space allowed by the constraints. To explain how this technique encapsulates the constraints imposed on a system, consider our system having P=2*N+3* variables, $b, x_c, y_c, x_1, y_1, \ldots, x_N, y_N$. As above, there are *M=N+1* constraints, leading to *K=P-M=N+2* generalized variables, $\boldsymbol{q} = \{b, \theta_c, \theta_1, \theta_2, \ldots, \theta_N\}$.

Now it is necessary to make a distinction between configuration variables and motion variables. Kane's method works with motion variables and momenta following the Lagrangian representation. The configuration variables, angles θ, define the kinetics of the system while satisfying the constraints.

The motion constraints are found by differentiating the expression for the constraint C_k:

$$\frac{d}{dt}\left[(x_k - x_{k-1})^2 + (y_k - y_{k-1})^2 - {l_k}^2\right] = 0$$

$$\dot{x}_k(x_k - x_{k-1}) + \dot{x}_{k-1}(x_k - x_{k-1}) - \dot{y}_k(y_k - y_{k-1}) - \dot{y}_{k-1}(y_k - y_{k-1}) = 0$$

The motion constraints can be gathered into an M x P matrix as follows:

$$\boldsymbol{C \cdot \dot{x} = 0}$$

$$\begin{bmatrix} x_c & -y_c + b & x_c & -y_c + b & & & \varnothing \\ & x_1 - x_c & -y_1 + y_c & x_1 - x_c & -y_1 + y_c & & \\ & & \ddots & \ddots & \ddots & \ddots & \\ \varnothing & & & x_N - x_{N-1} & -y_N + y_{N-1} & x_N - x_{N-1} & -y_N + y_{N-1} \end{bmatrix} \cdot \begin{bmatrix} \dot{b} \\ \dot{x}_c \\ \dot{y}_c \\ \dot{x}_1 \\ \dot{y}_1 \\ \vdots \\ \dot{x}_N \\ \dot{y}_N \end{bmatrix} = \mathbf{0}$$

The number of constraints, M, will reduce the number of independent variables to K=P-M=N+2, as before. In the previous section, the polar transformation was identified by inspection. The formal approach is to find the null space matrix of **C**, where **C** is the M x P constraint matrix acting on the vector $\boldsymbol{\dot{x}}$, shown above. The vector $\boldsymbol{\dot{x}}$ is viewed as having some orientation in its configuration space. The rows of **C**, when dotted with $\boldsymbol{\dot{x}}$, indicate which directions are forbidden (=0). Therefore, $\boldsymbol{C \cdot \dot{x} = 0}$, defines a subspace that is perpendicular to the rows of **C**. The null space of **C** can be defined by K independent eigenvectors of **C** that are arranged to form the P x K matrix **S**. Kane suggests that these be chosen by inspection according to physical significance.

The variables $\boldsymbol{\dot{x}}$ must occupy the same space, giving a new set of variables, the generalized speed, $\boldsymbol{\dot{q}}$:

$$\boldsymbol{\dot{x} = S \cdot \dot{q}}$$

The elements of $\boldsymbol{\dot{q}}$ are independent, in contrast to the elements of $\boldsymbol{\dot{x}}$ which are related by the constraints of **C**. Returning to the polar coordinates introduced in the previous section, this expression gives the kinematic equations for configuration variables in terms of the newly defined generalized speeds, $\{\dot{b}, \dot{\theta}_c, \dot{\theta}_1, \ldots, \dot{\theta}_N\}$.

$$\begin{bmatrix} \dot{b} \\ \dot{x}_c \\ \dot{y}_c \\ \dot{x}_1 \\ \dot{y}_1 \\ \dot{x}_2 \\ \dot{y}_2 \\ \vdots \\ \dot{x}_N \\ \dot{y}_N \end{bmatrix} = \begin{bmatrix} 1 & & & & & \varnothing \\ 0 & -r_c \sin\theta_c & & & & \\ 1 & r_c \cos\theta_c & & & & \\ 0 & -r_c \sin\theta_c & -l \sin\theta_1 & & & \\ 1 & r_c \cos\theta_c & l \cos\theta_1 & & & \\ 0 & -r_c \sin\theta_c & -l \sin\theta_1 & -l \sin\theta_2 & & \\ 1 & r_c \cos\theta_c & l \cos\theta_1 & l \cos\theta_2 & & \\ \vdots & \vdots & \vdots & \vdots & \ddots & \\ 0 & -r_c \sin\theta_c & -l \sin\theta_1 & -l \sin\theta_2 & \cdots & -l \sin\theta_N \\ 1 & r_c \cos\theta_c & l \cos\theta_1 & l \cos\theta_2 & \cdots & l \cos\theta_N \end{bmatrix} \cdot \begin{bmatrix} \dot{b} \\ \dot{\theta}_c \\ \dot{\theta}_1 \\ \dot{\theta}_2 \\ \vdots \\ \dot{\theta}_N \end{bmatrix}$$

The dynamical equations of the system are also over-determined. To apply the constraints, the motion must be restricted to the same subspace as above. This is accomplished by projecting the governing equations onto a set of vectors that defines this subspace. There are N+2 motion variables, which are not independent due to the constraints, $\mathbf{V} = \{\dot{b}, \dot{\theta}_c, \boldsymbol{v}_1, \boldsymbol{v}_2, \ldots, \boldsymbol{v}_N\}^T$

To construct the set of vectors, use the fact that the elements of **V** are linear in $\dot{\boldsymbol{x}}$ and that the components of $\dot{\boldsymbol{q}}$ are independent. The partial derivatives, $\frac{\partial \vec{v}_i}{\partial \dot{q}_j}$, are also independent vectors and span a space that is consistent with the constraints. Kane's method has confined the solution to the allowed configurations by projecting the dynamic equations onto this set of vectors, providing a systematic and efficient way to impose constraints on a dynamical system.

Evaluation of the partial derivatives reveals that this term is non-zero for $i \geq j$. Some clumsiness has been introduced in the notation by the setup variables, $\dot{b}$ and $\vec{v}_c$. The numbered subscripts refer to segments of the oil-absorbent. This will become convenient when the fluid forces are developed as this portion of the system of equations remains unchanged throughout. Kane arranges these 'partial velocities' in tabular form:

3.1 Partial velocities

	$\dot{b}, \vec{v}_c$	$\vec{v}_1$	$\vec{v}_2$	$\vec{v}_3$	...	$\vec{v}_N$
$\dot{q}_1 = \dot{b}$	$\langle 0,1 \rangle$	$\langle 0,1 \rangle$	$\langle 0,1 \rangle$	$\langle 0,1 \rangle$	...	$\langle 0,1 \rangle$
$\dot{q}_1 = \dot{\theta}_c$	$\langle {-r_c \sin\theta_c \atop r_c \cos\theta_c} \rangle$	$\langle {-r_c \sin\theta_c \atop r_c \cos\theta_c} \rangle$	$\langle {-r_c \sin\theta_c \atop r_c \cos\theta_c} \rangle$	$\langle {-r_c \sin\theta_c \atop r_c \cos\theta_c} \rangle$	...	$\langle {-r_c \sin\theta_c \atop r_c \cos\theta_c} \rangle$
$\dot{q}_2 = \dot{\theta}_1$	0	$\langle {-l \sin\theta_1 \atop l \cos\theta_1} \rangle$	$\langle {-l \sin\theta_1 \atop l \cos\theta_1} \rangle$	$\langle {-l \sin\theta_1 \atop l \cos\theta_1} \rangle$	...	$\langle {-l \sin\theta_1 \atop l \cos\theta_1} \rangle$
$\dot{q}_3 = \dot{\theta}_2$	0	0	$\langle {-l \sin\theta_2 \atop l \cos\theta_2} \rangle$	$\langle {-l \sin\theta_2 \atop l \cos\theta_2} \rangle$	...	$\langle {-l \sin\theta_2 \atop l \cos\theta_2} \rangle$
$\dot{q}_4 = \dot{\theta}_3$	0	0	0	$\langle {-l \sin\theta_3 \atop l \cos\theta_3} \rangle$	...	$\langle {-l \sin\theta_3 \atop l \cos\theta_3} \rangle$
$\vdots$	$\vdots$	$\vdots$	$\vdots$	$\vdots$	$\ddots$	$\vdots$
$\dot{q}_P = \dot{\theta}_N$	0	0	0	0	...	$\langle {-l \sin\theta_N \atop l \cos\theta_N} \rangle$

The first column contains the setup variables. Depending on which stage of the turn is being modeled, either $\dot{b}$ or $\vec{v}_c$ is used, which corresponds to either the first or second rows. The remaining entries do not change. The vector, $\langle -\sin\theta_j\,,\ \cos\theta_j\rangle$, is the normal vector of link j. The dot product in the statement of Kane's Equation retains only the components of force $\vec{F}$ that will influence the coordinate θ_j. The sparcity pattern of this array indicates that only the links outboard of j contribute to the jth dynamic equation.

During the u-turn, the angle θ_c of the pivot arm is the setup variable for the constrained system, whereas during the exit stage the setup variable is b. The system of equations for both stages has the same size, defined by P=N+1. The system can also be configured to model a continuous turn for the purpose of finding the steady tow-in angle.

Inertial Forces

Generalized inertial forces are determined as follows:

$$F_{\theta_j}{}^* = \sum_{i=1}^{n} m_i \vec{a}_i \cdot \frac{\partial \vec{v}_i}{\partial \dot{q}_j}\,, \qquad j = 1, \ldots, P$$

Expanding the summation for n=3, j=2:

$$F_{\theta_2}{}^* = m_1\vec{a}_1 \cdot \frac{\partial \vec{v}_c}{\partial \dot{q}_2} + m_2\vec{a}_2 \cdot \frac{\partial \vec{v}_1}{\partial \dot{q}_2} + m_3\vec{a}_3 \cdot \frac{\partial \vec{v}_2}{\partial \dot{q}_2} + m_4\vec{a}_4 \cdot \frac{\partial \vec{v}_3}{\partial \dot{q}_2}$$

$$= (m_2\vec{a}_2 + m_3\vec{a}_3 + m_4\vec{a}_4) \cdot \frac{\partial \vec{v}_1}{\partial \dot{q}_2}$$

From the definition of the velocity, the partial derivative $\frac{\partial \vec{v}_i}{\partial \dot{q}_j}$ is zero for $i < j$, and equal to $\frac{\partial \vec{v}_j}{\partial \dot{q}_j}$ othewise. Keep in mind that the first index refers to the setup variable, and that $\vec{v}_1 \ldots \vec{v}_N$ are the velocities of the absorbent segments. Recall the definition of the acceleration:

$$\vec{a}_i = \sum_{k=1}^{i} \vec{a}'_k\ ; \qquad \vec{a}'_k = \begin{pmatrix} -l_k(\dot{\omega}_k \sin\theta_k + \omega_k^2 \cos\theta_k) \\ l_k(\dot{\omega}_k \cos\theta_k - \omega_k^2 \sin\theta_k) \end{pmatrix}$$

Now the generalized inertial force can be rearranged into the following form, allowing for the pre-computation of the mass term in the numerical implementation.

$$F_{\theta_2}{}^* = [m_2\,(\vec{a}'_1 + \vec{a}'_2) + m_3\,(\vec{a}'_1 + \vec{a}'_2 + \vec{a}'_3) + m_4(\vec{a}'_1 + \vec{a}'_2 + \vec{a}'_3 + \vec{a}'_4)] \cdot \frac{\partial \vec{v}_1}{\partial \dot{q}_2}$$

$$F_{\theta_2}{}^* = [(m_2 + m_3 + m_4)\vec{a}'_1 + (m_2 + m_3 + m_4)\vec{a}'_2 + (m_3 + m_4)\vec{a}'_3 + m_4\vec{a}'_4] \cdot \frac{\partial \vec{v}_1}{\partial \dot{q}_2}$$

The general expression with $\dot{q}_1 = \dot{\theta}_c$, with, $\boldsymbol{l} = \{r_c, l, \dots, l\}$ and $\boldsymbol{\theta} = \{\theta_c, \theta_1, \theta_2, \dots, \theta_N\}$ reads:

$$F_{\theta_j}{}^* = \sum_{k=1}^{P}\left(\sum_{\substack{s=j+1\\ s\geq k+1}}^{N} m_s\right)\begin{pmatrix} -l_k(\dot{\omega}_k \sin\theta_k + \omega_k^2 \cos\theta_k) \\ l_k(\dot{\omega}_k \cos\theta_k - \omega_k^2 \sin\theta_k)\end{pmatrix}\cdot\begin{pmatrix} -l_j \sin\theta_j \\ l_j \cos\theta_j\end{pmatrix}, \qquad j = 1, \dots P$$

$$F_{\theta_j}{}^* = \sum_{k=1}^{P}\left(\sum_{\substack{s=j+1\\ s\geq k+1}}^{N} m_s\right)\left[l_k l_j \sin\theta_j\left(\dot{\omega}_{\mathrm{k}} \sin\theta_k + \omega_{\mathrm{k}}^2 \cos\theta_k\right) + l_k l_j \cos\theta_j\left(\dot{\omega}_{\mathrm{k}} \cos\theta_k - \omega_{\mathrm{k}}^2 \sin\theta_k\right)\right],$$
$$j = 1, \dots, P$$

The final step is to collect like terms into a system of equations for numerical integration. Here l is a constant segment length and $\boldsymbol{\theta} = \{\theta_1, \theta_2, \dots, \theta_N\}$. The angle-sum identity has been used. For j=1:

$$F_{\dot{\theta}_c}{}^* = \sum_{k=1}^{N}\left(\sum_{\substack{s=1\\ s\geq k}}^{N} m_s\right) l r_c \cos(\theta_c - \theta_k)\,\dot{\omega}_k + \sum_{k=1}^{N}\left(\sum_{\substack{s=1\\ s\geq k}}^{N} m_s\right) l r_c \sin(\theta_c - \theta_k)\,\omega_k^2$$

For the remaining degrees of freedom, $\dot{q}_{j+1} = \dot{\theta}_j,\ \ j = 1, \dots, N$:

$$F_{\dot{\theta}_j}{}^* = \sum_{k=1}^{N}\left(\sum_{\substack{s=j\\ s\geq k}}^{N} m_s\right) l^2 \cos(\theta_j - \theta_k)\,\dot{\omega}_k + \sum_{k=1}^{N}\left(\sum_{\substack{s=j\\ s\geq k}}^{N} m_s\right) l^2 \sin(\theta_j - \theta_k)\,\omega_k^2, \qquad j = 1, \dots, N$$

For the exit stage, $\dot{q}_1 = \dot{b}$, l is a constant segment length and $\boldsymbol{\theta} = \{\theta_1, \theta_2, \dots, \theta_N\}$. The first equation is:

$$F_{\dot{b}}{}^* = \left(\sum_{s=1}^{N} m_s\right)\ddot{b} + \sum_{k=1}^{N}\left(\sum_{\substack{s=1\\ s\geq k}}^{N} m_s\right)\begin{pmatrix} -l(\dot{\omega}_k \sin\theta_k + \omega_k^2 \cos\theta_k) \\ l(\dot{\omega}_k \cos\theta_k - \omega_k^2 \sin\theta_k)\end{pmatrix}\cdot\begin{pmatrix} 0 \\ 1\end{pmatrix}$$

$$F_{\dot{b}}{}^* = Nm\ddot{b} + \sum_{k=1}^{N}\left(\sum_{\substack{s=1\\ s\geq k}}^{N} m_s\right) l \cos\theta_k\,\dot{\omega}_k - \sum_{k=1}^{N}\left(\sum_{\substack{s=1\\ s\geq k}}^{N} m_s\right) l \sin\theta_k\,\omega_k^2$$

The quantity Nm is simply the total mass of the absorbent.

The remaining equations are the following:

$$F_{\dot{\theta}_j}{}^{*} = \left(\sum_{s=j}^{N} m_s\right) l \cos\theta_j \, \ddot{b} + \sum_{k=1}^{N}\left(\sum_{\substack{s=1 \\ s\geq k}}^{N} m_s\right) l^2 \cos(\theta_j - \theta_k)\, \dot{\omega}_k + \sum_{k=1}^{N}\left(\sum_{\substack{s=1 \\ s\geq k}}^{N} m_s\right) l^2 \sin(\theta_j - \theta_k)\, \omega_k^2 \qquad j = 1, \dots, N$$

The incremental mass, m_s, includes the added mass in fluid. The third term involving ω^2 can readily be interpreted as the centripetal force.

Tow Force

The active forces fall into two categories. The towing force, which only acts on the first point mass, is defined by the user. It may be the product of a separate analysis of the driving force generated by the sails of the Protei vessel. The magnitude and direction may be a function of time. Evaluating the summation with $\vec{F} = \{\vec{F}^{tow}, 0,0, \dots, 0\}$ leaves:

$$F_{\dot{q}_j}^{tow} = \sum_{i=1}^{n} \vec{F}_i \cdot \frac{\partial \vec{v}_i}{\partial \dot{q}_j}, \qquad j = 1, \dots, P$$

$$F_{\dot{b}}^{tow} = -F_y^{tow}$$

$$F_{\dot{\theta}_c}^{tow} = -F_x^{tow} l_1 \, sin\,\theta_1 + F_y^{tow} l_1 \, cos\,\theta_1$$

A tow force that is perpendicular to the pivot arm is:

$$F_{\dot{q}}^{tow} = \{F^{tow} r_c, 0,0, \dots, 0\}$$

Fluid Force

The oil absorbent has been discretized in space and is now represented by a series of point masses. The fluid forces are applied at each point mass. The local flow velocity, $\vec{u}$, at each point is equal to the opposite of the velocity of the linkage at that point.

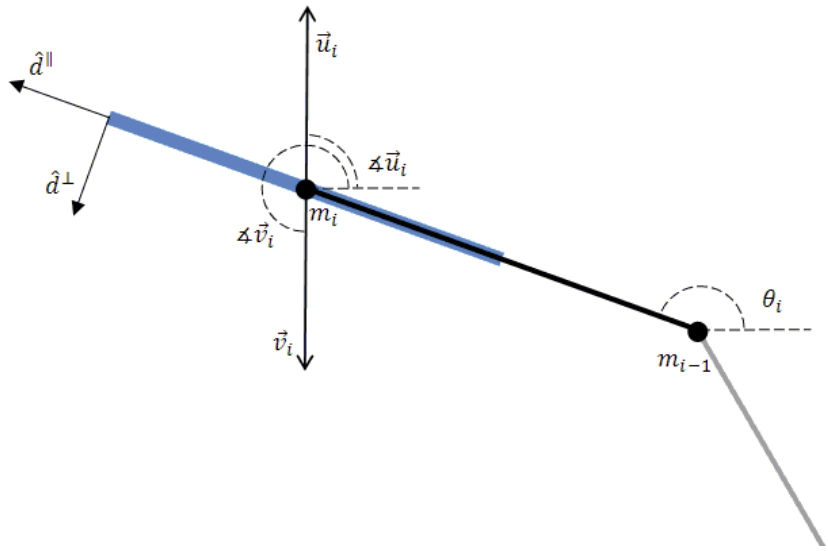

3.3 Definition of fluid forces

$$\vec{u} = -\vec{v}$$

$$\vec{u} = \left[r_c \omega_c \sin\theta_c + \sum_{k=1}^{i} l_k \omega_k \sin\theta_k \right] \hat{\boldsymbol{\imath}} - \left[\dot{b} + r_c \omega_c \cos\theta_c + \sum_{k=1}^{i} l_k \omega_k \cos\theta_k \right] \hat{\boldsymbol{\jmath}}$$

Drag is calculated for a fictive segment that is centered at the point mass. Once the relative fluid velocity is determined at each point mass, the fluid velocity is divided into components tangential and normal to the segment of oil absorbent, expressed in $\langle \hat{\boldsymbol{\imath}}, \hat{\boldsymbol{\jmath}} \rangle$ coordinates for the calculation of forces at each point mass. The vector $\hat{d}_i^{\parallel}$ has unit length, it indicates the orientation of segment i. Its counterpart, $\hat{d}_i^{\perp}$, indicates the normal direction for segment i.

$$\hat{d}_i^{\parallel} = \frac{\vec{x}_{i+1} - \vec{x}_i}{|\vec{x}_{i+1} - \vec{x}_i|} = \langle cos\theta_i, sin\theta_i \rangle$$

$$\hat{d}_i^{\perp} = \langle -sin\theta_i, cos\theta_i \rangle$$

So that the tangential and normal velocities become:

$$\vec{u}_i^{\parallel} = (\vec{u}_i \cdot \hat{d}_i^{\parallel})\hat{d}_i^{\parallel}$$

$$\vec{u}_i^{\perp} = (\vec{u}_i \cdot \hat{d}_i^{\perp})\hat{d}_i^{\perp}$$

Evaluating these expressions for later use:

$$\vec{u}_i^{\parallel} = \left[-\dot{b} sin\theta_i - r_c \omega_c (-\sin\theta_c \, cos\theta_i + \cos\theta_c \, sin\theta_i) \right.$$
$$\left. - \sum_{k=1}^{i} l_k \omega_k \, (-\sin\theta_k \cos\theta_i + \cos\theta_k \, sin\theta_i) \right] \langle cos\theta_i, sin\theta_i \rangle$$

$$\vec{u}_i^{\perp} = \left[-\dot{b} cos\theta_i - r_c \omega_c (\sin\theta_c \, sin\theta_i + \cos\theta_c \, cos\theta_i) \right.$$
$$\left. - \sum_{k=1}^{i} l_k \omega_k (\sin\theta_k \sin\theta_i + \cos\theta_k \cos\theta_i) \right] \langle -sin\theta_i, cos\theta_i \rangle$$

In these expressions the summation over k gives the direction of the local flow velocity and θ_i gives the orientation of the oil-absorbent segment. A factor of (-1) has been removed for convenience so that these expressions will take the same form as the inertial forces above after using the angle-sum identities as follows:

$$\vec{u}_i^{\parallel} = \left[\dot{b} sin\theta_i + r_c \omega_c \sin(\theta_i - \theta_c) + \sum_{k=1}^{i} l_k \omega_k \sin(\theta_i - \theta_k) \right] \langle -cos\theta_i, -sin\theta_i \rangle$$

$$\vec{u}_i^{\perp} = \left[\dot{b} cos\theta_i + r_c \omega_c \cos(\theta_i - \theta_c) + \sum_{k=1}^{i} l_k \omega_k \cos(\theta_i - \theta_k) \right] \langle sin\theta_i, -cos\theta_i \rangle$$

Fluid forces may be divided into normal and tangential components following the Morison equation. The Morison equation models the drag components tangent and normal to a submerged body according to the expression:

$$\vec{F}^{drag} = \frac{1}{2} \rho_w A^{\parallel} C_D^{\parallel} |u^{\parallel}| \vec{u}^{\parallel} + \frac{1}{2} \rho_w A^{\perp} C_D^{\perp} |u^{\perp}| \vec{u}^{\perp}$$

In this expression, $\vec{F}$ is the fluid force acting on a segment of oil absorbent, ρ_w is the fluid density, $C_D^{\perp}$ and $C_D^{\parallel}$ are respectively the coefficients of normal and tangential drag, and A is the relevant area. A is calculated when the absorbent draft is selected. For the drag force caused by normal flow, the relevant area is the frontal area, $A^{\perp} = T l_i$, whereas the submerged surface area is the relevant area for the frictional drag caused by tangential flow, $A^{\parallel} = 2r \cos^{-1}\left(\frac{r-T}{r}\right) l_i$. The fluid force is written compactly:

$$\vec{F}_i^{drag} = F_i^{\parallel} \langle -cos\theta_i, -sin\theta_i \rangle + F_i^{\perp} \langle sin\theta_i, -cos\theta_i \rangle, \qquad i = 1, \ldots, n$$

With:

$$F_i^{\parallel} = \frac{1}{2}\rho_w A^{\parallel} C_f \left| \dot{b} sin\theta_i + r_c \omega_c \sin(\theta_i - \theta_c) + \sum_{k=1}^{i} l_k \omega_k \sin(\theta_i - \theta_k) \right|^2$$

$$F_i^{\perp} = \frac{1}{2}\rho_w A^{\perp} C_D \left| \dot{b} cos\theta_i + r_c \omega_c \cos(\theta_i - \theta_c) + \sum_{k=1}^{i} l_k \omega_k \cos(\theta_i - \theta_k) \right|^2$$

The setup linkages do not interact with the water, therefore $F^{\parallel}$ and $F^{\perp}$ are only defined for oil absorbent segments $i = 1, \dots, N$.

From the definition of the active force:

$$\vec{F}_{\theta_j}^{drag} = \sum_{i=1}^{P} \vec{F}_i^{drag} \cdot \frac{\partial \vec{v}_i}{\partial \dot{q}_j}, \qquad j = 1, \dots, P$$

For the u-turn stage, with $\dot{q}_1 = \dot{\theta}_c$, with $\boldsymbol{l} = \{r_c, l, \dots, l\}$ and $\boldsymbol{\theta} = \{\theta_c, \theta_1, \theta_2, \dots, \theta_N\}$. For $j = 1$, this term reads:

$$\vec{F}_{\dot{\theta}_c}^{drag} = \sum_{i=1}^{N} \left[F_i^{\parallel} \langle -cos\theta_i, -sin\theta_i \rangle \cdot \frac{\partial \vec{v}_i}{\partial \dot{q}_1} + F_i^{\perp} \langle sin\theta_i, -cos\theta_i \rangle \cdot \frac{\partial \vec{v}_i}{\partial \dot{q}_1} \right]$$

$$\vec{F}_{\dot{\theta}_c}^{drag} = \sum_{i=1}^{N} \left[F_i^{\parallel} \langle -cos\theta_i, -sin\theta_i \rangle \cdot \langle -r_c sin\theta_c, r_c cos\theta_c \rangle + F_i^{\perp} \langle sin\theta_i, -cos\theta_i \rangle \cdot \langle -r_c sin\theta_c, r_c cos\theta_c \rangle \right]$$

$$\vec{F}_{\dot{\theta}_c}^{drag} = \sum_{i=1}^{N} \left[r_c (\cos\theta_i \sin\theta_c - \sin\theta_i \cos\theta_c) F_i^{\parallel} - r_c (sin\theta_i \sin\theta_c + cos\theta_i \cos\theta_c) F_i^{\perp} \right]$$

$$\vec{F}_{\dot{\theta}_c}^{drag} = \sum_{i=1}^{N} \left[r_c \sin(\theta_c - \theta_i) F_i^{\parallel} - r_c \cos(\theta_c - \theta_i) F_i^{\perp} \right]$$

The remaining general speeds are $\dot{\theta}_j$ for $j = 1, \dots, N$. The partial velocity $\frac{\partial \vec{v}_i}{\partial \dot{\theta}_j}$ is nonzero for i>j:

$$\vec{F}_{\dot{\theta}_j}^{drag} = \sum_{i=j}^{N} \left[l_j \sin(\theta_j - \theta_i) F_i^{\parallel} - l_j \cos(\theta_j - \theta_i) F_i^{\perp} \right], \qquad j = 1, \dots, N$$

For the sail-away stage, with $\dot{q}_1=\dot{b}$, l=constant, and $\boldsymbol{\theta} = \{\theta_1, \theta_2, \dots, \theta_N\}$, the first equation, with $\frac{\partial \vec{v}_i}{\partial \dot{q}_1} = \langle 0,1 \rangle$, reads:

$$\vec{F}_{\dot{b}}^{drag} = \sum_{i=1}^{N} \left[-l \sin\theta_i \, F_i^{\parallel} - l \cos\theta_i \, F_i^{\perp} \right], \qquad j = 1$$

The variable $\dot{b}$ is present in the expressions for $F^{\parallel}$ and $F^{\perp}$. Finally, the equation for the remaining degrees of freedom:

$$\vec{F}_{\dot{\theta}_j}^{drag} = \sum_{i=j}^{N} \left[l_j \sin(\theta_j - \theta_i) \, F_i^{\parallel} - l_j \cos(\theta_j - \theta_i) F_i^{\perp} \right], \qquad j = 1, \dots, N$$

Linearization and Numerical Implementation

There are two terms that are quadratic in the generalized coordinates, the centripetal force and the fluid drag. The equations are linearized by omitting the centripetal term and by substituting a linear drag model. Previous work by Chapman, Srivastava, Kennedy, and Grosenbaugh indicates that the fluid drag terms dominate the behavior of the towed cable system. Chapman reports that the centripetal force is smaller by two orders of magnitude, it will be neglected here. The quadratic fluid drag model is linearized by dropping the exponent. If the fluid speeds are kept near to one, it is assumed that this will not introduce a large error.

$$\vec{F}^{drag} = \frac{1}{2}\rho_w A^{\parallel} C_D^{\parallel} \vec{u}^{\parallel} + \frac{1}{2}\rho_w A^{\perp} C_D^{\perp} \vec{u}^{\perp}$$

It is now possible to write Kane's equation per absorbent segment as a system of N+1 equations.

For the u-turn stage, with $\boldsymbol{l}$ the uniform segment length and $\boldsymbol{\theta} = \{\theta_1, \theta_2, \dots, \theta_N\}$, the first equation reads:

$$N m {r_c}^2 \dot{\omega}_c + \sum_{k=1}^{N} \left(\sum_{\substack{s=1 \\ s \geq k}}^{N} m_s \right) l r_c \cos(\theta_c - \theta_k) \, \dot{\omega}_k \quad \text{- - - - - -} \quad \text{Inertial force}$$

$$= F^{tow} r_c \quad \text{- - - - - - - - - -} \quad \text{Towing force}$$

$$+ \sum_{i=1}^{N} r_c \sin(\theta_c - \theta_i) \frac{1}{2} \rho_w A^{\parallel} C_D^{\parallel} \left(r_c \omega_c \sin(\theta_i - \theta_c) + \sum_{k=1}^{i} l \omega_k \sin(\theta_i - \theta_k) \right) \quad \text{-} \quad \text{Tangential drag}$$

$$- \sum_{i=1}^{N} r_c \cos(\theta_c - \theta_i) \frac{1}{2} \rho_w A^{\perp} C_D^{\perp} \left(r_c \omega_c \cos(\theta_i - \theta_c) + \sum_{k=1}^{i} l_k \omega_k \cos(\theta_i - \theta_k) \right) \quad \text{-} \quad \text{Normal drag}$$

For the generalized speeds, $\dot{\theta}_j, j = 1, \dots, N$:

$\left(\sum_{s=j}^{N} m_s\right) r_c{}^2 \dot{\omega}_c + \sum_{k=1}^{N} \left(\sum_{\substack{s=1 \\ s \geq k}}^{N} m_s\right) l_k l_j \cos(\theta_j - \theta_k)\, \dot{\omega}_k$ - - - - - Inertial force

$= \sum_{i=j}^{N} l_j \sin(\theta_j - \theta_i) \frac{1}{2} \rho_w A^{\parallel} C_D^{\parallel} \left(r_c \omega_c \sin(\theta_i - \theta_c) + \sum_{k=1}^{i} l \omega_k \sin(\theta_i - \theta_k)\right)$ - Tangential drag

$- \sum_{i=j}^{P} l_j \cos(\theta_j - \theta_i) \frac{1}{2} \rho_w A^{\perp} C_D^{\perp} \left(r_c \omega_c \cos(\theta_i - \theta_c) + \sum_{k=1}^{i} l_k \omega_k \cos(\theta_i - \theta_k)\right)$ - Normal drag

$j = 1, \dots, N$

For the sail-away stage, with l the uniform segment length and $\boldsymbol{\theta} = \{\theta_1, \theta_2, \dots, \theta_N\}$.

For the generalized speed $\dot{b}$:

$N m \ddot{b} + \sum_{k=1}^{N} \left(\sum_{\substack{s=1 \\ s \geq k}}^{N} m_s\right) l \cos\theta_k\, \dot{\omega}_k$ - - - - - - Inertial force

$= -F^{tow}$ - - - - - - - - - - Towing force

$- \sum_{i=1}^{N} l \sin\theta_i \frac{1}{2} \rho_w A^{\parallel} C_D^{\parallel} \left(\dot{b} sin\theta_i + \sum_{k=1}^{i} l \omega_k \sin(\theta_i - \theta_k)\right)$ -- - - Tangential drag

$- \sum_{i=1}^{N} l \cos\theta_i \frac{1}{2} \rho_w A^{\perp} C_D^{\perp} \left(\dot{b} cos\theta_i + \sum_{k=1}^{i} l \omega_k \cos(\theta_i - \theta_k)\right)$ - - - Normal drag

For the generalized speeds, $\dot{\theta}_j$, with $j = 1, \dots, N$:

$\left(\sum_{s=j}^{N} m_s\right) l \cos\theta_j\, \ddot{b} + \sum_{k=1}^{N} \left(\sum_{\substack{s=j \\ s \geq k}}^{N} m_s\right) l^2 \cos(\theta_j - \theta_k)\, \dot{\omega}_k$ - - - - Inertial force

$= \sum_{i=j}^{N} l \sin(\theta_j - \theta_i) \frac{1}{2} \rho_w A^{\parallel} C_D^{\parallel} \left(\dot{b} sin\theta_i + \sum_{k=1}^{i} l \omega_k \sin(\theta_i - \theta_k)\right)$ - - - Tangential drag

$- \sum_{i=j}^{N} l \cos(\theta_j - \theta_i) \frac{1}{2} \rho_w A^{\perp} C_D^{\perp} \left(\dot{b} cos\theta_i + \sum_{k=1}^{i} l \omega_k \cos(\theta_i - \theta_k)\right)$ - - Normal drag

$j = 1, \dots, N$

With an eye toward time integration, the equations will be arranged into matrix form in a way that minimizes computational effort.

Beginning with the inertial force, a matrix $\mathbb{M}$ is defined such that (with $\dot{\omega}$ a column vector):

$$\mathbb{M}\dot{\boldsymbol{\omega}} = \sum_{k=1}^{N}\left(\sum_{\substack{s=j \\ s\geq k}}^{N} m_s\right) l_k l_j \cos\left(\theta_j - \theta_k\right)\dot{\omega}_k$$

$$\mathbb{M}_{jk} = \left(\sum_{\substack{s=j \\ s\geq k}}^{N} m_s\right) l_k l_j \cos\left(\theta_j - \theta_k\right)$$

Each segment has the same mass, *dm*. Summation over *s* inside the brackets is pre-computed as the matrix m_{jk}. The first row and first column, corresponding to the setup variables, have been added to fill the matrix. It is important to note that these degrees of freedom do not contribute to the total mass of the system.

$$m = \begin{bmatrix} Ndm & Ndm & (N-1)dm & (N-2)dm & \cdots & dm \\ Ndm & Ndm & (N-1)dm & (N-2)dm & \cdots & dm \\ (N-1)dm & (N-1)dm & (N-1)dm & (N-2)dm & \cdots & dm \\ (N-2)dm & (N-2)dm & (N-2)dm & (N-2)dm & \cdots & dm \\ \vdots & \vdots & \vdots & \vdots & \ddots & \vdots \\ dm & dm & dm & dm & \cdots & dm \end{bmatrix}$$

$$\mathbb{M}_{jk} = m_{jk} l_k l_j \cos\left(\theta_j - \theta_k\right)$$

Most of the expressions contain a similar trigonometric function. An array containing the difference $\theta_j - \theta_k$ will be defined and reused to improve the computational efficiency.

For the u-turn stage:

$$\mathbb{M}\ddot{\mathbf{q}} = m \circ \begin{bmatrix} r_c^{\,2} & l r_c \cos\left(\theta_c - \theta_1\right) & l r_c \cos\left(\theta_c - \theta_2\right) & \cdots & l r_c \cos\left(\theta_c - \theta_N\right) \\ r_c l \cos\left(\theta_1 - \theta_c\right) & l^2 & l^2 \cos\left(\theta_1 - \theta_2\right) & \cdots & l^2 \cos\left(\theta_1 - \theta_N\right) \\ r_c l \cos\left(\theta_2 - \theta_c\right) & l^2 \cos\left(\theta_2 - \theta_1\right) & l^2 & \cdots & l^2 \cos\left(\theta_2 - \theta_N\right) \\ \vdots & \vdots & \vdots & \ddots & \vdots \\ r_c l \cos\left(\theta_N - \theta_c\right) & l^2 \cos\left(\theta_N - \theta_1\right) & l^2 \cos\left(\theta_N - \theta_2\right) & \cdots & l^2 \end{bmatrix} \begin{bmatrix} \dot{\omega}_c \\ \dot{\omega}_1 \\ \dot{\omega}_2 \\ \vdots \\ \dot{\omega}_N \end{bmatrix}$$

For the sail-away stage:

$$\mathbb{M}\ddot{\mathbf{q}} = m \circ \begin{bmatrix} 1 & l\cos\theta_1 & l\cos\theta_2 & \cdots & l\cos\theta_N \\ l\cos\theta_1 & l^2 & l^2\cos(\theta_1-\theta_2) & \cdots & l^2\cos(\theta_1-\theta_N) \\ l\cos\theta_2 & l^2\cos(\theta_2-\theta_1) & l^2 & \cdots & l^2\cos(\theta_2-\theta_N) \\ \vdots & \vdots & \vdots & \ddots & \vdots \\ l\cos\theta_N & l^2\cos(\theta_N-\theta_1) & l^2\cos(\theta_N-\theta_2) & \cdots & l^2 \end{bmatrix} \begin{bmatrix} \ddot{b} \\ \dot{\omega}_1 \\ \dot{\omega}_2 \\ \vdots \\ \dot{\omega}_N \end{bmatrix}$$

Here ° indicates element-wise matrix multiplication.

The fluid forces will be expressed compactly as $(\mathbb{P}^S\mathbb{F}_{\parallel} + \mathbb{P}^C\mathbb{F}_{\perp})\dot{q}$ by separating the summations into matrices $\mathbb{F}$ and $\mathbb{P}$. $\mathbb{F}$ contains the calculation of the local flow speed, where as $\mathbb{P}$ contains the evaluation of the dot product with the partial velocities. Defining the matrices $\mathbb{F}^{\parallel}$ and $\mathbb{F}^{\perp}$, such that for the u-turn:

$$\mathbb{F}^{\perp}\dot{\boldsymbol{q}} = D^{\perp} \begin{bmatrix} 0 & & & & \varnothing \\ r_c\cos(\theta_1-\theta_c) & l & & & \\ r_c\cos(\theta_2-\theta_c) & l\cos(\theta_2-\theta_1) & l & & \\ \vdots & \vdots & \vdots & \ddots & \\ r_c\cos(\theta_N-\theta_c) & l\cos(\theta_N-\theta_1) & l\cos(\theta_N-\theta_2) & \cdots & l \end{bmatrix} \begin{bmatrix} \omega_c \\ \omega_1 \\ \omega_2 \\ \vdots \\ \omega_N \end{bmatrix}$$

$$\mathbb{F}^{\parallel}\dot{\boldsymbol{q}} = D^{\parallel} \begin{bmatrix} 0 & & & & \varnothing \\ r_c\sin(\theta_1-\theta_c) & 0 & & & \\ r_c\sin(\theta_2-\theta_c) & l\sin(\theta_2-\theta_1) & 0 & & \\ \vdots & \vdots & \vdots & \ddots & \\ r_c\sin(\theta_N-\theta_c) & l\sin(\theta_N-\theta_1) & l\sin(\theta_N-\theta_2) & \cdots & 0 \end{bmatrix} \begin{bmatrix} \omega_c \\ \omega_1 \\ \omega_2 \\ \vdots \\ \omega_N \end{bmatrix}$$

For the sail away stage:

$$\mathbb{F}^{\perp}\dot{\boldsymbol{q}} = D^{\perp} \begin{bmatrix} 0 & & & & \varnothing \\ \cos(\theta_1) & l & & & \\ \cos(\theta_2) & l\cos(\theta_2-\theta_1) & l & & \\ \vdots & \vdots & \vdots & \ddots & \\ \cos(\theta_N) & l\cos(\theta_N-\theta_1) & l\cos(\theta_N-\theta_2) & \cdots & l \end{bmatrix} \begin{bmatrix} \dot{b} \\ \omega_1 \\ \omega_2 \\ \vdots \\ \omega_N \end{bmatrix}$$

$$\mathbb{F}^{\parallel}\dot{\boldsymbol{q}} = D^{\parallel}\begin{bmatrix} 0 & & & & \varnothing \\ \sin(\theta_1) & 0 & & & \\ \sin(\theta_2) & l\sin(\theta_2-\theta_1) & 0 & & \\ \vdots & \vdots & \vdots & \ddots & \\ \sin(\theta_N) & l\sin(\theta_N-\theta_1) & l\sin(\theta_N-\theta_2) & \cdots & 0 \end{bmatrix}\begin{bmatrix} \dot{b} \\ \omega_1 \\ \omega_2 \\ \vdots \\ \omega_N \end{bmatrix}$$

where $D^{\perp} = \frac{1}{2}\rho_w A^{\perp} C_D^{\perp}$, and $D^{\parallel} = \frac{1}{2}\rho_w A^{\parallel} C_D^{\parallel}$.

These matrix expressions return the force vectors $F_i^{\parallel}$ and $F_i^{\perp}$, as above. The matrices $\mathbb{F}$ are lower triangular, reflecting the range of the summation $k = 1, \ldots, i$.

It remains only to project this result onto the constraint space. This is accomplished with the following matrices.

For the u-turn stage:

$$\mathbb{P}^{C} = \begin{bmatrix} -r_c & -r_c\cos(\theta_c-\theta_1) & -r_c\cos(\theta_c-\theta_2) & \cdots & -r_c\cos(\theta_c-\theta_N) \\ & -l & -l\cos(\theta_1-\theta_2) & \cdots & -l\cos(\theta_1-\theta_N) \\ & & l & \cdots & -l\cos(\theta_2-\theta_N) \\ & & & \ddots & \vdots \\ \varnothing & & & & -l \end{bmatrix}$$

$$\mathbb{P}^{S} = \begin{bmatrix} 0 & r_c\sin(\theta_c-\theta_1) & r_c\sin(\theta_c-\theta_2) & \cdots & r_c\sin(\theta_c-\theta_N) \\ & 0 & l\sin(\theta_1-\theta_2) & \cdots & l\sin(\theta_1-\theta_N) \\ & & 0 & \cdots & l\sin(\theta_2-\theta_N) \\ & & & \ddots & \vdots \\ \varnothing & & & & 0 \end{bmatrix}$$

For the sail-away stage:

$$\mathbb{P}^{C} = \begin{bmatrix} 0 & -1 & -1 & \cdots & -1 \\ & -l & -l\cos(\theta_1-\theta_2) & \cdots & -l\cos(\theta_1-\theta_N) \\ & & l & \cdots & -l\cos(\theta_2-\theta_N) \\ & & & \ddots & \vdots \\ \varnothing & & & & -l \end{bmatrix}$$

$$\mathbb{P}^S = \begin{bmatrix} 0 & -1 & -1 & \cdots & -1 \\ & 0 & l\sin(\theta_1 - \theta_2) & \cdots & l\sin(\theta_1 - \theta_N) \\ & & 0 & \cdots & l\sin(\theta_2 - \theta_N) \\ & & & \ddots & \vdots \\ \varnothing & & & & 0 \end{bmatrix}$$

The oil absorbent system has been described by the following system of differential equations:

$$\mathbb{M}\ddot{\mathbf{q}} = \mathbb{F}_{tow} + (\mathbb{P}^S\mathbb{F}^{\parallel} + \mathbb{P}^C\mathbb{F}^{\perp})\dot{\boldsymbol{q}}$$

$$\ddot{\mathbf{q}} = \mathbb{M}^{-1}\mathbb{F}_{tow} + \mathbb{M}^{-1}(\mathbb{P}^S\mathbb{F}^{\parallel} + \mathbb{P}^C\mathbb{F}^{\perp})\dot{\boldsymbol{q}}$$

The differential equations are solved using inbuilt Matlab solvers for stiff systems. ODE23s was selected because it produces reliable results. The author recognizes that a more efficient numerical implementation is possible.

Numerical Modeling Overview

The equations of motion for the absorbent system has been derived these equations have been linearized by neglecting the centripetal term and by adopting a linear fluid drag model. The final matrix form as been implemented in Matlab. Complete Matlab files can be found in appendix B.

Finally, it is hoped that the readers understanding of Kane's method has been enriched by this example.

4

Experiments

The primary goal in these experiments was to estimate the drag coefficients for a floating towed system. Also of interest is the degree to which the conclusions of submerged cable studies presented above transferred to the oil-absorbent system that is confined to the free surface.

A short series of open water tests was organized and carried out the help of the TU Delft towing tank staff. A TU Delft research vessel was conducting open water experiments on a unrelated project and it was possible to join the trip on very short notice.

The test segment was towed through a series of circular tracks to establish a relationship between system variables for a study turn. Working within the limitations of open water experiments, a sensible result was achieved for a steady-state condition. Transient response was also investigated, but these results were difficult to interpret.

Test Methodology

The test subject was a length of polypropylene/polyethylene blend line. It was selected for its specific gravity of 0.707, representing a length of oil absorbent laden with oil. Using actual oil absorbent would have been impractical because of the task of ballasting. The polypropylene line was suspended behind the vessel with a length of Dynema to remove it as much as possible from the high energy section of the research vessel wake. Every 10 meters along the polypropylene line was marked with a thick black stripe.

The tests were carried out in a small bight on the Hollands Diep near Numansdorp (51.70629N, 4.40161E) on July 4, 2014. On the day of the tests, the weather was calm with south-east wind building to 7 kn by the end of the afternoon. The TU Delft research vessel is a motor cruiser of approximately 8 m and moderate displacement. The varying lengths of line were towed from a measurement installation on the swim platform as the skipper of the research vessel performed a variety of turns. The experiment lasted three hours, during which time 21 runs were recorded with a total of 32 turns.

4.1 Experimental apparatus

During each run, three data sets were collected. First, the GPS position of the tow point was recorded. The raw GPS position underwent a correction for atmospheric disturbances, yielding a very accurate position. It was used to calculate the radius of curvature of the track to identify steady turns and to find the velocity and heading of the towing point. The towing force was recorded using a load sensor. A 200N load sensor was selected and was calibrated beforehand. The tow-in angle was measured with a custom-built arc. A video camera was mounted above the arc to record the tow-in angle during each run. The tow-in angle was under predicted, and the limits of the arc were exceeded during some turns. The standard deviation for this measurement was set to reflect this. Finally, a digital watch was mounted in the shot to synchronize the data streams.

Each cable length was towed through a series of circular tracks, follows by several u-turns. The experiment was designed to establish the relationship between the parameter L/r and the system response. The precision of the open-water experimental setup was limited, but a good range of satisfactory turns were recorded. The u-turns also contribute to this data set, and are used to assess the validity of the model for transient behavior. There were few repeated data points for the transient runs. The precision available in the open water setting for defining a u-turn trackwas very low.

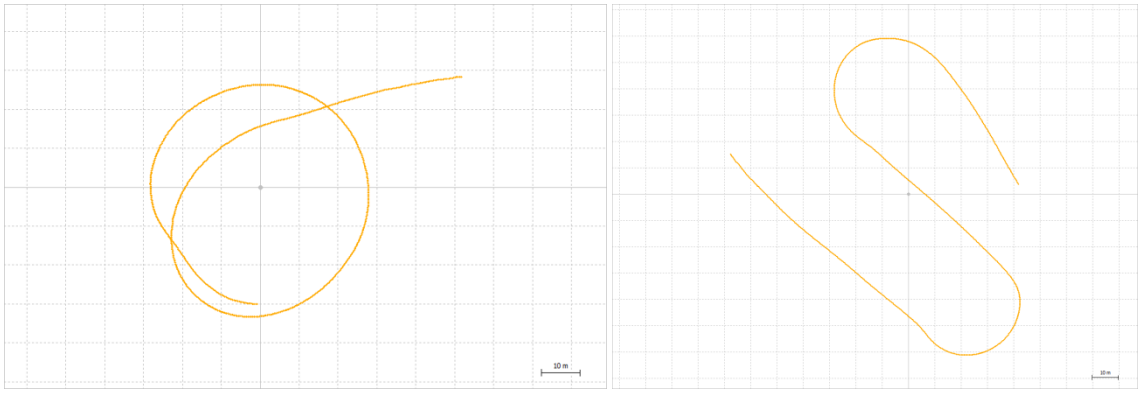

4.2 Sample tracks: circles and u-turns.

Data Processing

The radius of curvature was calculated from the GPS data using the following result of differential calculus:

$$R = \left| \frac{(\dot{x}^2 + \dot{y}^2)^{3/2}}{\dot{x}\ddot{y} - \dot{y}\ddot{x}} \right|$$

Discrete approximations were used for the time-derivatives. A moving average with a window size of ten seconds was needed to achieve a usable result.

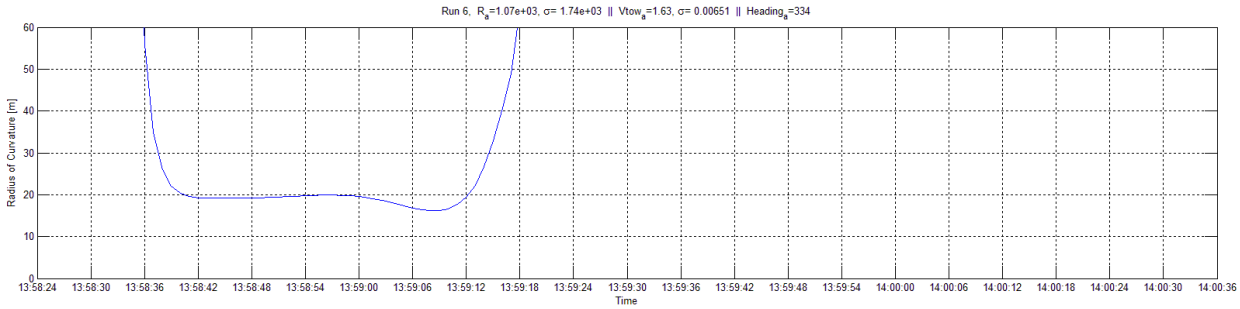

4.3 Radius of curvature for turn #9

Candidate turns were selected based on the following criteria:

1. The sample should be at least 30 seconds long, during which the standard deviation of the radius should be less than 10% of the mean value.
2. The video recording of the tow-in angle must be complete and in focus.

The average radius of curvature over the whole sample is reported along with the standard deviation.

The tow in angle is recorded from video. The arc used to measure the tow-in angle had a maximum at 45°. During tests it was quickly apparent that this was an underestimation. The standard deviation was assumed based on the fidelity of the video recordings and the shortcomings of the measuring system: 1° for for tow-in angles less than 20°, 2° for values between 20° and 45°, and 3° for values above 45°.

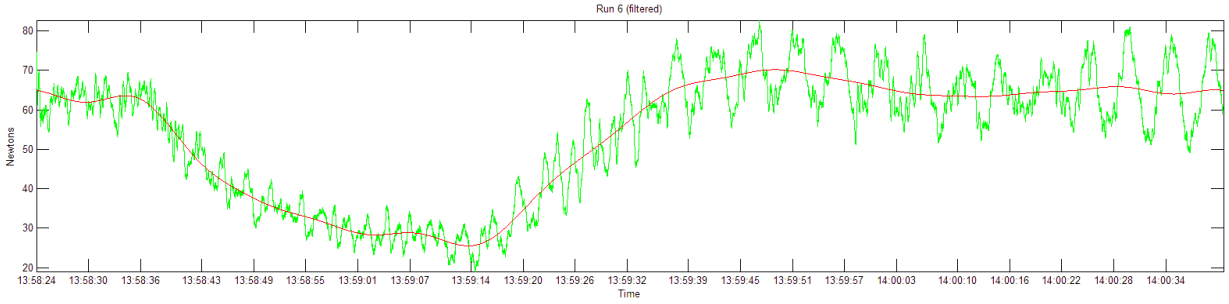

4.4 Tow force for turn #9

The raw force data is shown above for the same turn. An ideal pass-band filter with cut off frequency set to 0.1 Hz was applied to remove the high-frequency content that is not relevant to this study. The force is sampled over the last quarter of each turn, where it is assumed the system has reached a steady-state. The mean value is reported along with the standard deviation. For the turn shown in the figures above, the force is sampled between 13:59:02 and 13:59:09. It is easy to observe the two stages of the force profile: an exponential decay during the turn and a nearly linear rise during the exit.

A refined subset of the data was made for calculating coefficients. Here, the turns are filtered used by requiring the relative error for L/r <5%, and the high-energy wake of the research vessel is avoided by keeping only data with tow-in > 25 degrees. Finally, derived values with a relative error greater than ten percent were removed.

Uncertainties

Due to the uncontrolled nature of open-water experiments, the level of precision possible in the setup and the measurments is coarse at best. One of the key uncertainties is in the translation of GPS position to course and speed through water. If there was a steady current in the test area, the recorded position would inlcude this spurious component, whereas the force trace and the tow-in angle may not. The research vessel may also be subject to wind or wave loads. Another shortcoming in the test setup and possible source of error is the impact of the research vessel wake on the behavior of the test segment. Each of these uncertainties will be addressed below.

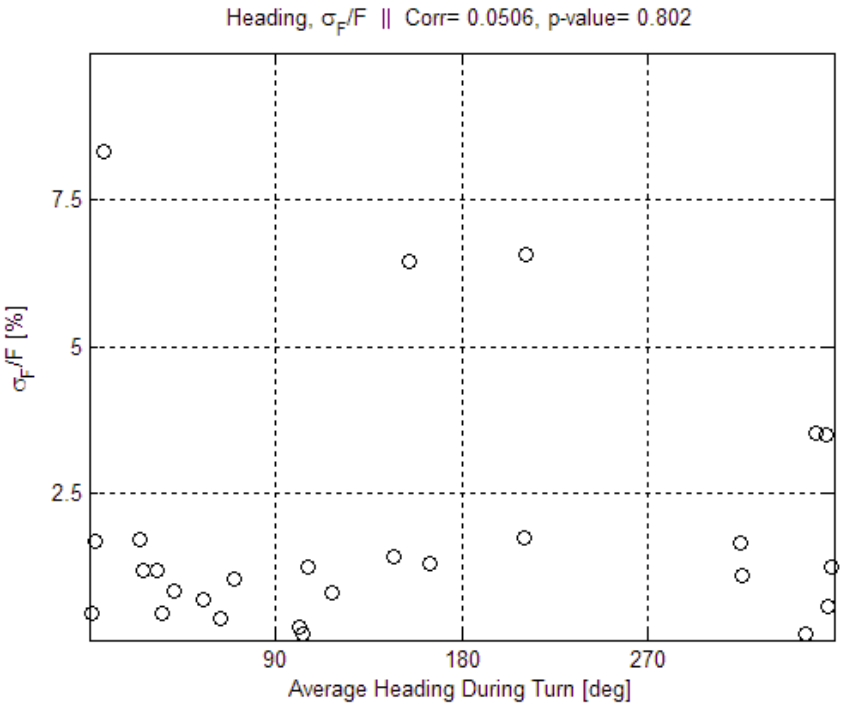

4.5 Test for systemaic error due to current

Although the GPS position is very precise after postprocessing, there exists a possible systematic error due to current or current eddies in the test area. The test area is nested inside a small cove and no current or current eddies are expected. The body of water is behind system of dykes, which are periodically opened to drain rain water. As such, there is no daily record of the current. A member of the faculty who was sailing nearby observed a Northwest current of less than 0.1 m/s. He was sailing in the center of the channel, however. To investige the possiblility of systematic error due to current, the relative uncertainty of the tow force measurement is plotted against the average heading during the turn in figure 4.5 above.

The tow force data is independent of the GPS position and is a quantity that should not be sensitive to the presense of current, assuming any current eddies with scale less than the sizeof the test segment are neglected. In other words, if the vessel and test segment are translating due to a current, the measured tow force would be the same as when there is no current, wheras the GPS track will be skewed in the direction of the current. For example, if the research vessel is steaming against the current, the velocity over ground derived from the GPS measurement will be less than the speed through water. The force measurement will remain unchanged whether the vessel sails against the current or with the current, assuming the same motor throttle is given.

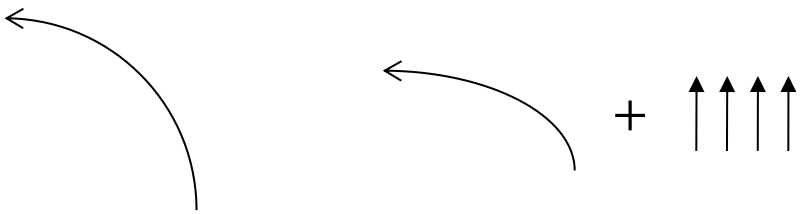

4.6 Possible decomposition of GPS track

In this experiment, the equilibrium configuration of the tow system performing a steady-radius turn is desired. A turn that was classified as steady based on a GPS track that is skewed due the presence of current would not in fact be steady. In figure 4.6, an example GPS track is shown (a), together with a possible decomposion into an unsteady turn and a current component (b). During a 30-second sample, even a modest current component will result in a significant error for L/r. For a turn with radius equal to 20 meters, a 0.033 m/s current will skew the track in excess of the limits for the refined data set. An unsteady turn should not come to an equilibrium state as well, which will return a larger standard deviation for the force sample. The relationship between the relative uncertainty of the force data and the turn heading is displayed in figure 4.5. The orientation of the turn and the relative error are uncorrelated, implying there is no current in the test area.

The research vessel and the test segment are also subject to environemntal loads associated with wind and waves. The wind was southeasterly and building during the afternoon of the tests, reaching 7 kn by the end of the afternoon. Though the test area was nested inside a cove and protected from wind chop, the Hollands Diep is a heavily trafficed waterway and occasionally the wake of a powerboat crossed the test area. The effect of the wind is evident in some of the GPS tracks. Assuming the wind does not act on the rope, the impact of this environmental load is only unsatisfactory turns.

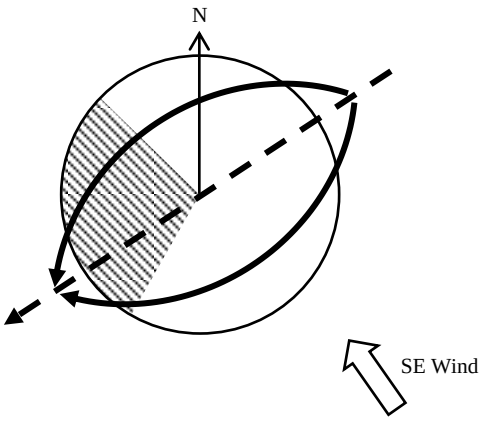

4.7 Compass rose showing directional characteristics of experiment data

There is a gap in the distribution of the runs as shown in the figure 4.7 aabove. Also shown is the meaning of the ‘average heading during turn’. No turns fall in the portion of the compass rose which is hatched.

The cause of this gap is not known. These headings are in the direction of the shore. Another contributing factor may be the swim ladder of the research vessel, which favored anti-clockwise turns. The waves generated by the occasional powerboat will have a high frequency (see figure 4.4), and are removed with the low-pass filter.

The test segment was towed in the wake of a small motor boat, and the effect of this disturbed inflow must be evaluated. From observations during the experiment, the tow-in angle was such that the test segment did not interact with the wake for all but the lowest tow-in angles. For this reason, the resistance measurement for straight towing is not a reliable value.

Results and Discussion

Based on previous work for submerged cables, the ratio between length and radius is used to organize the results. There are 27 turns, spanning a range of the ratio L/r= 0.4 to L/r= 3.4 and nicely encompassing the region of interest identified in the work of Chapman. [1]

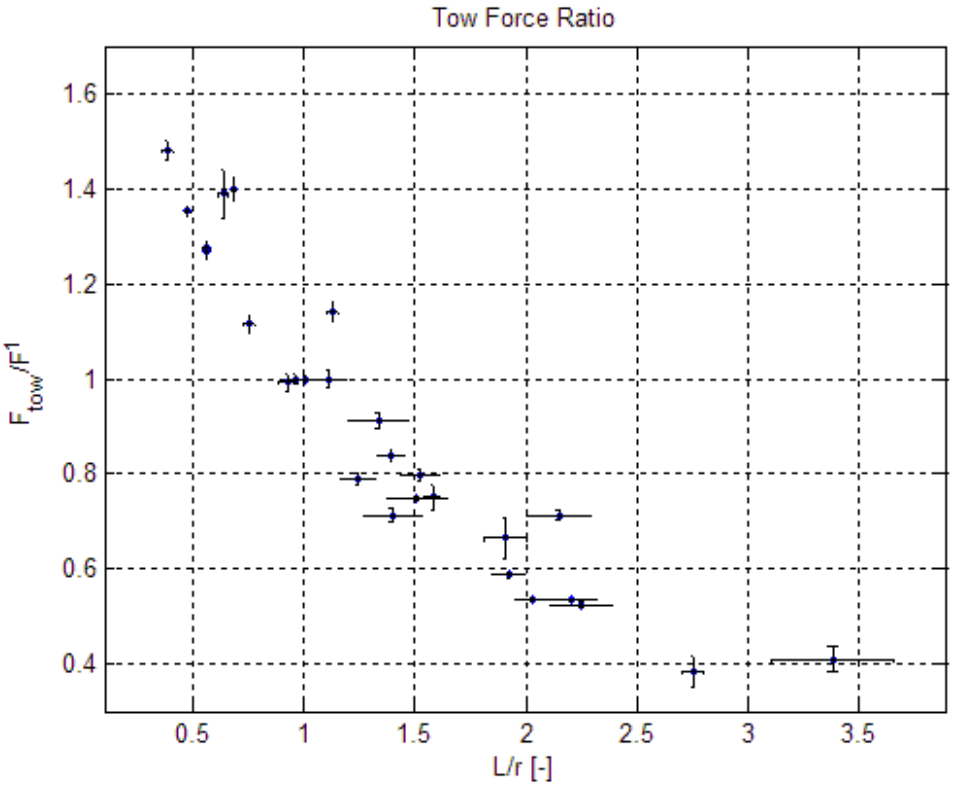

4.8 Tow force ratio for varying L/r

The surface-tow undergoing a turn can be characterized by a tow force reduction due to the turn. Unfortunately, the resistance measurements for straight towing are not reliable. Besides the question of inflow conditions, the tow speed for straight towing is approximately 0.5 m/s faster than during a turn. Instead of normalizing the force data with the straight tow value, the tow force for L/r= 1 was chosen as the reference because the data sets for all three lengths overlap at this value. The tow force ratio is presented in

figure 4.8 above. As in the work of Chapman, the tow force decreases for increasing L/r. Chapman identifies a critical radius, where the response of the system changes dramatically. For the floating system, no distinct transitions identified. For increasing values of L/r, the tow force ratio may reach the lower limits of approximately 0.4. However, there are few available data points in this region.

To interpret the relationship between tow force and tow-in angle, consider the equilibrium state for a differential cable element:

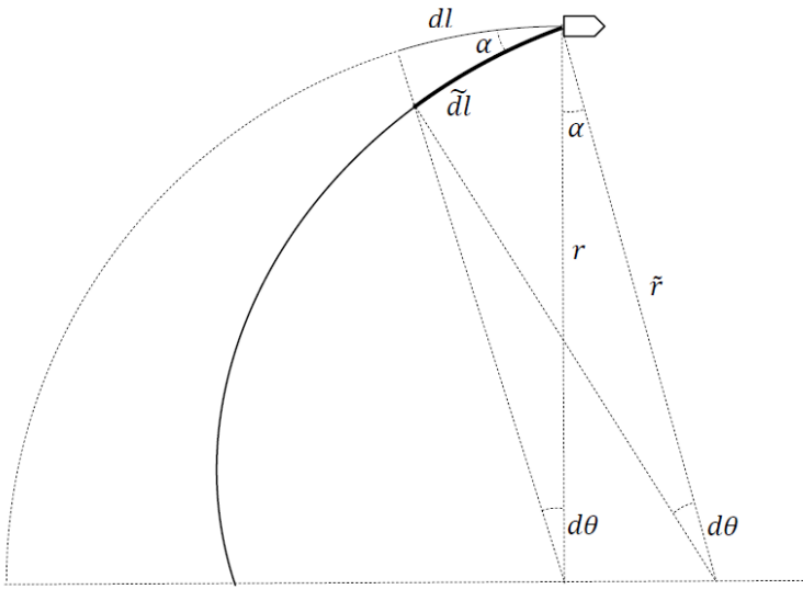

4.9 Geometry of cable system

In the figure above, the circular track of the tow vessel is shown. The test segment with tow-in angle α is shown spiralling toward the center of the turn. As outlined in the literature study, the origin of the tow-in angle is to create the cross-flow needed to generate a normal component of fluid force. If the ratio of tangential and normal fluid forces is constant along the test segment, the nessecary angle of attack is also constant. A constant-angle spiral is also known as a logarithmic spiral, and has many convienient properties. In fact, the internal tension will decrease along the segment, implying that the angle relative to the flow will as well. For the first cable segment, as shown in figure 4.9 above, it is assumed that the the property of self-similarity for logarithmic spirals allows the following expressions of $\tilde{dl}$ and $\tilde{r}$:

$$\tilde{dl} = dl \cos\alpha \qquad\qquad \tilde{r} = r \cos\alpha$$

The length of the spiral can be calculated. In a simplistic view of the system, when the length of absorbent exceeds the length of the spiral, there will be a slack portion near the end cable.

$$spiral\ length = \frac{r}{\sin\alpha}$$

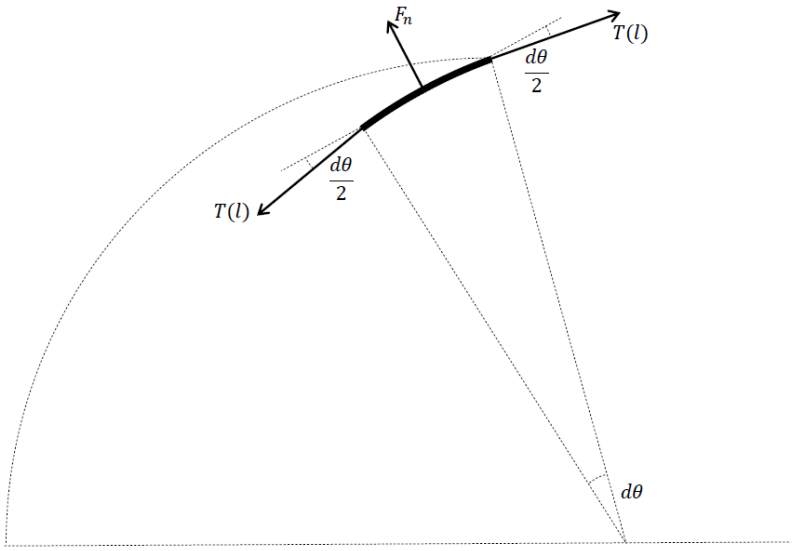

4.10 Force balance for cable element

From figure 4.10, equilibrium in the cable-normal direction requires that:

$$\mathrm{F_n}\widetilde{dl} = 2T(l)\sin\left(\frac{d\theta}{2}\right)$$

Here $\mathrm{F_n}$ is defined with units [N/m]. Assume a linear tension distribution along the test segment, where $T(0) = F^{tow}$ is the measured towing force:

$$T(l) = F^{tow}\left(1 - \frac{l}{L}\right)$$

The small angle approximation is valid for $\sin(d\theta)$. Substitute:

$$d\theta = \widetilde{dl}/_{\tilde{r}} = dl/_{r}$$

Integrate over the first meter of the test segment:

$$\int_{l=0}^{1} \mathrm{F_n} dl \cos\alpha = \frac{1}{r}\int_{l=0}^{1} F^{tow}\left(1 - \frac{l}{L}\right) dl$$

$$\mathrm{F_n} = \frac{1}{r\cos\alpha}\left[F^{tow}\left(l - \frac{1}{2L}l^2\right)\right]_0^1$$

$$\mathrm{F_n} = \frac{1}{r\cos\alpha}\left[F^{tow}\left(1-\frac{1}{2L}\right)\right]$$

This is an expression for the normal force [N/m], as a function of the experiemantal variables. The term $\frac{1}{2L}$, which accounts for the changing tension along the segment, is of the order 10^{-2} so it will be neglected. The normal drag force is simplfied to:

$$\mathrm{F_n} = \frac{F^{tow}}{r\cos\alpha}$$

The normal component of fluid force is normal to the cable element axis and does not contriubute to the measured tow force directly in. The expression relates the cable tension, measured as the tow force, and the force nessecary to induce the curvature defined by $\frac{1}{r}$. The cosine term arises from the relation between the arc length off the circular track and the arc length along the spiraling cable.

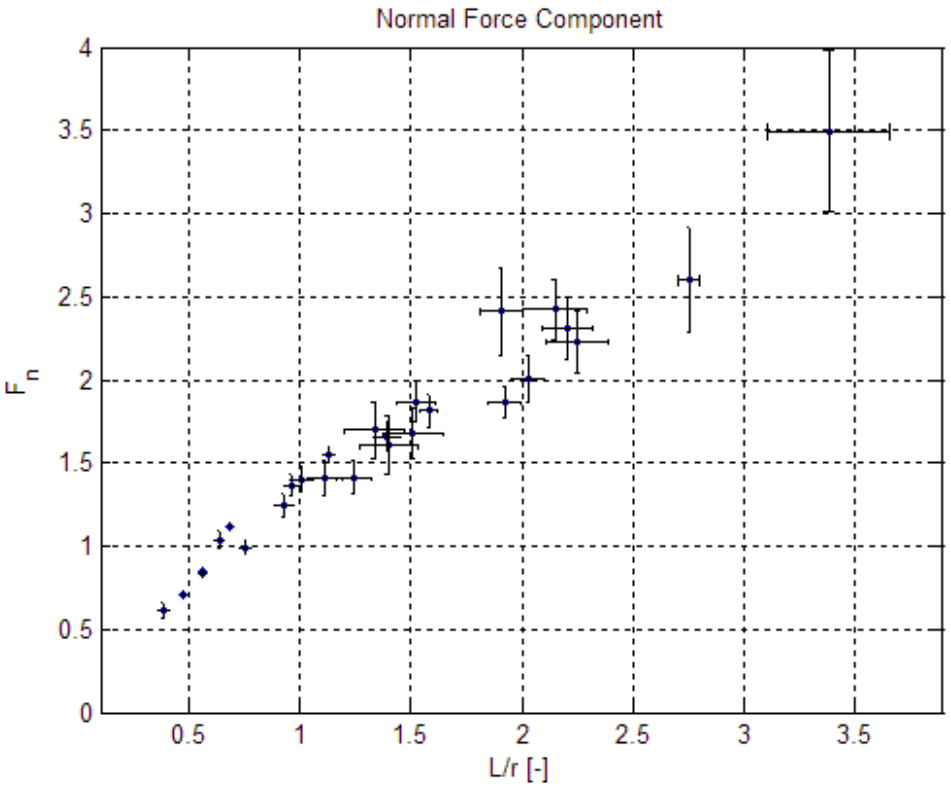

4.11 Normal force for varying L/r

This force, the normal fluid force, is plotted in the figure above. The quality of the data points deteriorates quickly for larger values of L/r. Larger values of L/r correspond to tighter turns, for which the limitations of the open water set up produce a higher relative error for both radius and tow-in angle.

The transient results are included for interested reader. This set of data was substantially impacted by the poor precision available when making a u-turn. Uncertainty about quantities such as the abruptness/smoothness of a turn and the influence of a varying tow speed, made a substantive analysis of this data impossible. The response of the measured variables and the system appears to be significantly dependent on the entire evolution of a given maneuver.

To account for varying tow speed and to compare results across varying test segment lengths, tow force measurements are non-dimensionalized as a tow force coefficient.

$$C_t = \frac{F^{tow}}{1/2\,\rho A L U^2}$$

Finally, a set of repeated runs was found and have been used to calculate the decay constant for the tow-in angle as the towed absorbent exits the turn. The exponential decay for tow-in angle occurs immediately after the towing vessel resumes a straight course.

A nice example that reveals some underlying physics is the following run 10, where the first turn begins broadly and ends sharply while the second turn evolves in the opposite way, sharply-to-broadly. For the first turn, labeled 10a, the radius of curvature is decreasing from approximately 50 meters to approximately 25 meters, whereas for the second turn, labeled 10b, the radius is increasing between the same values. It should be said that the increase or decrease are not steady, but such is the nature of open water testing. Nevertheless the impact of this difference in turn geometry can be found in the measured quantities. First, the tow-in angle for turn 10a is markedly smaller than that for turn 10b. For both samples, the turning radius is approximately equal after the towing vessel has travelled 70 m, while the tow in angle for 10a is approximately 8° smaller. Looking at the figures in a qualitative way, both tow-in angles come to a steady-state value, seen as a plateau. It is interesting to note that the average radius over that plateau for 10a is smaller than that for 10b, while the tow-in angles would suggest the opposite. The tow force coefficient during both turns is also shown. Besides being higher on average, the force coefficient for 10a increases during the turn, whereas for 10b it is seen decreasing.

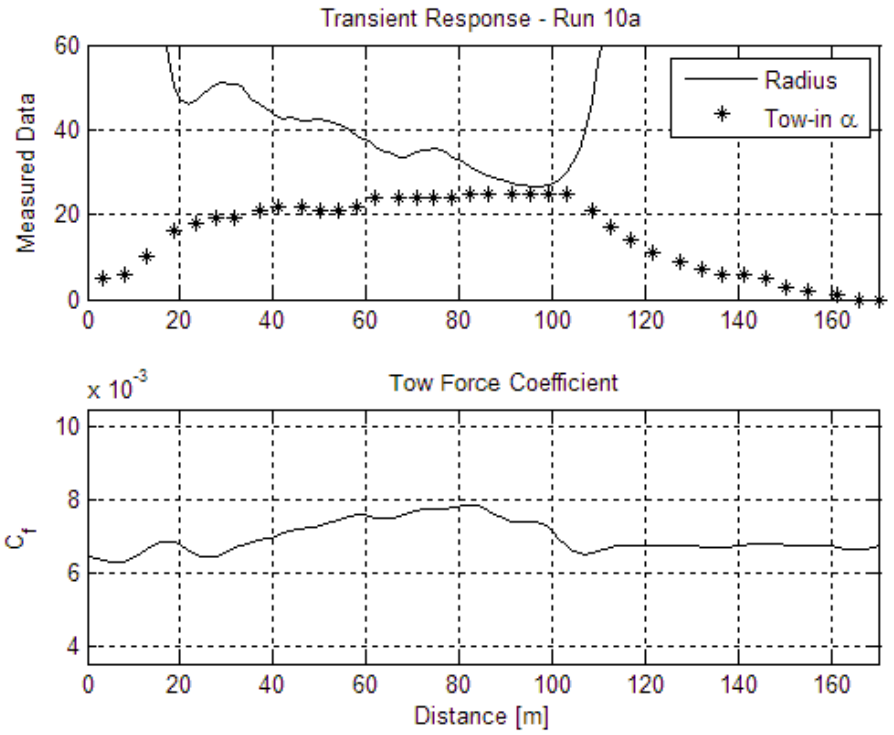

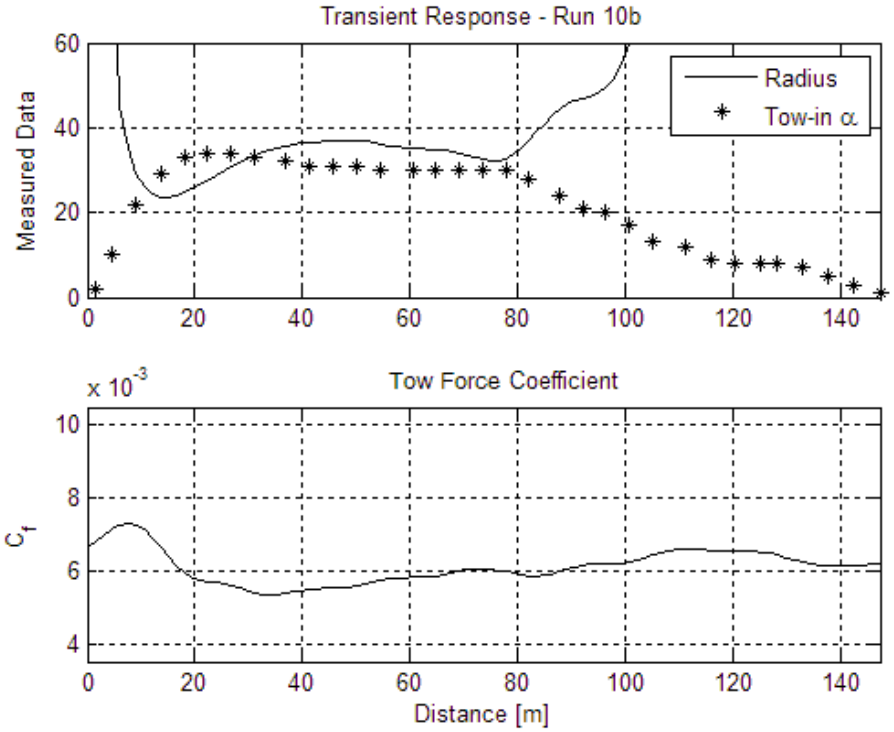

4.12 Transient response for run 10

Estimating Modeling Parameters

A primary goal of the experiments was to determine model parameters such as the coefficients of the fluid drag force. The refined datasets is used here. As will become clear, compromise was necessary to simultaneously reproduce kinematic variables such as the tow in angle and dynamic variables such as the towing force or the decay rate, τ.

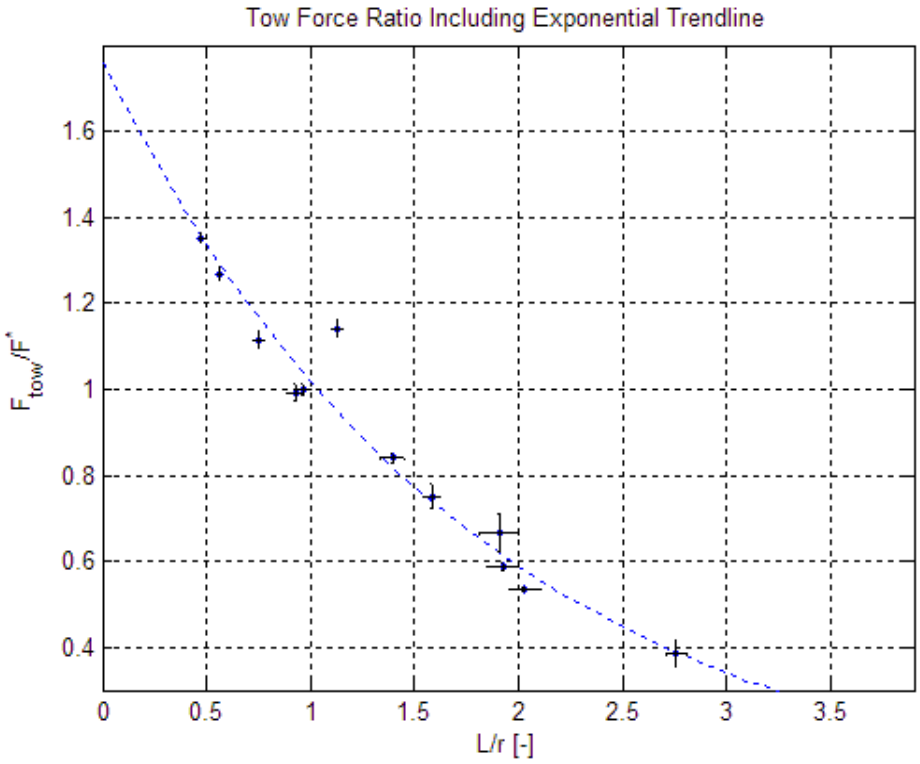

4.13 Tow force ratio showing fit - refined data set

The subset of the force ratio shown in figure 3.9 has been fitted to an exponential $fit = 1.76e^{-.548x}$. By taking the limit as L/r decreases to zero, it is possible to estimate the tow force for straight tow. The tangential drag coefficient is estimated using this value.

$$C_D{}^{\parallel} = \frac{1.76 * F^{tow}}{{}^{1}/_{2}\,\rho A L U^2}$$

The drag coefficient based on staight-tow measurements is calculated using the same principle. Finally, the results from the B.E.P. are given, as well as the analytical result from White [2] for axi-symmetric flows:

$$C_f = 0.0015 + \left(0.3 + 0.015\left(\frac{2L}{d}\right)^{0.4}\right) Re^{-\frac{1}{3}}$$

4.1 Estimates for tangential drag coefficient

$C_D^{\parallel}$ Estimate	length [m]	V_{tow} [m/s]	Tow Force [N]	$C_D^{\parallel}$ [-]	st.d
f(F/F[1])	43	1.5	95.568	0.0108	0.00456
	28	1.3	55.088	0.0127	0.00367
	15	1.06	27.456	0.0178	0.00289
Straight Tow	43	1.63	67	0.00650	0.0028
	28	1.53	40.3	0.00660	0.0061
	15	1.62	26.6	0.00730	0.0022
B.E.P.	9.94	0.99	22.97	0.0085	-
C_f (White)	43	1.5	-	0.00433	-
	28	1.3	-	0.00470	-
	15	1.06	-	0.00535	-

The tangential drag coefficient returned by using the tow force reduction ratio as outlined above is approximately twice as large as the other estimates, though the standard deviations of the estimates do overlap. The result of White is substantially smaller (approximatley a factor of three). It should be remembered that the equation from White is for a rigid cylinder completely submerged in uniform flow. The test segment was towed within the surface boundary layer, where a velocity gradient is present.

The B.E.P. result is closer to the Straight Tow result, however the surface roughness differs substantially. The B.E.P measurments were made using oil absorbent, which is smoother and has a larger diameter, giving a roughness height approximately ten times greater then for the polypropelene test segment. This is a significant discrepancy because the surface roughness will influence the boundary layer defelopment and the associated friction force. The Moody diagram, albeit for pipe flow, indicates that a factor ten in roughness corresponds to a factor two in friction coefficient. While the result of the B.E.P. cannot be used for direct comparison, they will be useful when estimating the drag coefficients for the Protei feasibility study.

For these reasons, the experimental values will be used to estimate this coefficient. Although these values are problematic as well due to the high-energy wake of the research vessel, and the unproven extrapolation by exponential fit, they are data from the free surface where physical behaivor is hard to predict. The influence of surface roughness should be awknowledged when translating these results for the polypropelene line to the smoother oil absorbent. The B.E.P. result provies a valuable benchmark.

The tow speed was caluculated using the GPS position. The components of flow for the first segment of cable are:

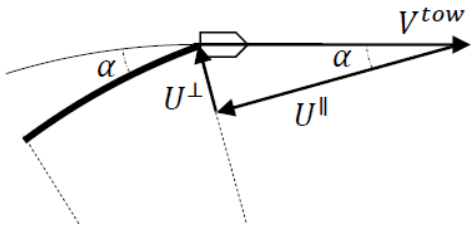

4.14 Decomposition of tow speed

Finally, one can solve for the drag coefficient:

$$C_D{}^{\perp} = \frac{\mathrm{F_n}}{{}^1\!/_2\,\rho T (U^{\perp})^2} = \frac{F^{tow}}{{}^1\!/_2\,\rho T r \cos\alpha\,(\mathrm{V_{tow}}\sin\alpha)^2}$$

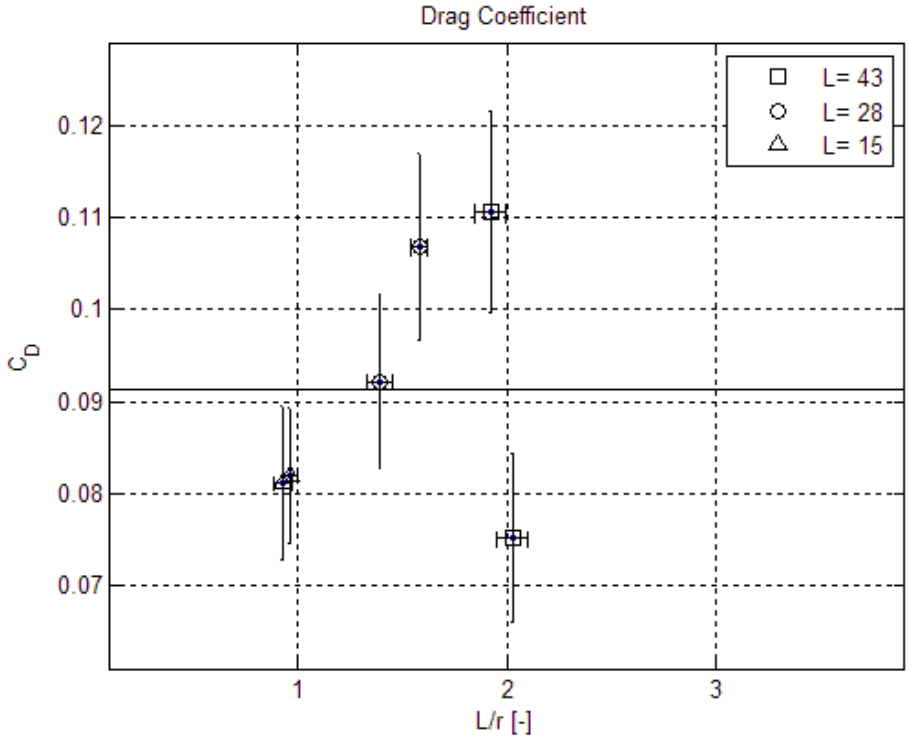

4.15 Drag coefficient - refined data set

The result is substantially lower than the expected value near to 1. This is a free surface effect where the interface with air imposes a strees-free boundary condition at the surface, allowing water to move much more freely than if the system were submerged. Air has a much lower viscosity and does not impart traction forces effectively. In essence, the oil absorbent will skim a layer of water along with it as it moves, a potentially helpful feature for the oil cleaning operations.

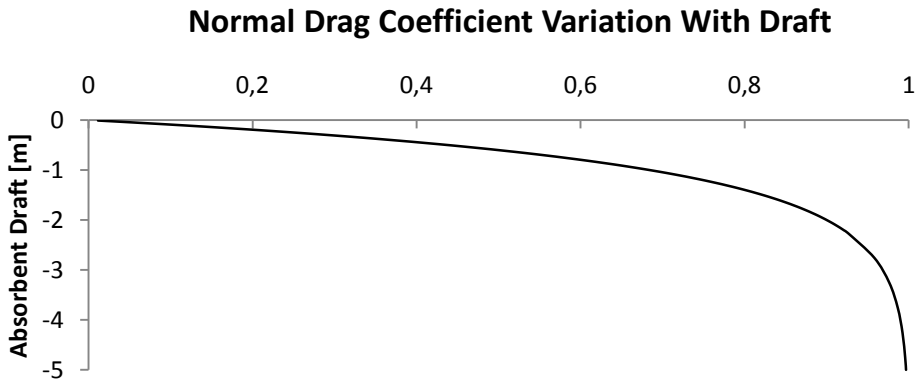

4.16 Exponential variation for normal drag coefficient

A proposed variation for the normal drag coefficient, $C_D{}^{\perp}$, is shown in figure 4.16 above. This profile is chosen based on the physical motivation provided in chapter 2, combined with the result of this experiment. To arrive at this profile, the following assumptions were made:

$$\lim_{z \to 0} C_D{}^{\perp} = 0$$

$$\lim_{z \to -\infty} C_D{}^{\perp} = 1$$

The first statement is deduced from the stress-free boundary condition at the surface. Keeping the same simplifications as in the previous analysis of chapter 2, a hypothetical cylinder with draft approaching zero will find the water unable to support fluid stresses and therefore unable to apply a normal fluid force. A detailed examination of influence of the free surface on normal fluid force is not part of this work. Fluid behavior around an obstruction in the vicinity of the free surface is complex to predict. A thorough study of this phenomenon should be conducted, perhaps including computational fluid dynamics, and experiments using cables with varying drafts. Finally, the second statement expresses that for bodies far removed from the free surface, $C_D{}^{\perp}$ returns to its characteristic value of 1.

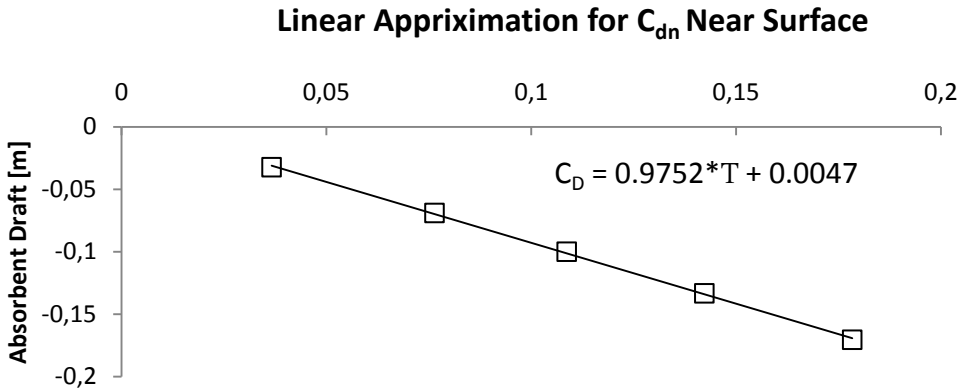

4.17 Linear function for normal drag coefficient

An exponential profile for the normal drag coefficient is assumed, shown in figure 4.16. For the oil absorbent material, with a radius equal to 0.1 m, the range of operating drafts is shown in the figure above. Depending on the density of the oil slick, the draft corresponding to be fully laden absorbent is approximately 0.17 m. Over this range, the exponential profile can be approximated with a linear function as shown in figure 4.17 above.

To establish a reference for the transient behavior of the numerical model, the decay constant for the tow-in angle is estimated. The nature of open water tests is uncontrolled. It was challenging to establish sensible criteria for transient samples.

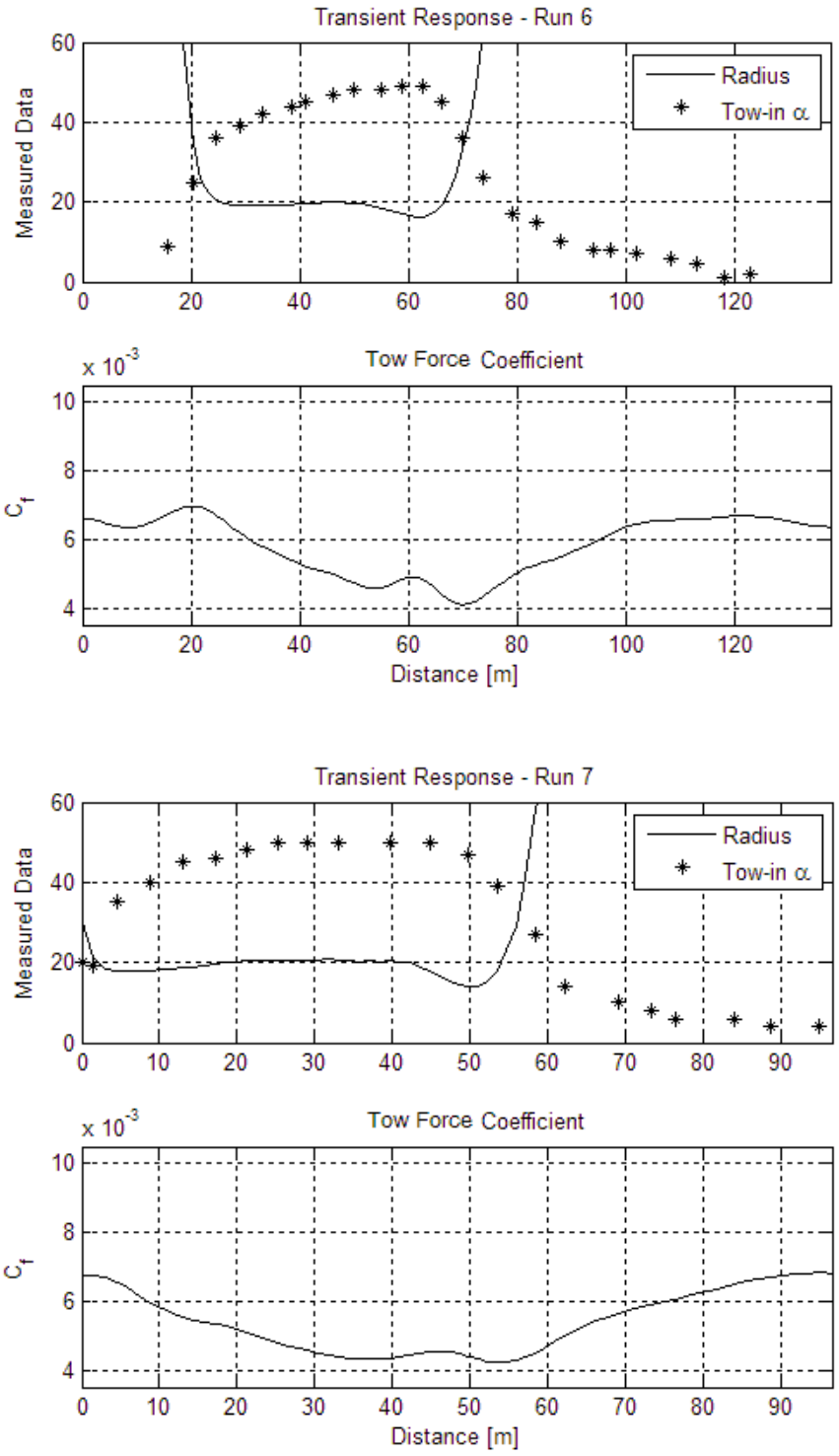

4.18 Samples for transient analysis

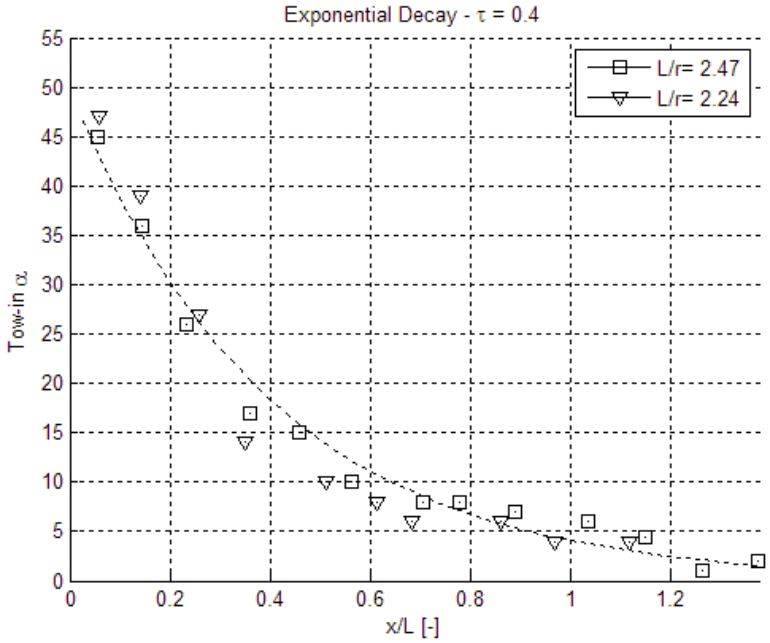

4.19 Exponential fit for tow-in angle during sail away

Shown on the previous pages, runs numbers 6 and 7 are identified based on the comparable geometry of the turns, and the similarities in behavior of the tow force coefficient. Shown in the figure above, the tow in angle is plotted against the non-dimensionalized distance, x/L. This choice was made initially to compare results from different test segment lengths, it also serves to normalize for variations in tow speed. Based on the exponential fits shown above the decay constant is equal to 0.4, meaning that after sailing a distance equal 40% of the test segment length, the tow in angle has reduced by 63%. It is important to remember that this result is a very crude and may only be valid for one value of L/r.

Experiments Overview

It has been shown that a flexible body towed on the surface has a similar behavior to the submerged oceanographic systems of chapter 2. A large set of data was obtained for the steady-state experiments. It was possible to derive estimates for the tangential and normal drag coefficients. A depth-varying normal drag coefficient is proposed based on physical motivation in chapter 2 and the experimental results. The tangential drag coefficient is estimated for polypropylene line, which has a roughness factor of approximately 0.1. When an estimate for the absorbent is made, the B.E.P. result will be the most relevant. A substantive analysis of transient response was impossible because there were few repeated runs. A more systematic method for defining the research vessel track is needed. The following estimates are made:

$C_D{}^{\parallel}$	0.011
$C_D{}^{\perp}$	0.09 $= 0.9752 * \mathrm{T} + 0.0047$
τ	0.4

5

Verification

The numerical model is evaluated on its physicality and its numerical properties. First, some time is taken to elucidate the meaning of each term in the system of equations. This will clarify the mathematics of Kane's method for the reader, and provide a verification of the sometimes cumbersome expressions that were derived.

A central property of cables and of oil absorbent is that they cannot support a compressive load. By selecting the rigid body model, this material nonlinearity was omitted. The cable tension, which is a non-contributing force in the nomenclature of Kane' s method, is derived to verify that this assumption has not been violated and has not influenced system behavior.

A rudimentary proportional-gain controller was implemented to achieve a constant towing speed during the maneuver. The controller gain is varied to examine how this parameter influences the system response.
Next, the numerical properties of the system are examined. Though an analytical relationship between spatial and temporal step sizes was not found, a stability threshold was identified by trial and error. The effect of scaling system geometry was also examined. Finally, the system response is tuned using results from the experiments. As will be shown, a compromise was necessary to match the experiments results for tow-in angle and tow force.

Physical Interpretation

The application of Kane's method may have obscured the physics of the problem. To restore confidence in this solution technique, each term will be analyzed using simple examples of the absorbent system.

Kane's equation reads:

$$\sum_{i=1}^{n} m_i \vec{a}_i \cdot \frac{\partial \vec{v}_i}{\partial \dot{q}_j} = \sum_{i=1}^{n} \vec{F}_i \cdot \frac{\partial \vec{v}_i}{\partial \dot{q}_j} , \qquad j = 1, \dots, P$$

Following from the interpretation of the partial velocity given above, one can recognize the mechanism underlying Kane's method. Only *active* forces and inertial forces are evaluated, based on their activity along the degrees of freedom j. This is expressed as the inner product of each force contribution with the partial velocity vector, $\frac{\partial \vec{v}_i}{\partial \dot{q}_j}$. The partial velocity evaluated for $q_j = \theta_j$ is:

$$\frac{\partial \vec{v}_i}{\partial \dot{\theta}_j} = \langle -l \ \sin\theta_j \, , l \ \cos\theta_j \rangle$$

This expression gives the direction normal to segment j, multiplied by the segment length l. To find the system of equations for coordinate q_j, each force contribution is projected onto this 'partial velocity' vector. The factor l can be interpreted as a moment arm, consistant with the fact that the general coordinates are angles.

For $q_1 = b$, during the sail-away stage, the partial velocity is:

$$\frac{\partial \vec{v}_i}{\partial \dot{b}} = \langle 0,1 \rangle$$

It can be verified that only forces in the $\hat{\boldsymbol{\jmath}}$-direction are retained.

The notation is cumbersome due to the distinction between the set-up variables, $\{b, \theta_c\}$ and the angles $\{\theta_1, \theta_2, \dots, \theta_N\}$, which describe the absorbent system. The reader should bear in mind that the set-up variables only contribute to the local flow speeds as part of the expression for the fluid forces and only as an added acceleration in the expression for the inertial force. This is most clearly seen in the matrix form of the system equations. The author recognizes that a simpler modeling can be achieved by defining the path of the turn with a constraint function rather than using the set-up variables $\{b, \theta_c\}$.

The mass matrix is arranged so that m_{jk} can be precomputed. The setup variables do not contribute to the total mass.

$$\mathbb{M}_{jk} = m_{jk} l_k l_j \cos(\theta_j - \theta_k)$$

$$m = \begin{bmatrix} Ndm & Ndm & (N-1)dm & (N-2)dm & \cdots & dm \\ Ndm & Ndm & (N-1)dm & (N-2)dm & \cdots & dm \\ (N-1)dm & (N-1)dm & (N-1)dm & (N-2)dm & \cdots & dm \\ (N-2)dm & (N-2)dm & (N-2)dm & (N-2)dm & \cdots & dm \\ \vdots & \vdots & \vdots & \vdots & \ddots & \vdots \\ dm & dm & dm & dm & \cdots & dm \end{bmatrix}$$

To aid in interpreting the significance of each component of the generalized fluid drag term, consider a system where the oil absorbent has been discretized into three segments (N=3):

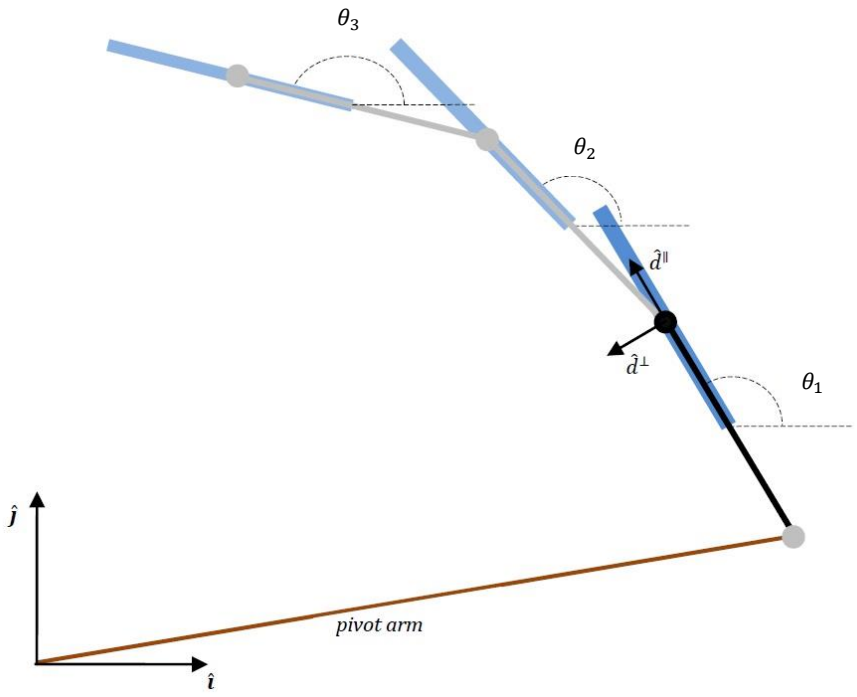

5.1 Model configuration (a)

The figure above represents a steady-state configuration for the towed cable during the u-turn stage. Denoting the fluid force terms by $F_i^{\parallel}$ and $F_i^{\perp}$ and writing out the summation over *i* for the second generalized coordinate, $\dot{\theta}_1$:

$$\vec{F}_{\dot{\theta}_1}^{drag} = \sum_{i=1}^{P} \left[\vec{F}_i^{\parallel} \cdot \frac{\partial \vec{v}_i}{\partial \dot{\theta}_1} + \vec{F}_i^{\perp} \cdot \frac{\partial \vec{v}_i}{\partial \dot{\theta}_1} \right]$$

$$\vec{F}_{\dot{\theta}_1}^{drag} = F_c^{\parallel}\langle -cos\theta_c, -sin\theta_c\rangle \cdot \frac{\partial \vec{v}_c}{\partial \dot{\theta}_1} + F_c^{\perp}\langle sin\theta_c, -cos\theta_c\rangle \cdot \frac{\partial \vec{v}_c}{\partial \dot{\theta}_1}$$
$$+ F_1^{\parallel}\langle -cos\theta_1, -sin\theta_1\rangle \cdot \frac{\partial \vec{v}_1}{\partial \dot{\theta}_1} + F_1^{\perp}\langle sin\theta_1, -cos\theta_1\rangle \cdot \frac{\partial \vec{v}_1}{\partial \dot{\theta}_1}$$
$$+ F_2^{\parallel}\langle -cos\theta_2, -sin\theta_2\rangle \cdot \frac{\partial \vec{v}_2}{\partial \dot{\theta}_1} + F_2^{\perp}\langle sin\theta_2, -cos\theta_2\rangle \cdot \frac{\partial \vec{v}_2}{\partial \dot{\theta}_1}$$
$$+ F_3^{\parallel}\langle -cos\theta_3, -sin\theta_3\rangle \cdot \frac{\partial \vec{v}_3}{\partial \dot{\theta}_1} + F_3^{\perp}\langle sin\theta_3, -cos\theta_3\rangle \cdot \frac{\partial \vec{v}_3}{\partial \dot{\theta}_1}$$

The first terms in the summation, corresponding to the pivot arm, are zero because the fluid drag terms are zero. Also, the partial velocity will be zero, since the motion, $\vec{v}_c$, of this coordinate does not depend on outboard segments. The inner product is evaluated for the remaining terms:

$$\frac{\partial \vec{v}_i}{\partial \dot{\theta}_1} = \langle -lsin\theta_1, lcos\theta_1\rangle$$

$$\vec{F}_{\dot{\theta}_1}^{drag} = l\left[F_1^{\parallel}\sin(\theta_1 - \theta_1) + F_2^{\parallel}\sin(\theta_1 - \theta_2) + F_3^{\parallel}\sin(\theta_1 - \theta_3)\right]$$
$$- l[F_1^{\perp}\cos(\theta_1 - \theta_1) + F_2^{\perp}\cos(\theta_1 - \theta_2) + F_3^{\perp}\cos(\theta_1 - \theta_3)]$$

The first term in each bracket is the contribution of the fluid element to its own generalized coordinate. The tangential component, being aligned with the segment and therefore suppressed by the constraint, does not play a role, while the normal component is fully transmitted. The rest of the summation expresses the influence of the tangential and normal fluid forces outboard of the first segment on the general coordinate θ_1. The setup variable, in this case θ_c, appears in the expression for F_i as part of the calculation of the local flow speed.

$$F_i^{\parallel} = \frac{1}{2}\rho_w A^{\parallel} {C_D}^{\parallel}\left[\dot{b}sin\theta_i + r_c\omega_c\sin(\theta_i - \theta_c) + \sum_{k=1}^{i} l_k\omega_k\sin(\theta_i - \theta_k)\right]\langle -cos\theta_i, -sin\theta_i\rangle$$

$$F_i^{\perp} = \frac{1}{2}\rho_w A^{\perp} {C_D}^{\perp}\left[\dot{b}cos\theta_i + r_c\omega_c\cos(\theta_i - \theta_c) + \sum_{k=1}^{i} l_k\omega_k\cos(\theta_i - \theta_k)\right]\langle sin\theta_i, -cos\theta_i\rangle$$

The significance of each summation is best understood by looking at the matrix form given in chapter 3. The expressions for $F_i^{\parallel}$ and $F_i^{\perp}$ contain a summation over *k*, giving the local flow speed. The difference $(\theta_i - \theta_k)$ expresses the orientation of the flow with respect to the segment. These force vectors are parallel or perpendicular to each segment. The matrix form of $\mathbb{F}$ is lower triangular. The velocity at each segment in relation to the origin is expressed as the sum of inboard generalized speeds. The projection of these forces on to the generalized coordinates gives the upper triangular matrices $\mathbb{P}$, indicating that only outboard forces contributes to the dynamics for each generalized coordinate.

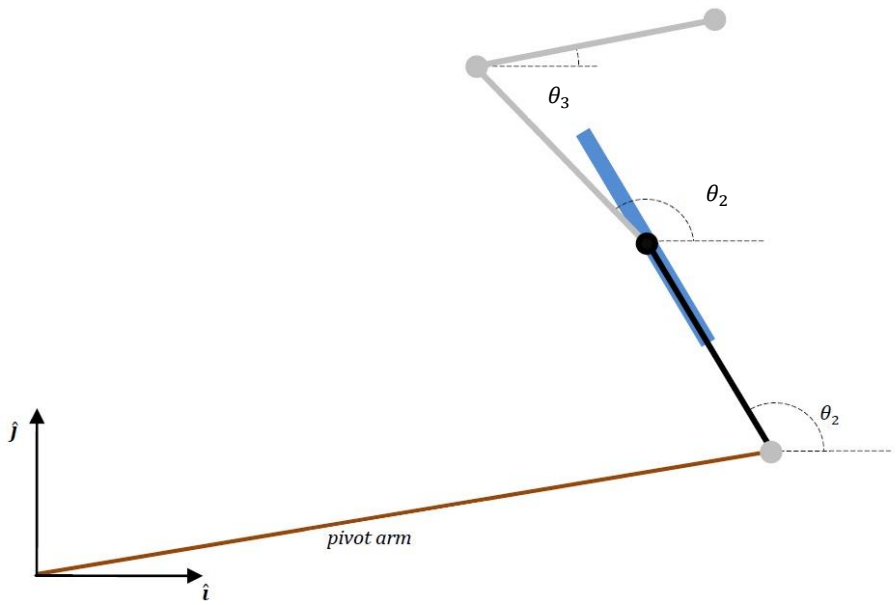

5.2 Model configuration (b)

Expanding these summations for the system shown above, again with *j*=2 and N=3. The angles are chosen in order to affirm the physical interpretation of the normal fluid drag forces resisting cross-track excitations. With $\theta_1 - \theta_2 < {}^{\pi}/_{2}$ and $\theta_1 - \theta_3 > {}^{\pi}/_{2}$, the contributions by normal fluid forces are to the general coordinate $q_2 = \theta_1$ are:

$$\vec{F}^{\perp}_{\dot{\theta}_1} = -\sum_{i=1}^{P} l\cos(\theta_2 - \theta_i)F_i^{\perp} \qquad \theta_1$$

$$= -lF_1^{\perp} - l\cos(\theta_1 - \theta_2)F_2^{\perp} - l\cos(\theta_1 - \theta_3)F_3^{\perp}$$

The last term, $-l\cos(\theta_1 - \theta_3)F_3^{\perp}$, will oppose the other contributions to the normal fluid drag because the cosine returns a negative value. Keeping in mind the orientation of the generalized coordinate θ_1, one can confirm that the contribution by the normal fluid drag of segment 3 should have a positive sense. With some imagination, it is possible to attribute the minus sign in this term to the restoring nature of the normal drag component. This behavior is of central importance for this study, as it is the normal component that will act to keep the oil absorbent faithfully following the Protei vessel around a turn.

Test for Compression in Cable

One of the key assumptions made in designing the present model is that the cable remains approximately under tension during the maneuver. It is possible to retrieve the tension in the cable by solving to the non-contributing forces. This is described in Kane, p 114 [3]. The dynamic solution for the motions has already been found using the equations formulated in Chapter 3. The following is an algebraic post-processing.

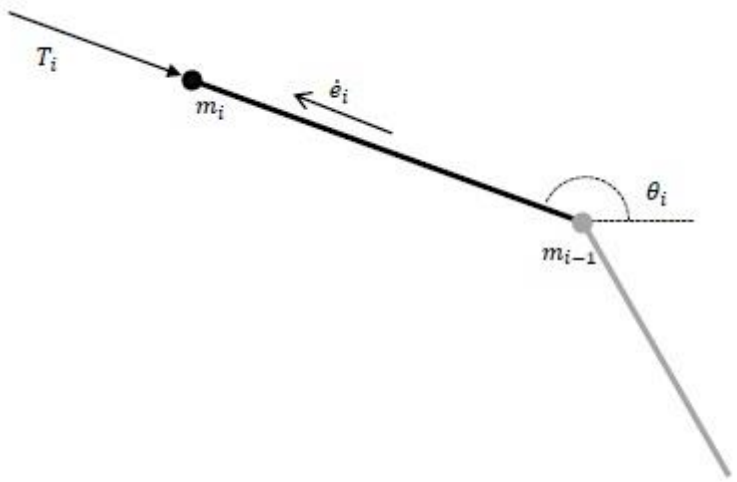

5.3 Fictitious speed $\dot{e}_i$ and cable tension

Define a new set of general speeds, $\dot{q}_j = \dot{e}_i$, which are aligned with each segment as shown. Although these degrees of freedom are in violation of the constraints, they will lead to a new set of equations for the non-contributing forces. In essence, these are the forces needed to satisfy the constraints: the tension T_i in each cable segment.

$$\vec{v}_i = \left[-r_c \omega_c \sin\theta_c - \sum_{k=1}^{i} l_k \omega_k \sin\theta_k + \sum_{k=1}^{i} \dot{e}_k \cos\theta_k \right] \hat{\boldsymbol{\imath}} + \left[\dot{b} + r_c \omega_c \cos\theta_c + \sum_{k=1}^{i} l_k \omega_k \cos\theta_k + \sum_{k=1}^{i} \dot{e}_k \sin\theta_k \right] \hat{\boldsymbol{\jmath}}$$

From the definition of a generalized speed:

$$\frac{\partial \vec{v}_i}{\partial \dot{q}_j} = \hat{d}_i^{\parallel} = \langle \cos\theta_i \,,\, \sin\theta_i \rangle$$

Arranged in tabular format as before:

5.2 Partial velocities for cable tension

	$\dot{b}, \vec{v}_c$	$\vec{v}_1$	$\vec{v}_2$	$\vec{v}_3$	...	$\vec{v}_N$
$\dot{q}_{P+1} = \dot{e}_1$	0	$\left\langle \begin{matrix}\cos\theta_1\\ \sin\theta_1\end{matrix} \right\rangle$	$\left\langle \begin{matrix}\cos\theta_1\\ \sin\theta_1\end{matrix} \right\rangle$	$\left\langle \begin{matrix}\cos\theta_1\\ \sin\theta_1\end{matrix} \right\rangle$	...	$\left\langle \begin{matrix}\cos\theta_1\\ \sin\theta_1\end{matrix} \right\rangle$
$\dot{q}_{P+2} = \dot{e}_2$	0	0	$\left\langle \begin{matrix}\cos\theta_2\\ \sin\theta_2\end{matrix} \right\rangle$	$\left\langle \begin{matrix}\cos\theta_2\\ \sin\theta_2\end{matrix} \right\rangle$	...	$\left\langle \begin{matrix}\cos\theta_2\\ \sin\theta_2\end{matrix} \right\rangle$
$\dot{q}_{P+3} = \dot{e}_3$	0	0	0	$\left\langle \begin{matrix}\cos\theta_3\\ \sin\theta_3\end{matrix} \right\rangle$	...	$\left\langle \begin{matrix}\cos\theta_3\\ \sin\theta_3\end{matrix} \right\rangle$
⋮	⋮	⋮	⋮	⋮	⋱	⋮
$\dot{q}_{P+N} = \dot{e}_N$	0	0	0	0	...	$\left\langle \begin{matrix}\cos\theta_N\\ \sin\theta_N\end{matrix} \right\rangle$

The internal tension for each segment is equal to T_i. Using the terminology of Kane, this is a non-contributing force. In the original formulation, the equations were simplified by eliminating the explicit solution of this force. By introducing fictitious degrees of freedom, $\dot{e}_i$, it is possible to retrieve these forces. T_i is aligned with each segment as shown in figure 5.3, and is exactly sufficient to oppose the sum of all force contributions aligned with the vector $\hat{d}_i^{\parallel} = \langle \cos\theta_i\,,\ \sin\theta_i \rangle$.

Now it remains to evaluate the individual contributions to the inertial and active forces. Beginning with the inertia term:

$$F_{\dot{e}_j}{}^* = \sum_{i=1}^{N} m_i \vec{a}_i \cdot \frac{\partial \vec{v}_i}{\partial \dot{e}_j}\,, \qquad j = 1, \dots, N$$

$$F_{\dot{e}_j}{}^* = \sum_{k=1}^{N} \left(\sum_{\substack{s=j \\ s \geq k}}^{N} m_s \right) \begin{pmatrix} -l_k(\dot{\omega}_k \sin\theta_k) \\ l_k(\dot{\omega}_k \cos\theta_k) \end{pmatrix} \cdot \begin{pmatrix} \cos\theta_j \\ \sin\theta_j \end{pmatrix}$$

$$F_{\dot{e}_j}{}^* = \sum_{k=1}^{N} m_{jk} l_k \dot{\omega}_k \left(-\sin\theta_k \cos\theta_j + \cos\theta_k \sin\theta_j \right)$$

$$F_{\dot{e}_j}{}^* = \sum_{k=1}^{N} m_{jk} l_k \sin\left(\theta_j - \theta_k\right) \dot{\omega}_k\,, \qquad j = 1, \dots, N$$

$$\boldsymbol{F}^* = \mathbb{M}^{\boldsymbol{e}} \dot{\omega}$$

The summations over *s* and *k* have been combined into the matrix $\mathbb{M}^{\boldsymbol{e}}$, which is marked with *e* to distinguish it from the previous mass matrix.

The fluid forces are evaluated similarly. They are briefly derived below. Keeping the compact expression of the normal and tangential drag force, which keep the same form as before:

$$\vec{F}_i^{drag} = F_i^{\parallel}\langle -cos\theta_i, -sin\theta_i\rangle + F_i^{\perp}\langle sin\theta_i, -cos\theta_i\rangle, \qquad i = 1, \dots, N$$

Returning to the definition of an active force:

$$F_{\dot{e}_j}^{drag} = \sum_{i=1}^{N} \vec{F}_i^{drag} \cdot \frac{\partial \vec{v}_i}{\partial \dot{e}_j}, \qquad j = 1, \dots, N$$

$$F_{\dot{e}_j}^{drag} = \sum_{i=1}^{N} F_i^{\parallel}\langle -cos\theta_i, -sin\theta_i\rangle \cdot \langle \cos\theta_j, \sin\theta_j \rangle + F_i^{\perp}\langle sin\theta_i, -cos\theta_i\rangle \cdot \langle \cos\theta_j, \sin\theta_j \rangle$$

$$F_{\dot{e}_j}^{drag} = \sum_{i=1}^{N} -F_i^{\parallel} cos(\theta_j - \theta_i) - F_i^{\perp} sin(\theta_j - \theta_i), \qquad j = 1, \dots, N$$

The system of equations for each partial speeds $\dot{e}_j$ can now be written to solve for the internal tension, T_j.

$$T_j = -\left(\sum_{k=1}^{N} m_{jk} l_k \dot{\omega}_k \sin(\theta_j - \theta_k) + \sum_{i=j}^{N} F_i^{\parallel} cos(\theta_j - \theta_i) + F_i^{\perp} sin(\theta_j - \theta_i) \right), \qquad j = 1, \dots N$$

$$\mathbb{T} = -(\mathbb{M}^{e}\dot{\boldsymbol{\omega}} + \mathbb{P}^{c}\mathbb{F}^{\parallel}\boldsymbol{\omega} + \mathbb{P}^{c}\mathbb{F}^{\perp}\boldsymbol{\omega})$$

The matrices $\mathbb{P}$ are defined in the same way as before but have switched roles.

The expression for internal tension was implemented in Matlab. The code, checkT.m, can be found in Appendix B.

The internal tension is plotted against a non-dimensional time, which has been scaled by the time needed to sail the semicircular path of the U-turn. This scaling will be used throughout so that results for turns with differing geometry can be compared.

$$T^* = \frac{TU}{r}$$

Using this scaling, the duration of the u-turn stage is π.

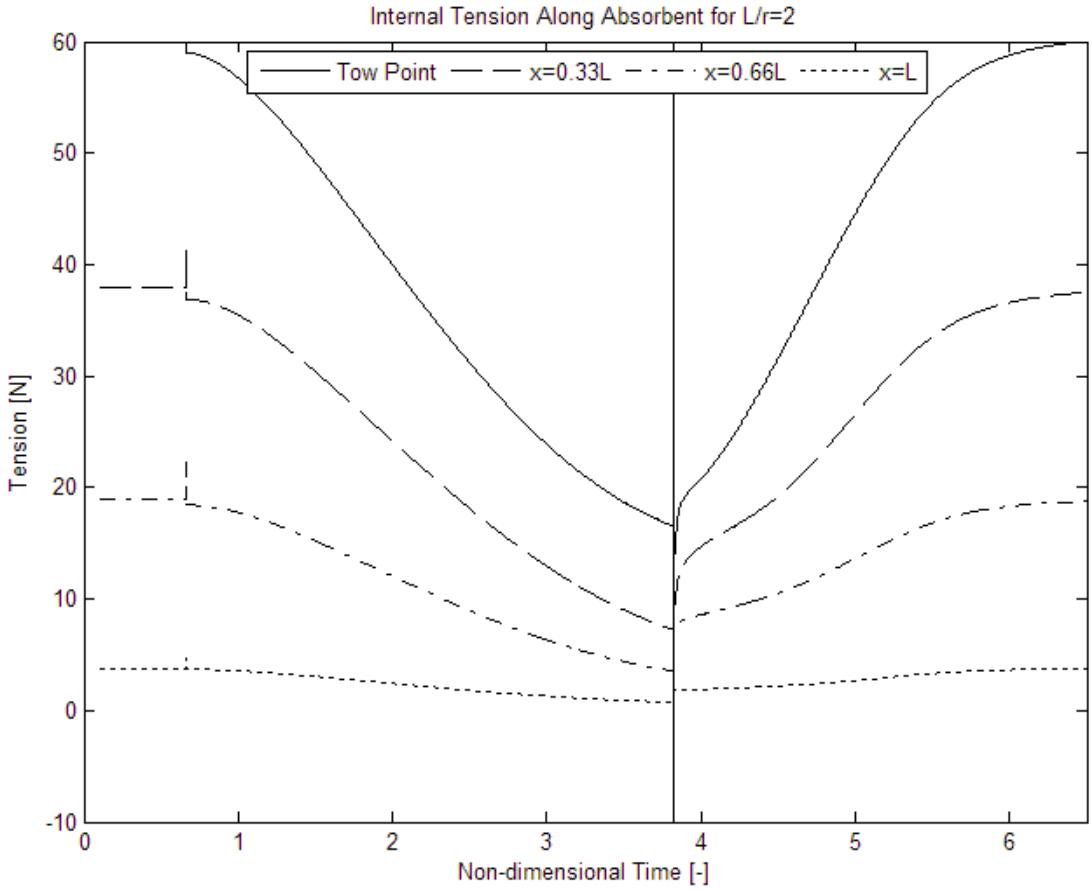

5.4 Internal tension for L/r=2

The solid line is the tension at the towing point, and is equal to towing force as expected. The remaining lines give the tension in the cable for three locations along the absorbent length. The dotted line, for x=L, is the tension contribution of the final incremental length.

The transitions between modeling stages are marked by some numerical issues. The evaluation of the second derivative for these transitions is not yet satisfactory. During this simulation, a constant speed is enforced using a controller. At the transition from the U-turn to the sail away stage, the towing force increases nearly impulsively to maintain the constant speed, causing a abrupt change in the internal tension as well.

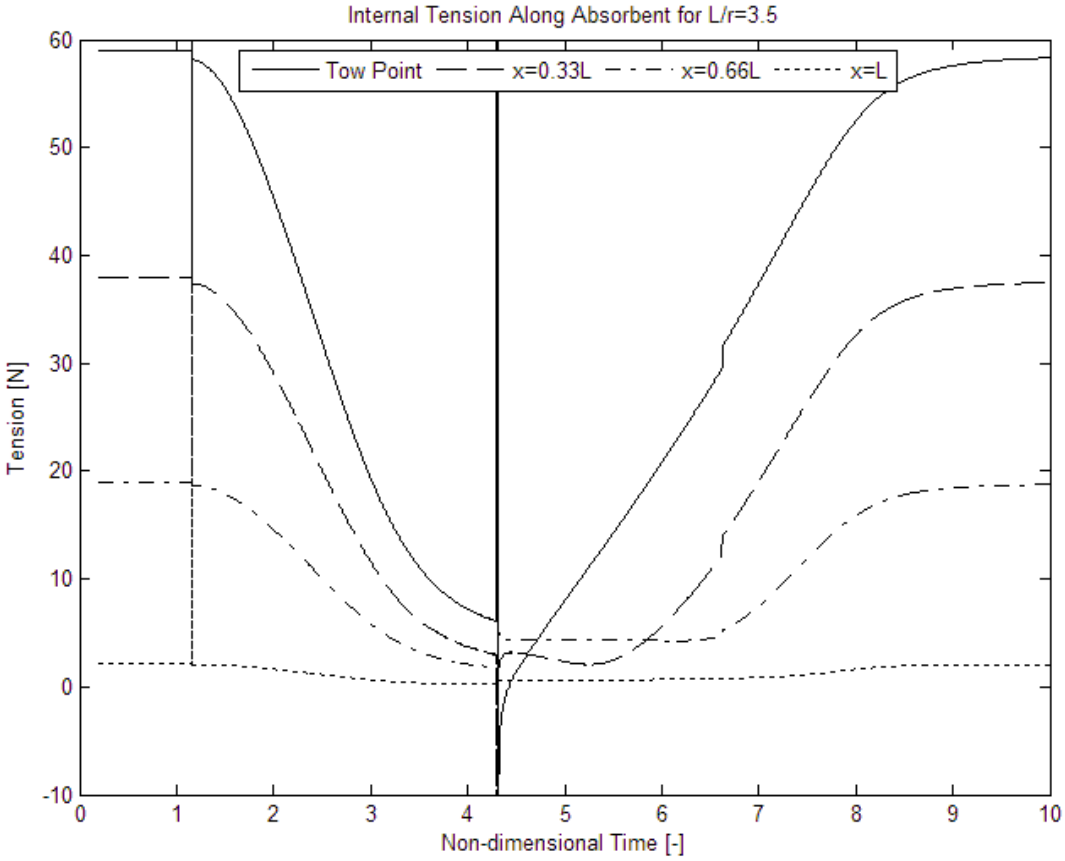

5.5 Internal tension for L/r=3.5

One of the modeling assumptions is that the internal tension remains nonnegative. As the parameter L/r increases, a dip in internal tension is seen travelling along the cable.

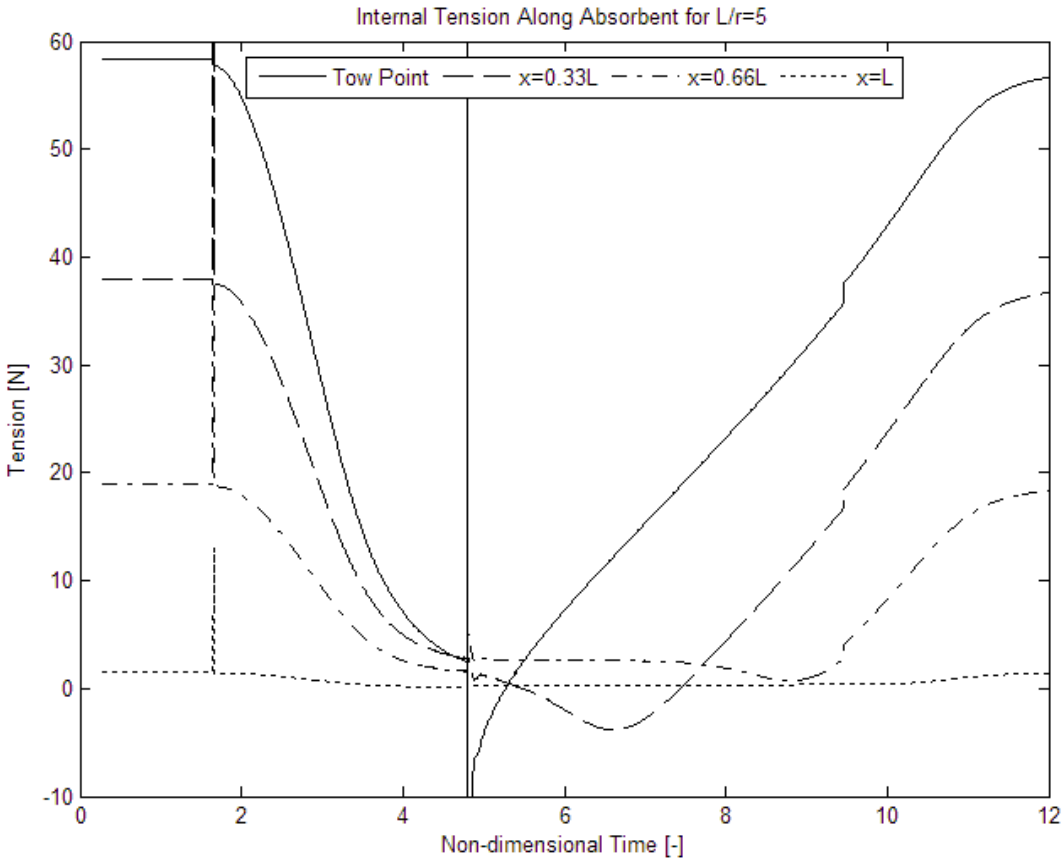

5.6 Internal tension for L/r=5

Figure 5.6 above shows a turn (L/r=5) where a traveling wave of compression is observed. At the beginning of the sail away stage (at the second numerical error), locations along the absorbent successively experience a dip in tension. This behavior was predicted in the literature study, it is the moment when the absorbent is changing direction. Nonlinear material response is not included in this model, leading to compression along the cable rather than a slack cable.

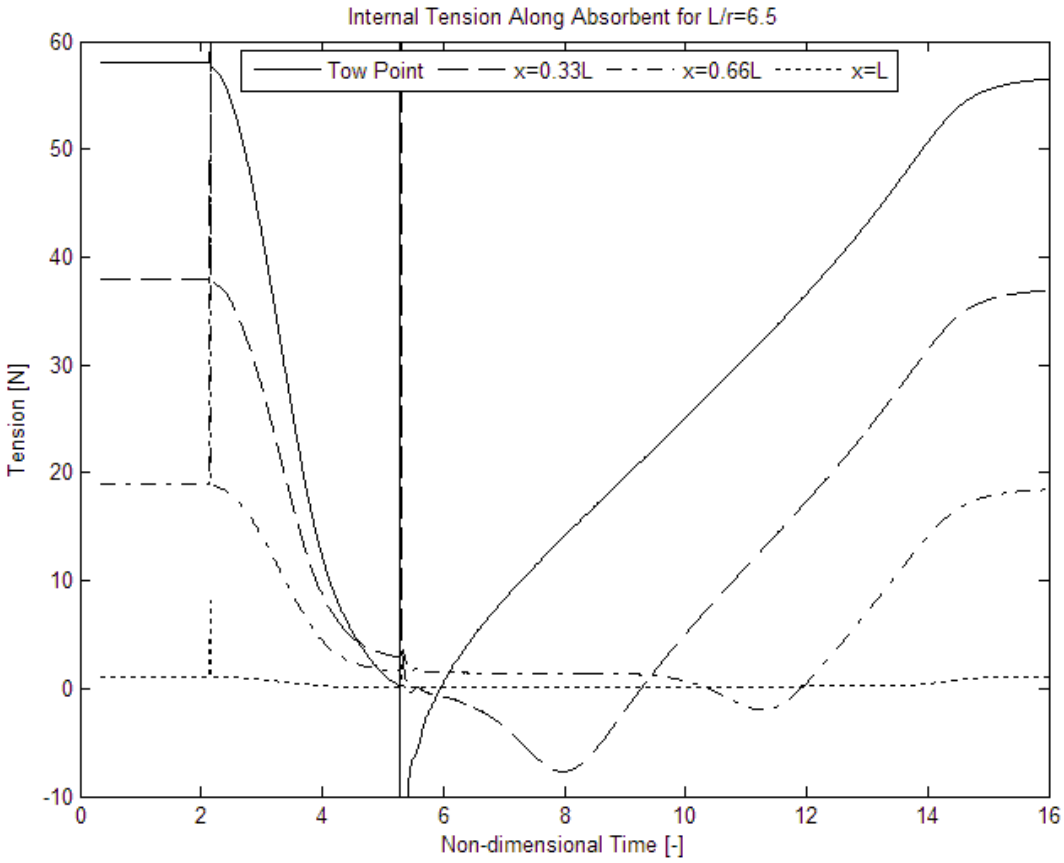

5.7 Internal tension for L/r=6.5

For L/r=6.5, the dip in tension has become more pronounced. During the sail away stage, the majority of the absorbent experiences compression. Based on these observations, the present model is applicable for cable geometries with L/r <4.

Sensitivity to Gain

A proportional gain controller was implemented to enforce a constant speed during the maneuver. A sensitivity study was conducted test the influence of controller gain on simulation results. From these results, a gain value of 1000 is chosen.

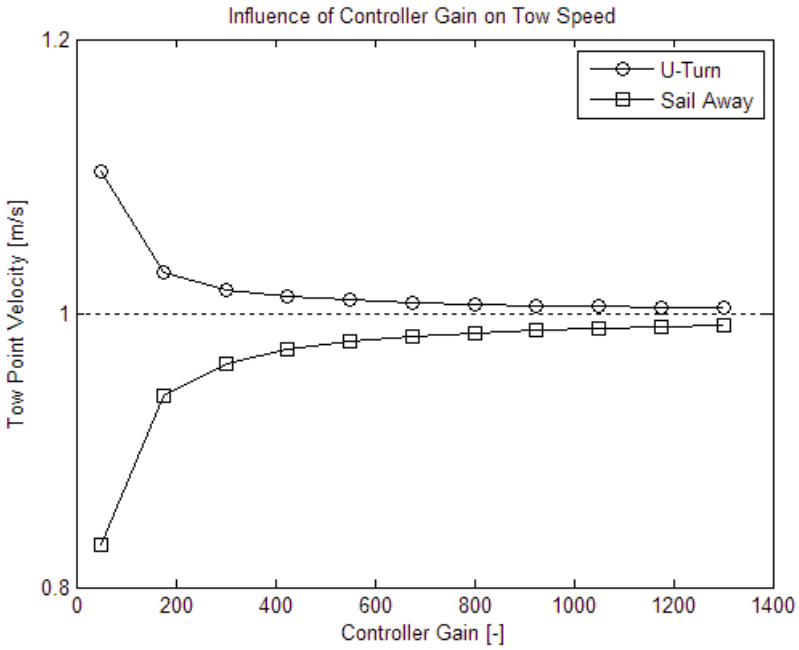

5.8 Tow speed for varying gain value

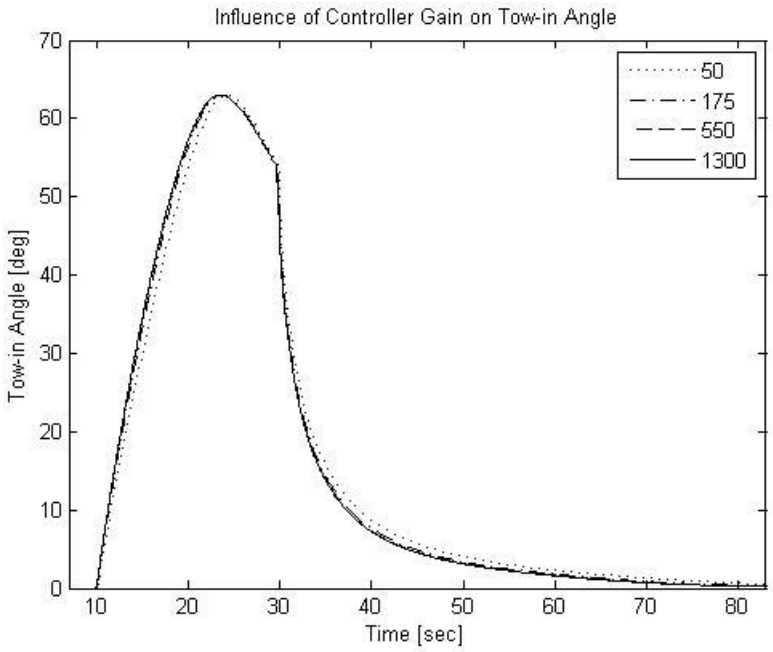

5.9 Tow-in for varying gain value

Figure 5.8 shows the variation of tow speed from the target value, 1 m/s. Figure 5.9 shows that the behavior of the tow in angle is not influenced by controller gain.

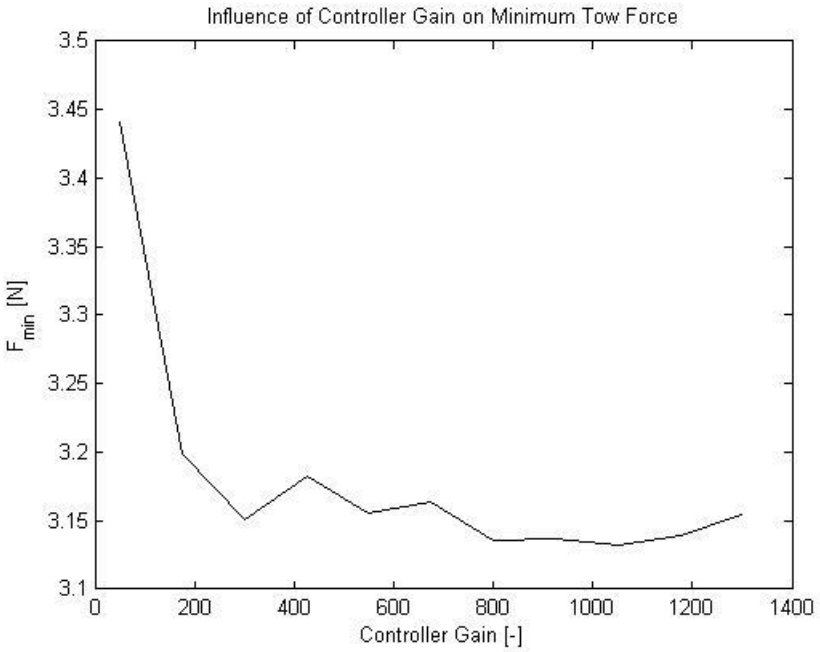

5.10 Minimum tow force for varying gain value

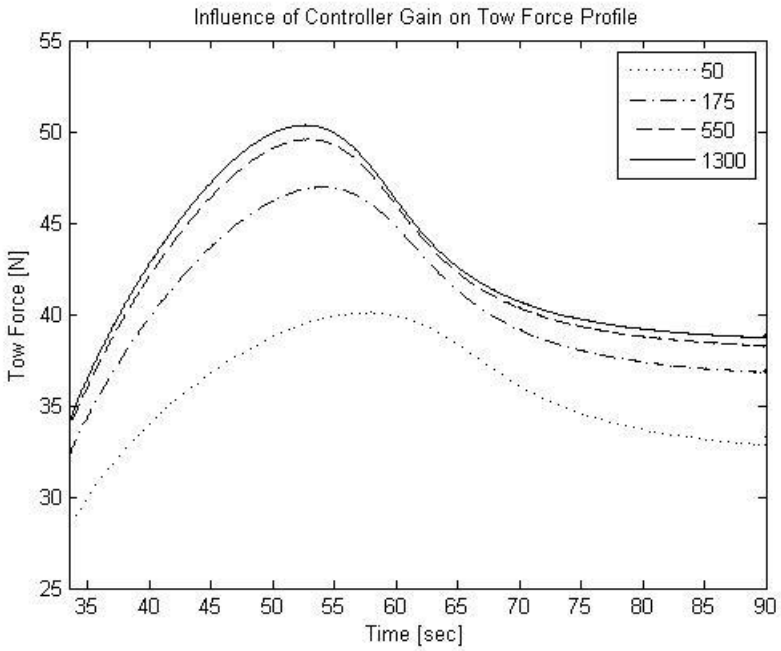

5.11 Tow force profile for varying gain value

The minimum tow force during the U-turn is shown in figure 5.10, and the peak value of the tow force profile during sail away given in figure 5.11. This effect will be discussed further in the next chapter.

Numerical Properties

A brief inspection of the equations of motion indicates that determining the form of the eigenvalues of the matrix $\mathbb{M}^{-1}(\mathbb{P}^S\mathbb{F}^{\parallel} + \mathbb{P}^C\mathbb{F}^{\perp})$ is impractical. Despite having linearized the problem in the general speed, ω, the elements of each of the contributions to this matrix involve nonlinear trigonometric functions of the configuration variable θ. Though an analytic stability criterion was not obtained, a grid sensitivity study was performed and a threshold of stability was identified at n_{arc}=25. The grid size is defined as the number of absorbent elements per semi-circle.

The tow-in angle is averaged after two full turns, during the last quarter-rotation. The standard deviation is also presented. Shown below, the tow-in angle behaves the same after scaling the radius. Also, the system response for tow-in angle remains the same if the system geometry is scaled proportionally.

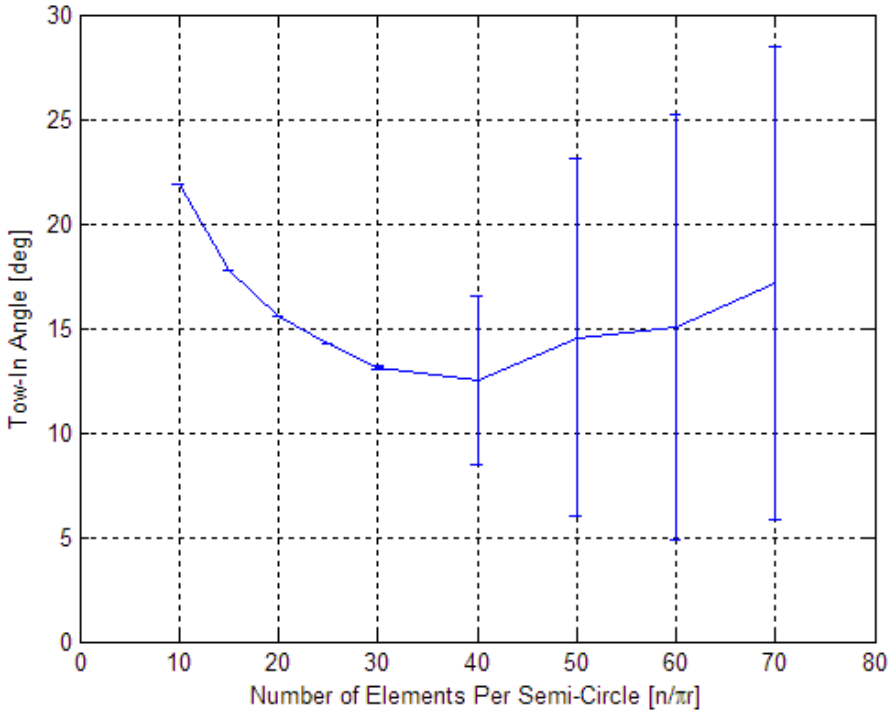

5.12 Development of numerical instability for increasing subdivision

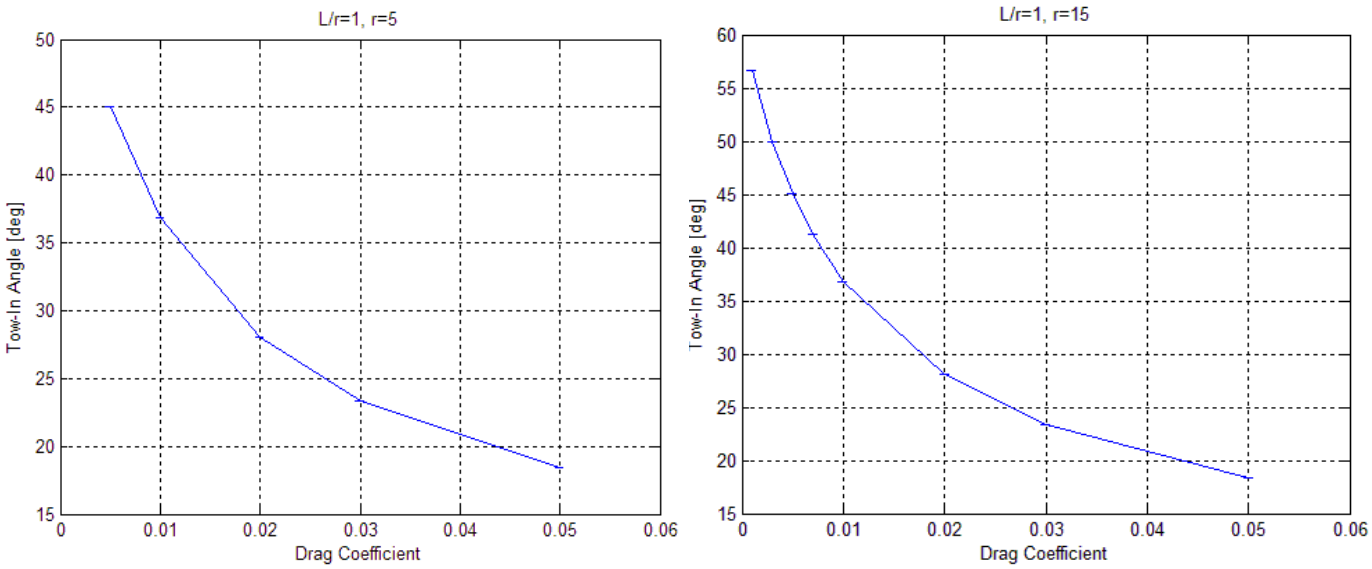

5.13 Model response for scaled geometry

Model Tuning

Again, the tow-in value is averaged after two full turns, over the final 90 degrees, where the system is presumed to have found a steady configuration. As L/r increases, the cable is likely to 'bunch up' in the center of the turn. The test is stopped when the spiral length, $\frac{r}{\sin\alpha}$ defined above, is reached. The system response for the experimentally derived value of the fluid drag coefficients is given in figures 5.14 and 5.15 below. The refined tow in dataset is shown for reference. In the following graphs the arrow indicates increasing parameter $C_D^{\perp}$ and $C_D^{\parallel}$.

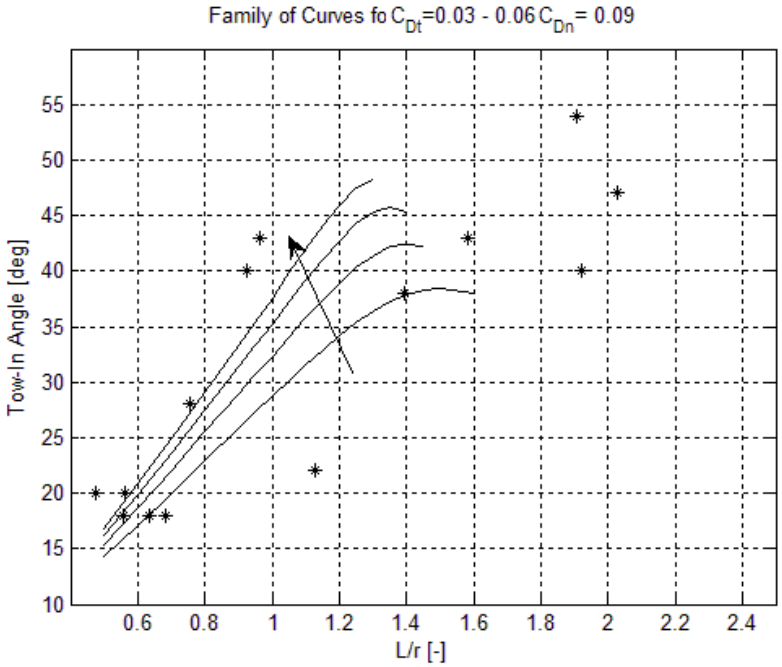

5.14 System response for the experimentally determined normal drag coefficient

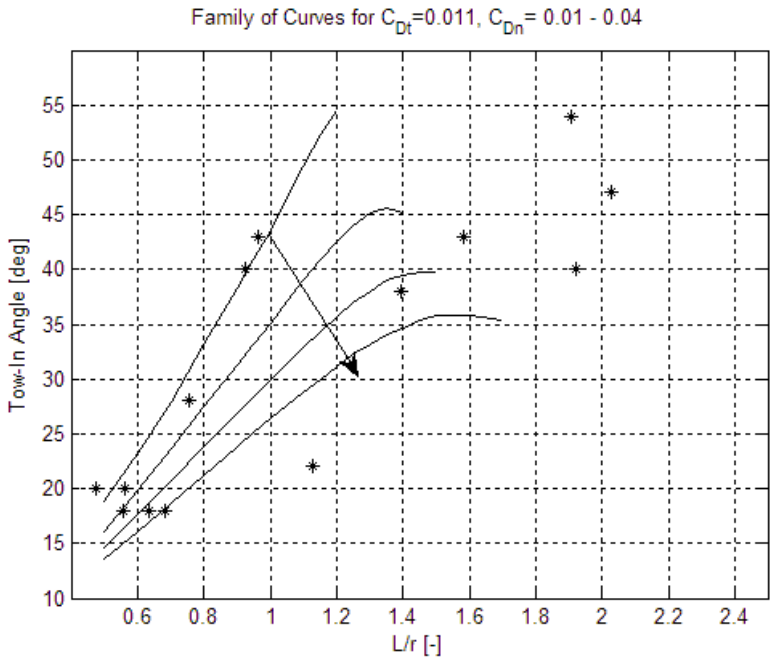

5.15 System response for the experimentally determined tangential drag coefficient

It is apparent from these figures that the values of $C_D^{\perp}$ and $C_D^{\parallel}$ as predicted from the experiment are not congruent. To define clear objectives for model tuning, the data spread of points for tow in angle is reduced to two values: (L/r=0.6, tow-in=20°) and (L/r=1, tow-in=40°).

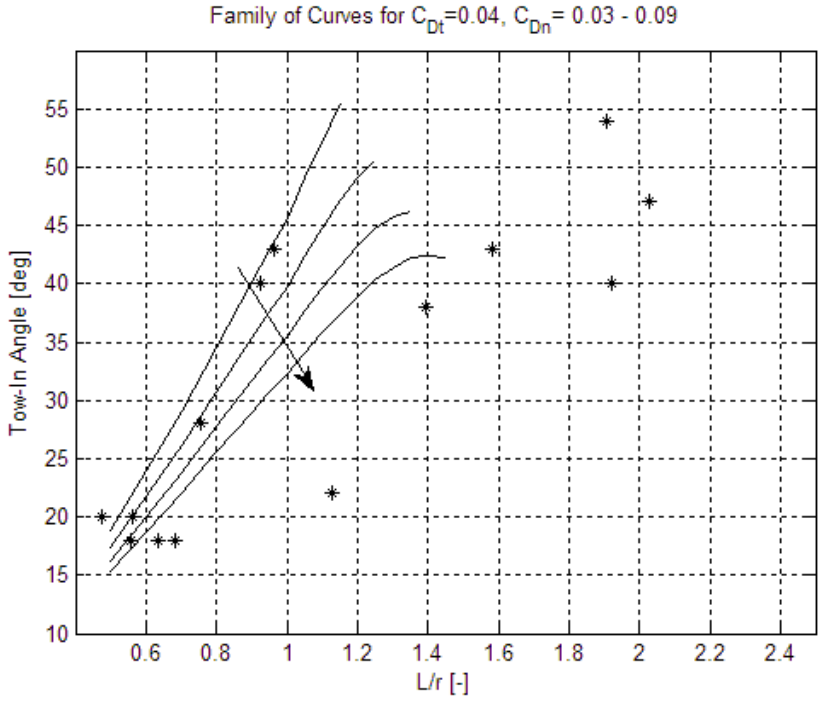

5.16 System response for intermediate value

In figure 5.16 above a compromise is reached with $C_D^{\perp} = 0.05$ and $C_D^{\parallel} = 0.04$.

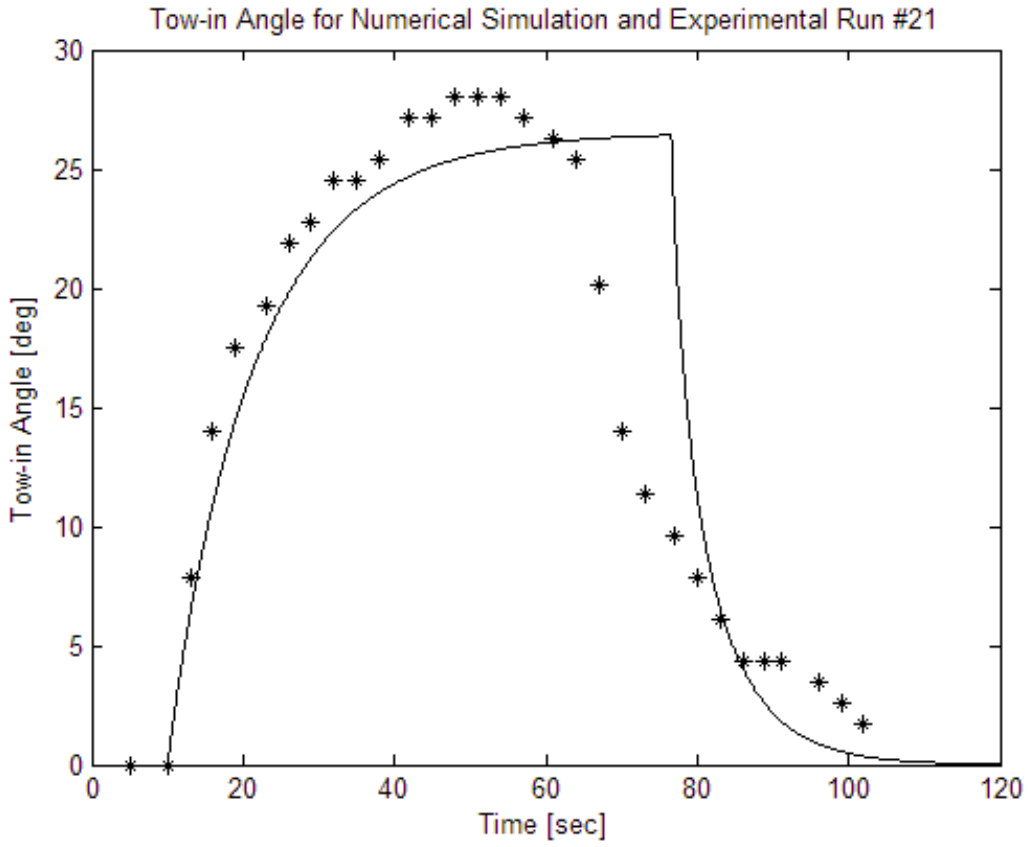

5.17 Simulation result compared with experimental data

A simulation for one of the experimental runs was performed. To achieve the correct towing force, the tangential drag coefficient was increased to $C_D^{\parallel} = 0.065$. As shown in figure 5.14, the corresponding normal drag coefficient is the experimentally derived value, $C_D^{\perp} = 0.09$. Simulation results and the data from the experiment for tow-in angle are given above and show good agreement.

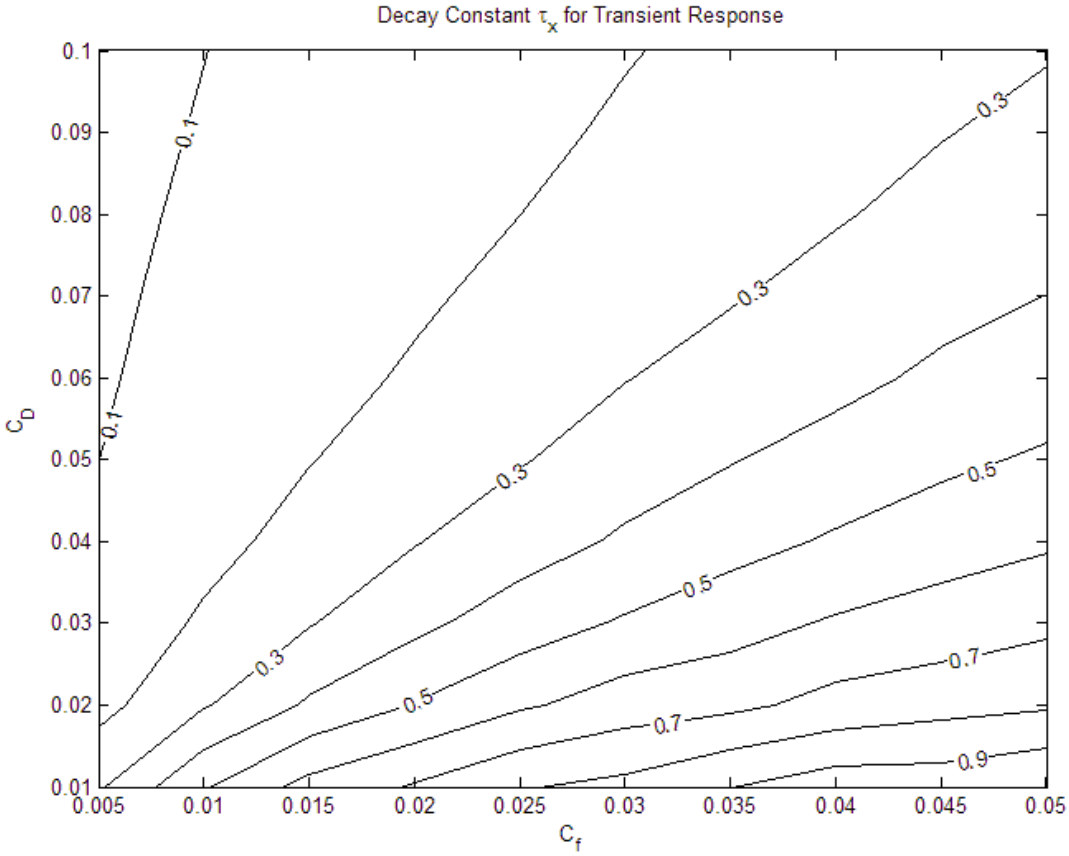

5.18 Transient response for tow-in angle

Finally, the variation in decay constant is presented in figure 5.18 across a range of $C_D^{\perp}$ and $C_D^{\parallel}$. This value is derived from two data samples and only for L/r~2.4. Interestingly, the isocurve for τ=0.4 is congruent with the system response for tow-in angle given above.

Verification Overview

In this chapter, the physical significance of each term in the equations of motion has been clarified. A post processing calculation to check the assumption for tension is derived. A geometric limitation of this simulation technique is found at L/r ~ 4. Also, the influence of controller gain on the simulation results is shown. The numerical properties were investigated and a stability threshold is identified. Finally, the model response is tuned using the experimental results as a guide. Experimentally derived coefficients provided an initial estimate but some compromise was needed to reproduce kinematic and dynamic behavior. Chosen values are $C_D^{\perp} = 0.09$ and $C_D^{\parallel} = 0.065$

6

Simulation Results

Selected results are presented. The time evolution of system variables given, as well as variations in system response for the parameter L/r. Characteristics of absorbent motion through a turn will be discussed.

These simulation results are for a constant towing speed equal to 1 m/s to mitigate the effects of the linearization made for the fluid drag terms. Some numerical errors in the implementation of the controller for the tow force during the two-stage simulation remain. Nevertheless, the system is modeled for varying geometries and the results give a good view of system behavior.

The numerical model was implemented as a multiple stage simulation. Designing a force profile, either via controller as above, or when using an assumed profile as in the next chapter was difficult. Present results do not match satisfactorily at the intersection of the stages. The response of the system is characterized by the tow in angle and the tow force.

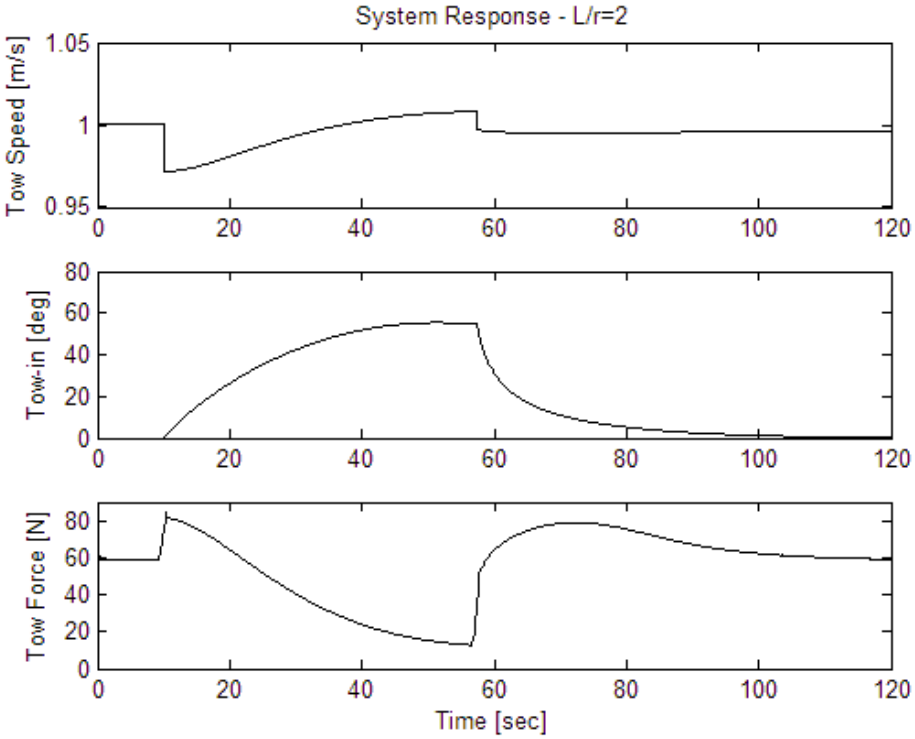

6.1 Simulation output with controlled tow speed

A simulation run, as shown above, is divided into three parts, the approach, the U-turn, and the sail away. In this chapter, the tow speed is held constant at 1 m/s using a proportional gain controller. Some discontinuities are evident in the system response displayed in figure 6.1 above. Although the modeled response is discontinuous at the interface between the stages, the author believes this is an error in the multi-stage implementation. The behavior during particular stages is well represented.

The general coordinates and their derivatives are the raw output of the simulation. To begin, the evolution of the turn is displayed for L/r=2 (left) and L/r=5 (right). The frame rate is adjusted to display the full maneuver for both geometries. Though not quantitative, these images will give the reader a glimpse of the physical process.

6.2 (following page)Kinematic results for L/r=2 (left) and L/r=5 (right

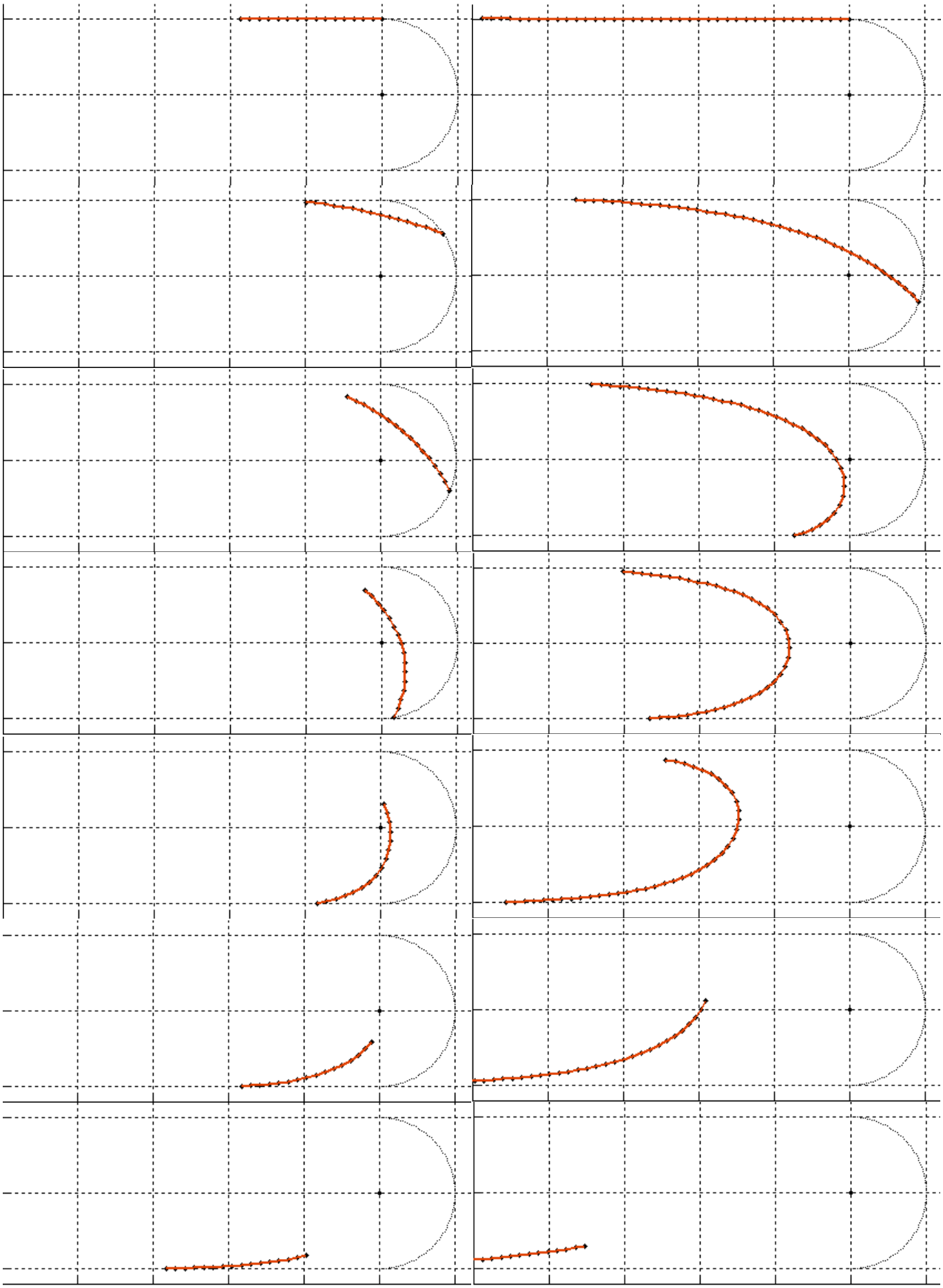

Results for varying L/r ratio are presented on the following pages and briefly discussed. These figures are shown with a non-dimensionalized time for the x-axis. This was introduced so that results for varying turn geometries could be compared. The time scale is the turn radius divided by the tow speed:

$$T^* = \frac{TU}{r}$$

Using this scaling, the duration of the U-turn stage is π.

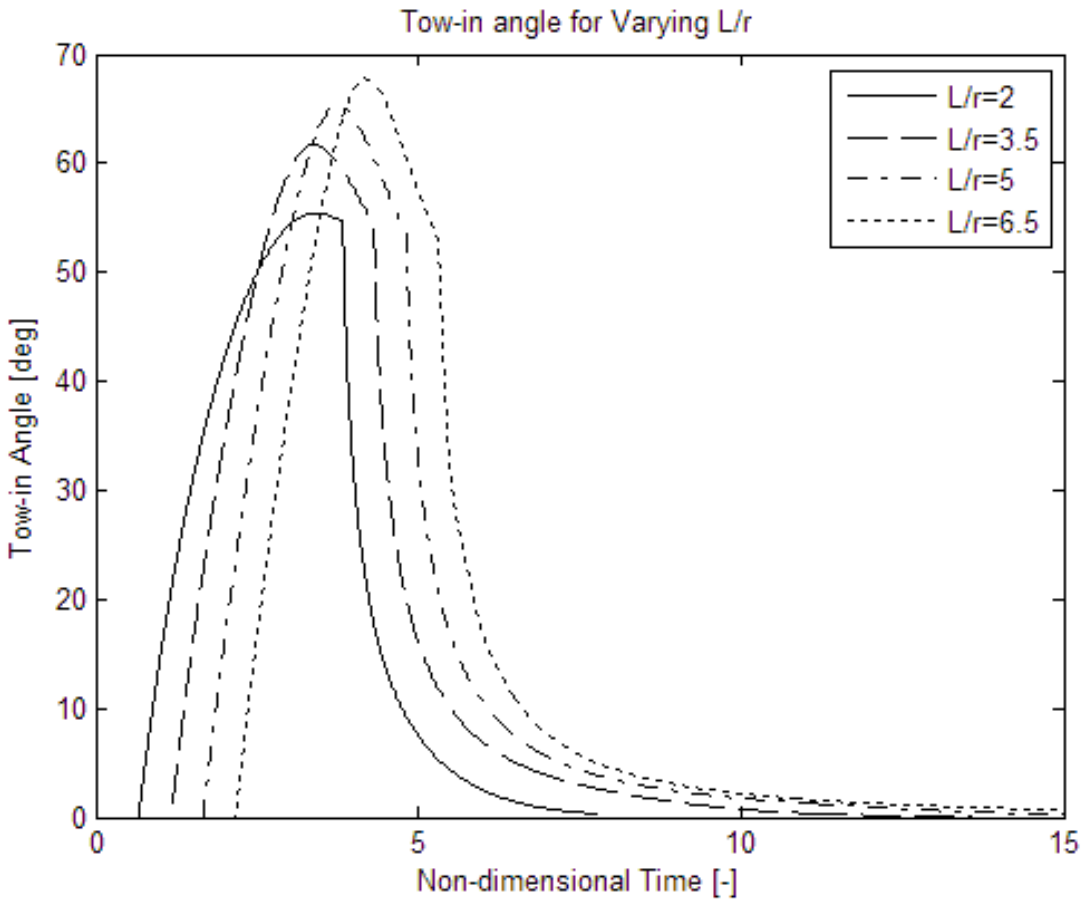

6.3 Response of tow-in for varying L/r

The maximum tow-in angle increases for increasing L/r. During the sail-away stage, decay constant is uniform across values of L/r. The maximum value of the tow-in angle occurs near the apex of the turn for larger values of L/r. After the results of the verification for compression, results for L/r > 4 must be interpreted with caution.

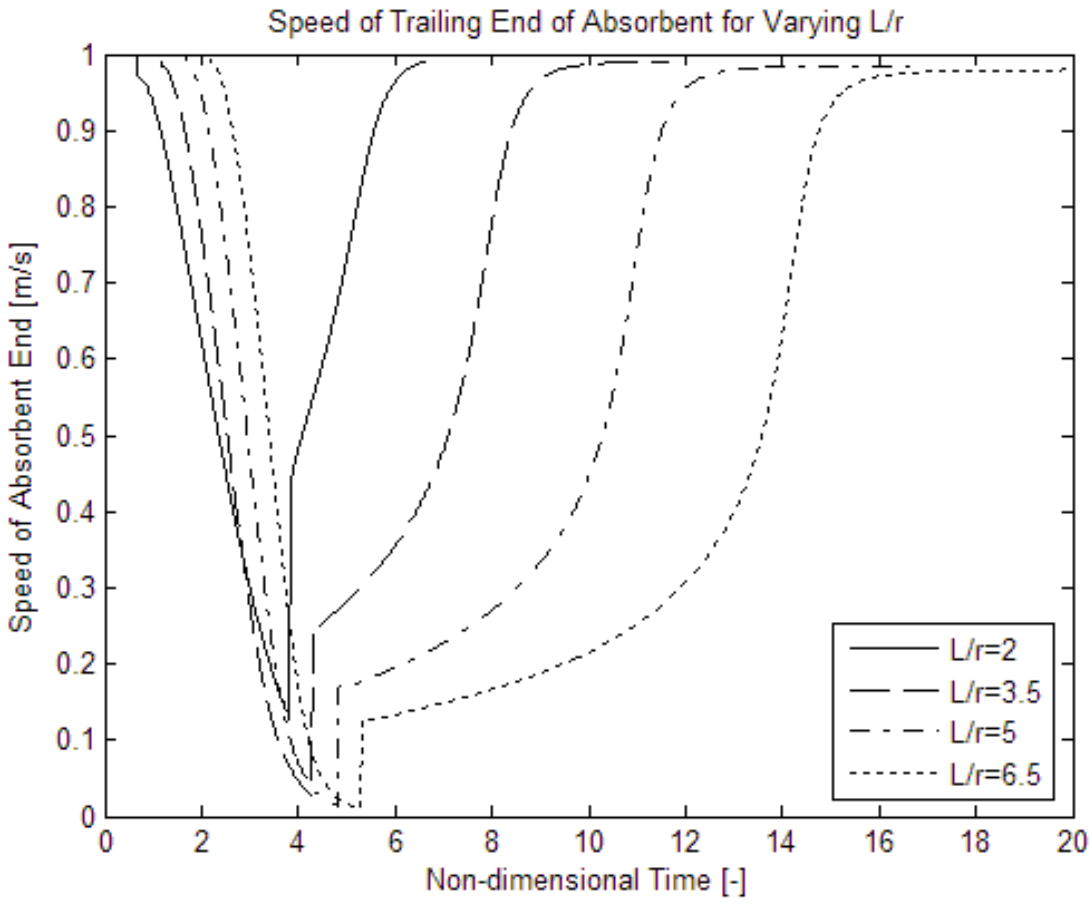

6.4 Response of trailing end speed for varying L/r

Figure 6.3 shows the speed of the trailing end during the maneuver. Overlooking the numerical issues, some observations can be made. For large values of L/r, the trailing end of the absorbent comes to a standstill. During the sail away stage, the trailing and is eventually reaccelerated to the nominal speed. For L/r=5, the trailing end only returns to the nominal tow speed after $T^* \sim 2\pi$, which is twice the time necessary to make the U-turn.

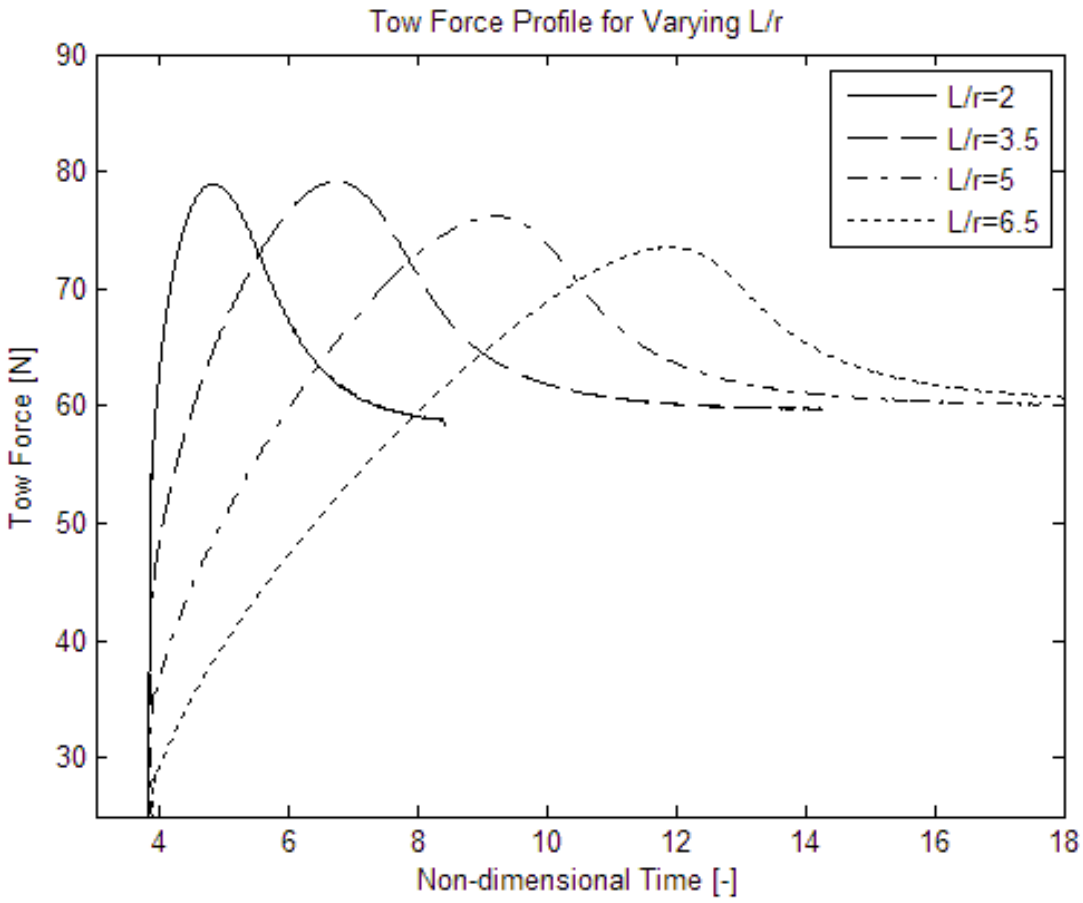

6.5 Tow force profile for varying L/r

The tow force profile for the sail away stage, shown in figure 6.4 above, contains a peak value that is a approximately 1.3 times greater than the straight tow force. The tow force is aligned with the tow point velocity, so one contribution to this peak is the influence of the tow-in angle, which will reduce the tow force according to its projection onto the absorbent direction. Also, the turning absorbent forms a catenary during this stage. The normal fluid force provides the radial component necessary to turn the absorbent with a given internal tension. The relationship between this distributed load, the cable tension, and the geometry of the catenary has the characteristics of a nonlinear spring, where the stiffness increases with increasing radius. The figures in this section were generated using a constant segment length and by decreasing the radius, and the force peak appears to diminish as the radius decreases. Finally, this peak may be a product of the numerical implementation, as the controller attempts to maintain a constant tow speed during the maneuver (see figure 6.1).

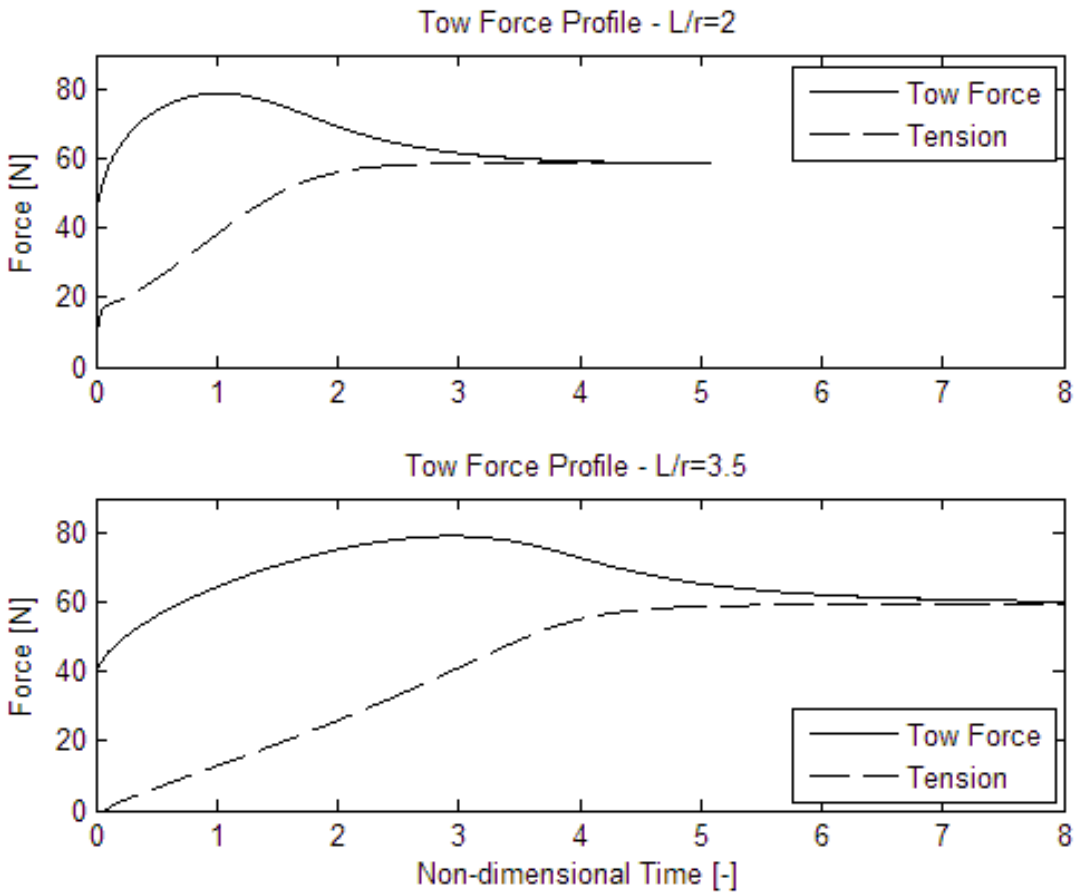

6.6 Discrepancy between tow force and cable tension

Results from the open water experiments also contain peak in the measured force (see figure 4.4), suggesting that this phenomenon is physical. Experimental results are for cable tension, rather than tow force as defined above, implying that the peak in the measured force is due to the catenary effect. Simulation results for tension are presented in figure 6.5 alongside the tow force. Apparently, this effect is not detected in the calculation for internal tension.

Simulation Results Overview

A survey of simulation results is given. The basic characteristics of the absorbent system are discussed. Some non-physical effects are identified. The calculation of internal tension may omit a catenary stiffness component.

7

Protei Feasibility Study

The Protei group developed a deformable hull with a long keel that consciously emulates the flexible forms found in the natural world with the hope of achieving the same efficiency. The feasibility of this concept was the topic of this thesis at the outset, and research findings are briefly presented here.

Though flow mechanisms for highly efficient interaction with water exist, the mechanical realization is not presently realistic. A brief design exercise was carried out to develop a placeholder vessel, with maximum driving force and maneuvering capabilities to cope with the absorbent tail. It will be used to arrive at a hypothetical sail-driving force for testing the feasibility of the Protei oil spill remediation concept.

Finally, the numerical simulation is run using the towing force profile for the placeholder vessel to determine the maximum length of oil absorbent.

Protei Development and Bio-mimicry

The Protei vessel evolved from a store-bought remote controlled sailboat. During early tests, it was observed that towing oil absorbent greatly hinders maneuvering. When the absorbent is attached to the after section of the boat, the absorbent will serve to oppose any attempt to change course. Mr. Cesar Harada, founder of the Protei project, moved the rudder to the bow in an attempt to improve the maneuvering of the vessel. Further testing and subsequent prototypes have established the feasibility of this configuration. A conventional rudder located at the stern is unable to affect the course of the vessel because it is overwhelmed by the towing load of the oil absorbent. The course instability inherent to the bow-rudder configuration is damped by the towing load of the oil absorbent.

7.1 Protei prototypes

A deformable hull with a long keel was developed over the course of extensive prototyping. The proposed mechanism consciously emulates the flexible forms found in the natural world with the hope of achieving the same maneuvering efficiency.

Following the methodology of bio-mimicry, inspiration is sought in the flow mechanisms used by fish. A cursory review of academic literature has revealed a broad array of research in the field of fish-like propulsion and maneuvering. [4] [5] [6] [7] Diverse flow-control mechanisms are studied using a variety of techniques, including robotic fish models. [8] [9] [10] [11] [12] There are also many investigators studying live specimens, where extra effort is sometimes needed to produce repeatable results. [13] [14] [15] [16] [17] Finally, a heaving and pitching hydrofoil is the focus of research as a canonical problem in fish-like propulsion. [18] [19] [20] The principal interest among these researchers is understanding how fish achieve such easy agility and superior efficiency in water.

Broadly speaking, efficiency means minimizing the energy in the wake and avoiding flow separation and the associated adverse pressure gradients. [9] Separation and turbulence control is a key feature of fish locomotive efficiency.

"Perhaps fish tune their swimming movements to take advantage of the lowered shear stress of a nearly separating boundary layer, while simultaneously benefiting from the reduced form drag and increased lift of fully attached flow." [8]

Fish are intimately aware of their environment and are able to respond subtly to influence flow behavior. Several researchers have identified travelling waves along the fish body that serve to stabilize nearly separating flow by introducing favorable pressure gradients. [12] [9] Also, it is observed that fish actively manipulate vorticity in propulsion and maneuvering in what are termed 'thrust augmentation devises' such as delayed stall.

The academic and scientific work in this field offers a compelling glimpse of what highly efficient vessels might one day incorporate. However, the physical problem is very complicated not yet fully understood. Also, any hypothetical benefits hinge on an acute sensitivity to flow behavior along the hull and smooth, intricate deformation of control surfaces. The mechanical realization of this concept is nothing short of futuristic.

Protei Placeholder Vessel

Recognizing that the deforming hull concept remains in early prototype stage, a brief design exercise was carried out to develop a representative Protei vessel. It will be used to arrive at a hypothetical sail-driving force for input to the numerical model. The Protei vessel should be thought of as a sailing tugboat. This poses a challenging design brief. The following observations are made.

Sailing upwind and tacking is probably not feasible. A tacking vessel is carried through the wind by its inertia and the added drag of the oil absorbent will quickly stop the vessel as soon as it turns into the wind and the sails loose power. It is much more realistic to design a system around jibing, where the vessel is able to maintain propulsive power through the maneuver. The oil absorbent will heavily influence the yaw balance of the Protei vessel. The absorbent will account for a significant portion of the total inertia and (ideally) the majority of resistance. Such a towing load may heighten course-stability dramatically. This is beneficial until the vessel is asked to perform a maneuver.

The vessel is less than seven meters and travelling slowly, giving a low Reynolds number and thus a large frictional resistance component. This, in combination with the towing load of the absorbent, will require maximum righting moment in order to support the necessary sail area. The wind gradient near (<10 m) the water surface means the wind is not reliable for pulling oil absorbent. However, with a low target speed (1 m/s), the variation of angle of attack will be minimal.

The following design criteria are established based on the specifications of the Protei system and the difficulties outlined above.

1. Oil Cleaning

Is the proposed design effective in cleaning oil? Can it sail beam-wind? How much absorbent can it tow? Can the proposed design accelerate the oil absorbent and maintain a steady speed of 1 m/s?

2. Maneuvering

Is the proposed design able to cope with the towing load while performing necessary maneuvers?

3. Operations

How complex is the design/control for autonomous operations? Is it possible to lift the vessel onto the support ship?

To achieve maximum driving force, a multi-hull design with water ballast is proposed powered by a sail modeled after a reaching gennaker. The sail is carried on a rolling forestay and an A-frame mast that is stepped in the keel of the main hull. The main hull has efficient shape with large lateral surface area, while the ama hull provides righting moment via water ballast.

This estimate is made for idealized conditions, with 10 knots of wind and flat water. The hypothetical driving force of a reaching gennaker is found using aerodynamic coefficients of a Volvo 60 reaching sail, Cl =.9 and Cd =.6. This sail was chosen because it is optimized for the same range of wind angles and because it has been carefully studied in a wind tunnel. The forward and lateral sail forces is calculated using:

$$L = \frac{1}{2}\rho A V^2 C_L \cos\alpha$$

$$D = \frac{1}{2}\rho A V^2 (C_D + C_{Di}) \sin\alpha$$

C_{Di} is the induced drag produced by the foil by the generation of lift. In the momentum theory of lift, it is the force spent redirecting the incident stream of air. It is a function of the aspect ratio and the lift coefficient, and reflects the efficiency of the foil. It is defined as:

$$C_{Di} = \frac{{C_L}^2}{\pi AR}$$

Table 7.1 Sail plan geometry and force generated

Span	9	m	A	20	deg
Chord	5	m	α_i	9,1	deg
AR	1,8	[]	α_{eff}	11	deg
Lift	303	N			
Drag	202	N			
Dragi	17,6	N			

The Protei is designed to sail beam-wind, meaning that the lift vector is aligned with the direction of travel while the sum of the drag forces will constitute the side force. Finally, the center of effort for the triangular sail is assumed to be at one third of the mast height, generating a heeling moment in the longitudinal and transverse directions. The possibility of nose-diving is a risk inherent of multihulls, which derive their stability from geometry rather than displacement. The main hull is given moderate displacement by the long keel. Increasing the inertia will help to cope with the threat of nose-diving in wind gusts, and will help

balance the inertia of the ama about the jaw axis. The heeling moment in the transverse direction is supported by the ama hull, which contains seawater ballast tanks. These are manually filled by the operator based on expected weather conditions. The ama dimensions are roughly estimated based on a cylindrical form.

Table 7.2 Calculation of ama proportions

Z-Center of effort		3,6	M
Transverse		1091	Nm
Longitudinal		791	Nm
Ama Distance		4,0	m
Ama Weight		273	kg
Ballast Volume		266	liter
Cylinder dia.	0,3	3,8	m

The side force must be supported by the keel. The keel is dimensioned by following the same method as outlined above. The keel will adopt some angle of attack, the leeway, with relation to the water to produce the needed side force. Just as above, the production of lift generates an added, induced drag component:

$$F_{Di} = \frac{{F_{lat}}^2}{\pi AR \frac{1}{2} \rho V^2 A}$$

Besides this drag, there are also drag components associated with skin friction and form drag. These are approximated using the ITTC procedure and a form factor of k=0,6 for long keels.

Table 7.3 Calculation of Protei drag

			Boat		
Draft	2	m	Speed	1	m/s
Chord	4	m	Re#	3,77E+06	
AR	0,5		C_f	3,58E-03	
A_keel	16	m2	K+1	1,6	
A_ama	7	m2			
Wetted area:	23	m2	Rf	67,53	N
			Ri	7,49	N

These rough estimates indicate that 200N are available for towing a length of oil absorbent. The keel will not perform effectively if the vessel is not near its target speed. The absorbent length and the quantity of ballast water can be configured while deploying based on conditions.

To overcome the maneuvering challenge, a bow-stern symmetry similar to a proa is proposed. When the Protei vessel reaches the edge of the oil slick and needs to turn around, the sail is rolled away. Protei will come to rest and drift downwind slowly. The absorbent is secured at the midship and passes under the ama hull, which has bows swept up to make sure this happens. The sail is unrolled in the opposite orientation, causing the Protei vessel to accelerate on the new course. The vessel makes considerable leeway while accelerating, which ensures that it will not become entangled in the absorbent.

Aside from this maneuver, the vessel is only asked to sail long, beam-wind courses. Capitalizing on the course stability brought by the towing load, if the oil absorbent tow point is correctly located along the crossbeam, the Protei can sail without rudders. With some fine-tuning, one should be able to align the driving force of the sails with the towing load of the oil absorbent. It may be that the towing force is located ahead of the center-of-effort for the sail, resulting in yaw instability. The gennaker tack attachment may be rigged to switch from jibe to jibe, such that the resultant sail force is positioned ahead of the towing force.

7.2 Protei placeholder vessel

During the shunting maneuver, the sail is rolled away and the vessel slows. The vessel is nearly still and drifting downwind, propelled by the windage of the A-frame mast and the furled sail. After drifting sufficiently to preclude entanglement, the sail is unfurled in the new orientation.

Cosine functions are used to construct a continuous tow force profile for numerical simulation. The tow force is estimated to be 200N. The force due to windage is estimated to be 30N.

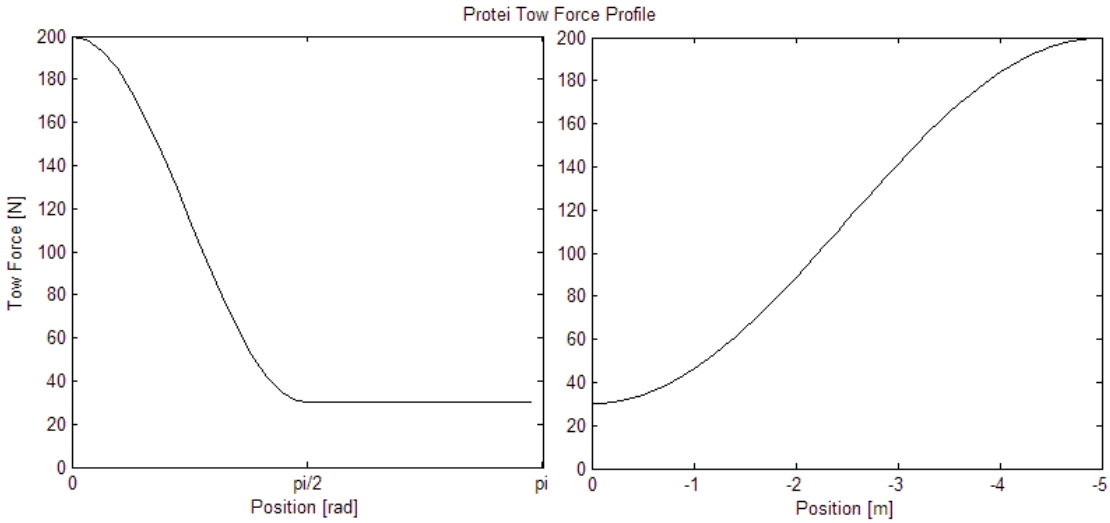

7.3 Placeholder tow force profile

Numerical Simulation

The feasibility of the turn for the Protei vessel is studied using the numerical simulation. The tow force profile described in figure 7.3 above is applied at the tow point, and the resulting speed is found. Nonphysical discontinuities between the simulation stages were encountered again. For the given tow force profile, the tow speed will reach its minimum value during the U-turn stage. It is assumed that the successful completion of the U-turn stage indicates that the maneuver is feasible.

A meaningful simulation result hinges on the proper selection of hydrodynamic coefficients. As detailed in chapter 4, the tangential drag coefficient is a related to the surface roughness. The present experiment was performed with braided polypropylene line, with a much larger roughness scale compared with the oil absorbent. The B.E.P. experiment measured the resistance of the oil absorbent material, and their result, $C_D^{\parallel} = 0.01$, is used. The normal drag coefficient is proposed as a function of absorbent draft,
$C_D^{\perp} = 0.9752 * \mathrm{T} + 0.0047.$

This linear variation is an approximation of the exponential profile introduced in chapter 4 for $0 < \mathrm{T} < 0.2$. The oil absorbent diameter is 20 cm, approximately twice that of the polypropylene test segment. Although the scientific foundation of the proposed exponential profile is scant—it is essentially based on one data point and an assumption—the theoretical justification for a $C_D^{\perp}$ that varies with draft is sound. The effect of doubling the draft is more than to double the frontal area; the absorbent will gain better traction as it reaches deeper into the water.

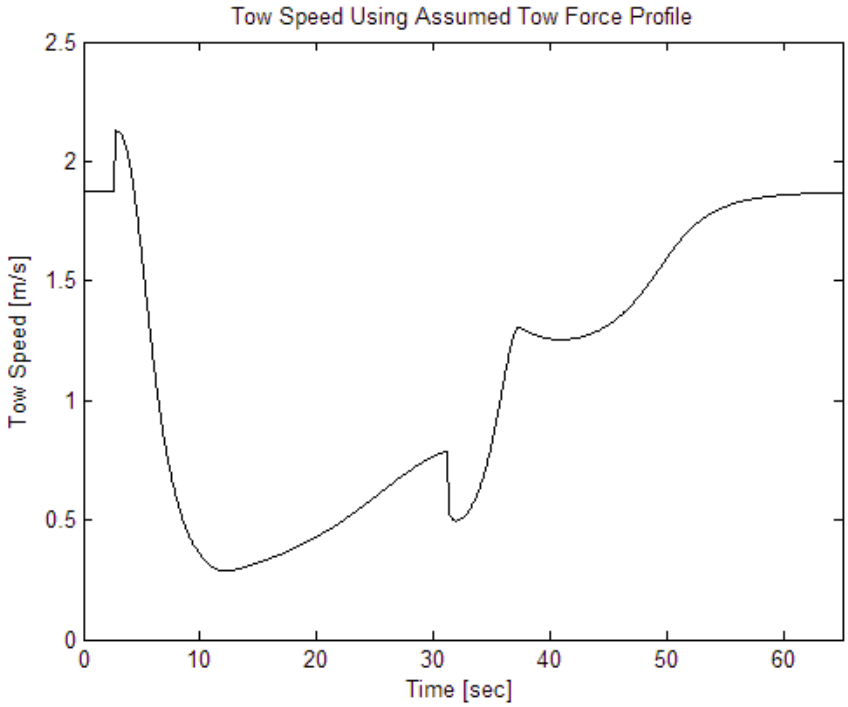

7.4 Simulation output for tow force profile

During operation, the oil absorbent mass increases as it fills with oil. The effect of this variation on hydrostatics is to increase the draft and the wetted area. The increase in absorbent mass will also manifest itself as the momentum of the oil-laden absorbent needs to be redirected in the u-turn. The consequences of this effect are examined with the tow force profile of figure 7.3 and an absorbent length L=20.

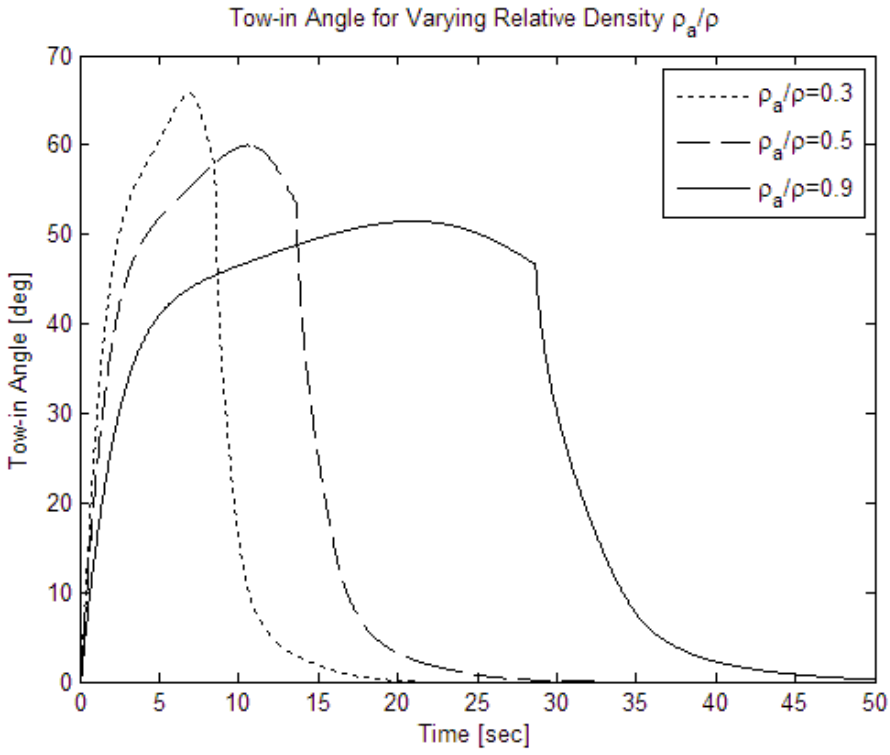

7.5 Influence of oil content on tow-in angle

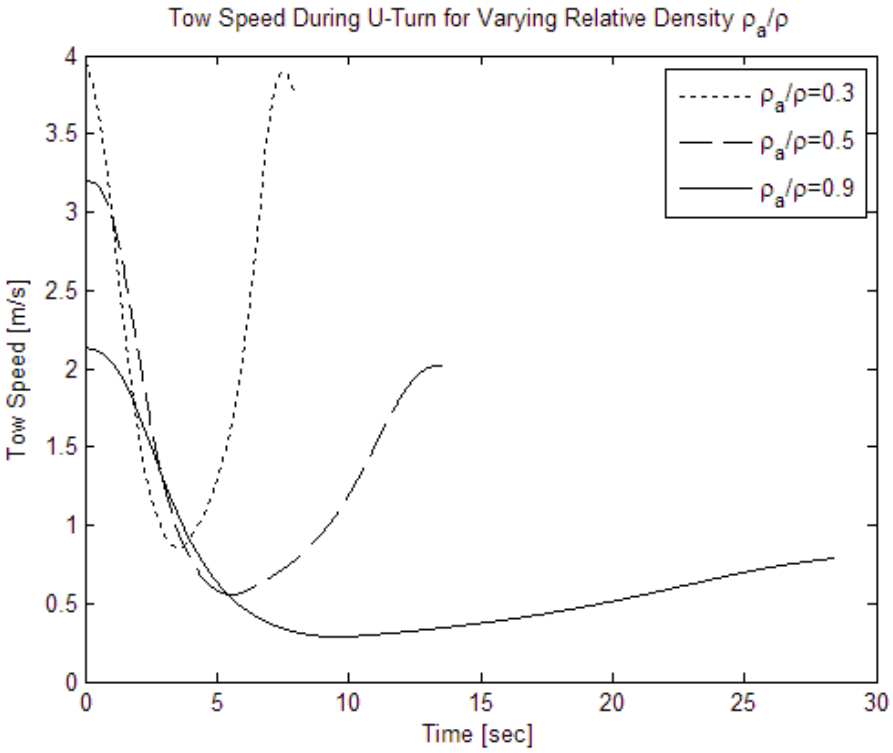

7.6 Influence of oil content on tow speed

As the absorbent fills with oil, the absorbent sinks to a deeper draft. The normal drag coefficient increases according to the linear function proposed in chapter 4, resulting in a lower tow-in angle. This is a beneficial effect as the Protei towing force will be better aligned with the oil absorbent. However, the net effect of the heavier absorbent is obviously to slow the tow speed. This effect is seen in figure 7.6. One should note that the tow speed coming into the turn will not be as high as 4 m/s. The rough estimate made for the tow force calculates the ship's resistance based on a speed of 1 m/s. The straight sailing equilibrium will come to some intermediate velocity value. A thorough modeling should include a velocity prediction function for the vessel.

The absorbent length is increased to L=35. In order to prevent compression in the cable, the L/r ratio is kept below 4, giving a turn radius of 9 meters. This may be realistic since the Protei vessel is first drifting due to windage, and then accelerating with a large leeway angle.

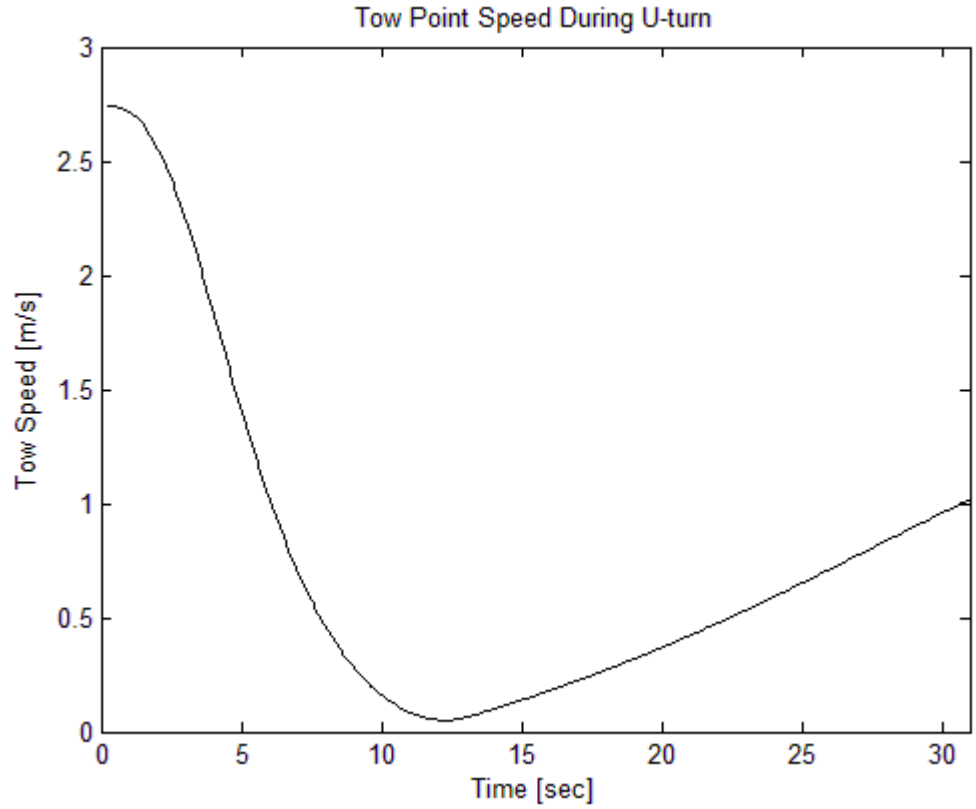

7.6 Tow point speed

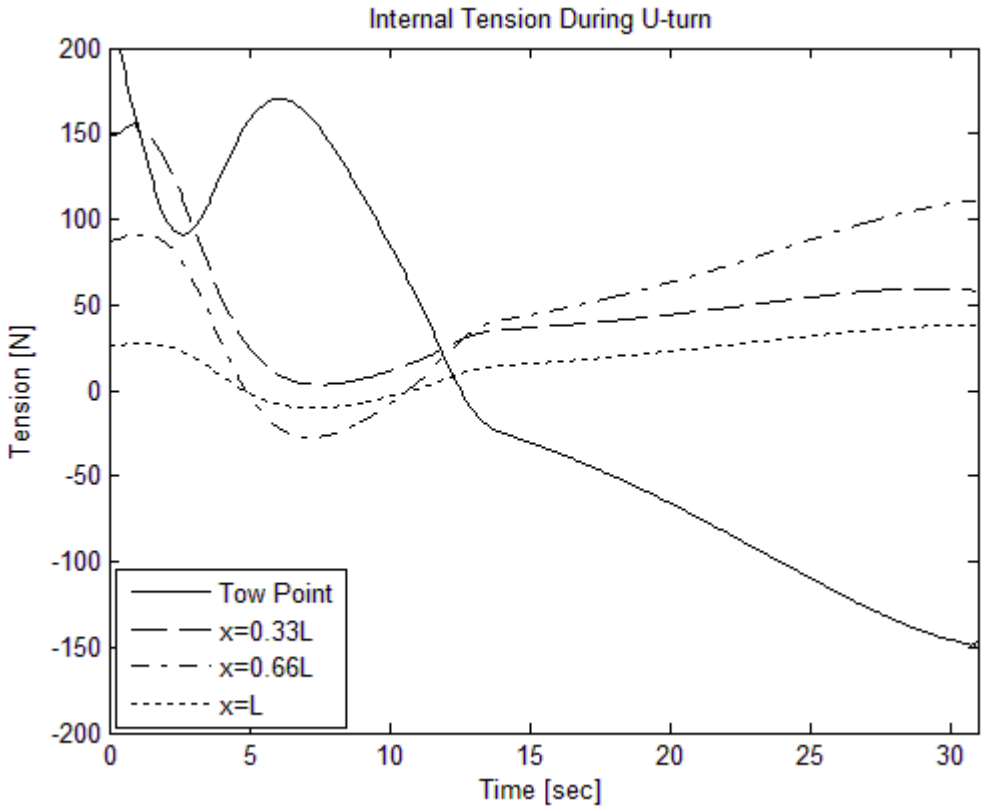

7.7 Internal tension

The results shown in figure 7.6 and 7.7 are for a half-full absorbent with L=35. The minimum value of the velocity profile is less than 0.1. Bearing in mind that the absorbent is only half full, this result indicates that the feasible length for the Protei system is less than 35 meters.

Figure 7.7 displays the internal tension over the course of the maneuver. Although the geometry of this turn obeys the restriction derived in the verification chapter, non-physical, compressive behavior is observed at the tow point. From the figure, it is as though the inertia of the trailing cable is pushing the towing vessel through the turn. Though it is possible to imagine some compressive force being transferred in this way, according to the assumptions upon which this model was based, this should not be. Absent this effect, the limiting length of absorbent would be shorter.

Protei Feasibility Study Overview

A synopsis of research performed for the deformable hull concept is given for the interested reader. The conclusion of this work is that though energy efficient maneuvering mechanisms have been identified, implementing them in a mechanical system is not presently feasible.

A brief design exercise is performed to estimate the towing force that a small sailboat can achieve. Also, the maneuvering challenge is addressed. This placeholder vessel is used as the basis for a feasibility study of the Protei system. The maximum length is estimated near 20 meters.

The simulation returned large compressive forces, indicating that a physical assumption is violated. The inertia of the absorbent is observed pushing the towing vessel through the turn. This is a non-physical effect, an indication that a more complete material model is needed to simulate the flexible absorbent.

Thesis Overview and Recommendations for Further Study

The physical problem of towing a floating, flexible body through a turn was modeled by numerical simulation. The simulation was designed after reviewing the state of the art in the field. Material behavior was not included. The equations of motion were derived using Kane's method for dynamical analysis. The application of Kane's method clarified the accounting of reference frames and of constraints. Besides issues in the clumsy numerical implementation, the model has successfully reproduced the physical system for a restricted set of geometries. The derivation of the numerical model was above all an instructive experience in dynamical analysis.

The tensile force was derived, a non-contributing force in Kane's nomenclature. An experiment was designed and conducted to estimate the value of the hydrodynamic coefficients and to compare the properties of the floating system with existing work on submerged cable behavior. It was shown that a flexible body towed on the surface exhibits a similar behavior to a submerged cable system. A large set of data was obtained for the steady-state experiments and it was possible to derive estimates for the tangential and normal drag coefficients. A depth-varying normal drag coefficient is proposed because the absorbent will gain better traction as it reaches deeper into the water. The numerical model is tuned using these values. Finally, the feasibility of the maneuver for the Protei vessel was assessed. The maximum absorbent length is conservatively estimated to be 20 meters.

In hindsight, the physical model could be the clarified by changing way that the path of the tow point is defined. The use of the variables, $\dot{b}, \dot{\theta}_c$, to 'set-up' the problem leads to cumbersome expressions and the confusing distinction between these 'set-up variables' and the 'real' degrees of freedom. Expressing the path as constraint function would be more elegant, and may allow a seamless numerical implementation. In the present approach, where the maneuver is divided into stages, the matching of these individual models is not satisfactory. The numerical implementation given here is not computationally efficient. An optimization of the solver, together with a new constraint function for the tow path could substantially improve performance.

Disregarding material behavior and modeling the system as a rigid linkage has introduced limitations for the range of applicability of this numerical simulation is limited in. During the Protei feasibility test, any precise conclusion was hampered by the presence compressive forces. If the non-linearity for material behavior is modeled, the simulation will be more widely applicable.

The proposed profile for $C_D^{\perp}$ can be placed on more scientific footing by conducting similar open water experiments with test segments of varying diameter. In the towing tank, the phenomenon can be examined by towing a bluff body that is immersed to a range of drafts. A thorough investigation of the influence of the free surface boundary condition on the normal drag coefficient might also include a computational fluid dynamic component.

Bibliography

[1] D. A. Chapman, "Towed Cable Behaviour During Turning Maneuvres," *Ocean Engineering,* vol. 11, no. 4, pp. 327-361, 1984.

[2] F. White, Viscous Fluid Flows, New York: McGraw-Hill, 2006.

[3] T. Kane, Dynamics, Stanford: Holt, Rinehart, Winston, 1968.

[4] B. Ahlborn, D. G. Harper, R. W. Blake, D. Ahlborn and M. Cam, "Fish without footprints," *Journal of Theoretical Biology,* pp. 148:521-533, 1991.

[5] M. S. Triantafyllou, G. S. Triantafyllou and D. K. P. Yue, "Hydrodynamics of fishlike swimming," *Annu. Rev. Fluid Mechanics,* pp. 32:33-53, 2000.

[6] Q. Zhu, M. J. Wolfgang, D. K. P. Yue and M. S. Triantafyllou, "Three-dimensional flow structures and vorticity control in fish-like swimming," *Journal of Fluid Mechanics,* vol. 468, pp. 468:1-28, 2001.

[7] M. J. Wolfgang, J. M. Anderson, M. A. Grosenbaugh, D. K. P. Yue and M. S. Triantafyllou, "Near-body flow dynamics in swimming fish," *The Journal of Experimental Biology,* pp. 202:2303-2327, 1999.

[8] E. J. Anderson, W. R. McGillis and M. A. Grosenbaugh, "The boundary layer of swimming fish," *The Journal of Experimental Biology,* pp. 204:81-102, 2001.

[9] M. S. Triantafyllou, A. H. Techet, Q. Zhu, D. N. Beal, F. S. Hover and D. K. P. Yue, "Vorticity control in fish-like propulsion and maneuvering," *Integrative and Comparative Biology,* pp. 42:1026-1031, 2002.

[10] P. Freymuth, "Visualizing the connectivity of vortex systems for pitching wings," *Journal of Fluids Engineering,* pp. 111:217-220, 1989.

[11] K. Streitlien, G. S. Triantafyllou and M. S. Triantafyllou, "Efficient foil propulsion through vortex control," *AIAA Journal,* pp. 34:2315-2319, 1996.

[12] A. H. Techet, F. S. Hover and M. S. Triantafyllou, "Seperation and turbulence control in biomimetic flows," *Flow, Turbulence and Combustion,* pp. 71:105-118, 2003.

[13] E. M. Standen and G. V. Lauder, "Dorsal and anal fin function in bluegill sunfish: three-dimensional kinematics during propulsion and maneuvering," *The Journal of Experimental Biology,* pp. 208:2753-2763, 2005.

[14] J. A. Walker, "Kinematics and performance of maneuvering control surfaces in teleost fishes," *IEEE Journal of Oceanic Engineering,* pp. 29:572-584, 2004.

[15] J. C. Nauen and G. V. Lauder, "Locomotion in scombrid fishes: visualization of flow around the caudal peduncle and finlets of the chub mackerel," *The Journal of Experimental Biology,* pp. 204:2251-2263, 2001.

[16] J. C. Nauen and G. V. Lauder, "Quantification of the wake of rainbow trout using three-dimensional stereoscopic particle image velocimetry," *The Journal of Experimental Biology,* pp. 205:3271-3279, 2002.

[17] G. V. Lauder and E. G. Drucker, “Morphology and experimental hydrodynamics of fish fin control surfaces,” *IEEE Journal of Oceanic Engineering,* pp. 29:556-571, 2004.

[18] H. R. Beem, D. E. Rival and M. S. Triantafyllou, “On the stabilization of leading-edge vortices with spanwise flow,” *Experimental Fluids,* pp. 52:511-517, 2012.

[19] K. Ohmi, M. Coutanceau, T. Phuoc Loc and A. Dulieu, “Vortex formation around an oscillating and translating airfoil at large incidences,” *Journal of Fluid Mechanics,* pp. 211:37-60, 1990.

[20] D. A. Read, F. S. Hover and M. S. Triantafyllou, “Forces on oscillating foils for propulsion and maneuvering,” *Journal of Fluids and Structures,* pp. 17:163-183, 2003.

[21] D. Dave and A. Ghaly, “Remediation Technologies for Marine Oil Spills: A Critical Review and Comparative Analysis,” *American Journal of Environmental Sciences,* pp. 423-440, 2011.

[22] C. Ablow and S. Schechter, “Numerical Simulation of Undersea Cable Dynamics,” *Ocean Engineering,* pp. 443-457, 1983.

[23] B. Buckham, M. Nahon, M. Seto, X. Zhao and C. Lambert, Dynamics and control of a towed underwater vehicle system, Victoria: Ocean Engineering, 2003.

[24] T. Delmer, T. Stephens and J. Tremills, “Numerical Simulation of Cable-Towed Accoustic Arrays,” *Ocean Engineering,* pp. 511-548, 1988.

[25] J. Gobat and M. Grosenbaugh, “Time-domain numerical simulation on ocean cable structures,” *Ocean Engineering,* pp. 1373-1398, 2005.

[26] R. M. Kennedy, “Crosstrack dynamics of long cable towed in the ocean,” Naval Underwater Systems Center, Fort Lauderdale.

[27] J. Ketchman and Y. Lou, “Application of the Finite Element Method To Towed Cable Dynamics,” *IEEE Ocean,* pp. 98-107, 1975.

Appendix A

Post processing of Experimental Data

Table A.1 Raw data and reference

turn #	run #	start time (GMT)	end time (GMT)	length [m]	radius [m]	st.d	Tow-in Angle [deg]	st.d	Tow Speed [m/s]	st.d	Tow force [N]	st.d
1	1	13:31:00	13:31:30	43	28.5	2.52	32	2.0	1.35	0.008	40.6	0.091
2	1	13:31:55	13:32:25	43	22.36	0.872	40	2.0	1.13	0.010	31.9	0.353
3	2	13:36:21	13:36:51	43	32.2	3.21	25	2.0	1.37	0.010	49.5	0.862
4	2	13:38:03	13:38:33	43	42.7	2.21	25	2.0	1.5	0.008	54.3	0.252
5	3	13:41:15	13:41:45	43	21.2	0.798	47	3.0	1.25	0.015	29	0.167
6	4	13:51:07	13:51:57	43	28.3	1.64	35	2.0	1.27	0.006	43.3	0.720
7	5	13:55:20	13:55:50	43	12.7	1.04	60	3.0	1.08	0.025	22.2	1.460
8	5	13:55:50	13:56:33	43	15.6	0.273	59	3.0	1.08	0.011	20.9	1.740
9	6	13:58:39	13:59:09	43	19.1	1.18	48	3.0	1.24	0.015	28.5	0.198
10	7	14:03:03	14:03:33	43	19.5	1.01	50	3.0	1.28	0.014	29	0.107
11	7	14:04:40	14:05:10	43	20	1.36	37	2.0	1.17	0.008	38.7	0.453
12	11	14:33:20	14:33:50	28	25.2	1.75	28	2.0	1.3	0.013	31.3	0.374
13	12	14:37:58	14:38:35	28	49.9	0.8	20	1.0	1.48	0.005	39.7	0.183
14	13	14:40:51	14:41:26	28	20.1	0.848	38	2.0	1.22	0.003	26.3	0.218
15	13	14:42:15	14:42:45	28	14.67	0.723	54	3.0	1.11	0.007	20.8	1.340
16	13	14:42:48	14:43:28	28	17.7	0.43	43	2.0	1.07	0.013	23.5	0.826
17	14	14:47:10	14:47:40	28	50.1	1.41	18	1.0	1.45	0.008	39.9	0.037
18	14	14:49:45	14:50:15	28	44.1	1.51	18	1.0	1.49	0.006	43.5	1.520
19	15	14:54:15	14:54:45	28	20	1.89	46	3.0	1.2	0.010	22.3	0.378
20	16	15:02:06	15:02:30	28	24.8	0.63	22	1.0	1.19	0.001	35.7	0.463
21	16	15:03:57	15:04:30	28	41.1	0.521	18	1.0	1.43	0.008	43.8	0.541
22	17	15:09:46	15:10:15	28	22.5	1.43	39	2.0	1.25	0.010	24.7	0.259
23	18	15:16:19	15:16:50	15	31.6	0.847	20	1.0	1.41	0.006	21.1	0.021
24	19	15:19:02	15:19:30	15	15.6	0.586	43	2.0	1.06	0.002	15.6	0.126
25	19	15:19:35	15:20:05	15	16.2	0.772	40	2.0	1.08	0.005	15.49	0.264
26	21	15:28:45	15:29:15	15	19.9	0.714	28	2.0	1.21	0.010	17.4	0.246
27	21	15:26:33	15:27:03	15	39.3	2.71	17	1.0	1.41	0.001	23.1	0.286

The complete set of experimental data is presented in table A.1. The individual sample is identified by the 'turn #'. The 'run #' and start, end times will allow for the retrieval of the correct data source. The computed radius and tow speed, along with the GPS position and the force measurements, are available as time-series variables in Matlab data files. The tow-in angle is sourced in the relevant video file.

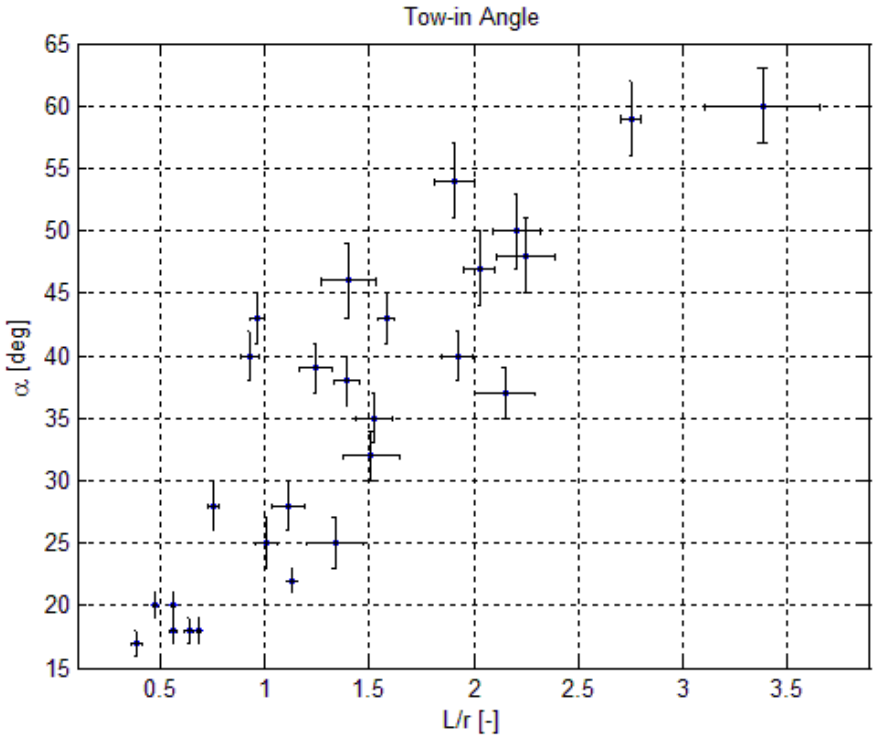

Figure A.1 Raw data: Tow-in angle

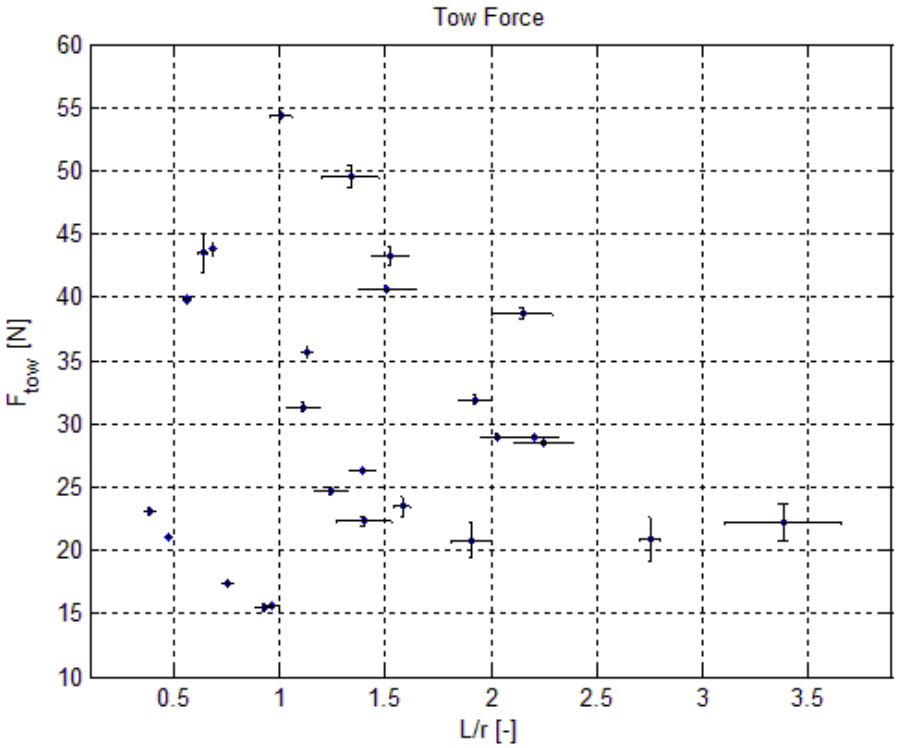

Figure A.2 Raw data: Tow force

Error Propagation for Derived Quantities

Each experimental quantity was recorded with a standard deviation. These uncertainties were passed on to all derived quantities using the following relation:

$$\sigma_G = \sqrt{\left(\sigma_a \frac{\partial G}{\partial a}\right)^2 + \left(\sigma_b \frac{\partial G}{\partial b}\right)^2 + \cdots}$$

$$\frac{L}{r}$$

$$\sigma_{L/r} = \sigma_r \frac{L}{r^2}$$

$$C_f = \frac{1.76 * F^{tow}}{1/2\, \rho A L U^2}$$

$$\sigma_{C_f} = \frac{2 * 1.76}{\rho A U^2} \sqrt{(\sigma_{F^{tow}})^2 + \left(\sigma_U \frac{2F^{tow}}{U}\right)^2}$$

$$F_n = \frac{F^{tow}}{r \cos\alpha}$$

$$\sigma_{F_n} = \frac{1}{r \cos\alpha} \sqrt{\left(\sigma_r \frac{F^{tow}}{r}\right)^2 + (\sigma_{F^{tow}})^2 + (\sigma_\alpha F^{tow} \tan\alpha)^2}$$

$$C_D = \frac{F_n}{1/2\, \rho T U^2 \sin^2\alpha}$$

$$\sigma_{C_D} = \frac{2}{\rho T U^2 \sin^2\alpha} \sqrt{(\sigma_{F_n})^2 + \left(\sigma_U \frac{2F_n}{U}\right)^2 + \left(\sigma_\alpha \frac{2F_n}{\tan\alpha}\right)^2}$$

Table A.2 Derived quantities & st. deviation

turn #	L/r [-]	st.d	F/F* [-]	st.d	C_D [-]	st.d
23	0.38168	0.02632	1.48077	0.02189	0.09545	0.01281
24	0.47468	0.01272	1.35256	0.01100	0.07924	0.00794
12	0.55888	0.01573	1.27476	0.01528	0.10948	0.01224
13	0.56112	0.00900	1.26837	0.01624	0.08569	0.00838
14	0.63492	0.02174	1.38978	0.05132	0.12841	0.01522
15	0.68127	0.00864	1.39936	0.02405	0.15062	0.01652
25	0.75377	0.02704	1.11538	0.01816	0.07478	0.01034
26	0.92593	0.04412	0.99295	0.01873	0.05476	0.00536
27	0.96154	0.03612	1.00000	0.01142	0.05281	0.00446
1	1.00703	0.05212	1.00000	0.00656	0.08733	0.01391
16	1.11111	0.07716	1.00000	0.01690	0.09203	0.01386
17	1.12903	0.02868	1.14058	0.02011	0.19992	0.01823
18	1.24444	0.07909	0.78914	0.01255	0.04896	0.00534
2	1.33540	0.13313	0.91160	0.01643	0.12656	0.02299
19	1.39303	0.05877	0.84026	0.01222	0.06401	0.00637
20	1.40000	0.13230	0.71246	0.01478	0.04130	0.00581
3	1.50877	0.13341	0.74770	0.00385	0.07682	0.01100
4	1.51943	0.08805	0.79742	0.01377	0.07958	0.00932
21	1.58192	0.03843	0.75080	0.02787	0.06881	0.00617
22	1.90866	0.09407	0.66454	0.04354	0.04852	0.00543
5	1.92308	0.07500	0.58748	0.00705	0.07463	0.00704
6	2.02830	0.07635	0.53407	0.00395	0.04517	0.00487
7	2.15000	0.14620	0.71271	0.00897	0.10771	0.01254
8	2.20513	0.11421	0.53407	0.00317	0.04269	0.00447
9	2.25131	0.13909	0.52486	0.00439	0.04850	0.00561
10	2.75641	0.04824	0.38490	0.03209	0.04314	0.00465
11	3.38583	0.27726	0.40884	0.02695	0.05515	0.00716

Calibration of Force Sensor

The force sensor was calibrated by loading it using calibration weights and recording the output voltage. The 250-Newton sensor was used to avoid any possible over-loading due to dynamic loads, which were poorly understood beforehand. The calibration curve is linear with a slope of 118.2 N/V.

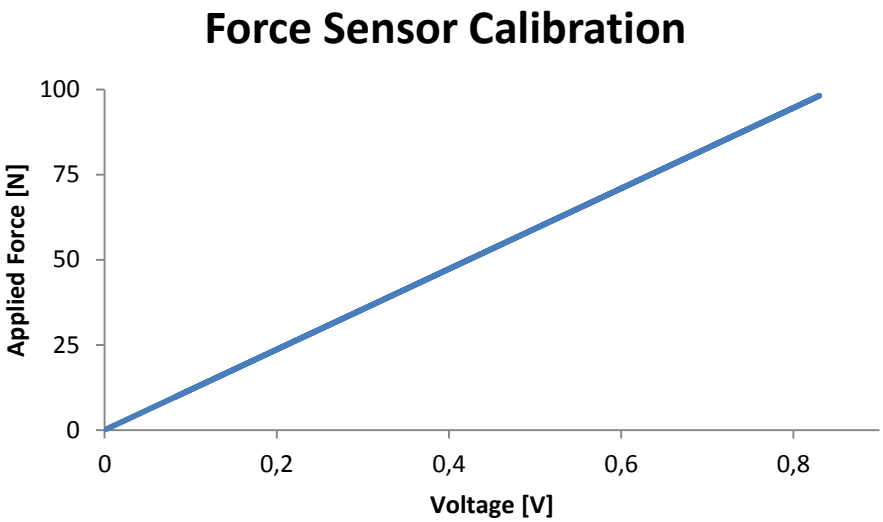

Figure A.3 Force Sensor Calibration

GPS Corrections for Atmospheric Interference

The GPS data underwent a post-processing designed to remove errors caused by atmospheric conditions. The process uses the same principle as DGPS, where a reference station records a high-quality GPS position and compares it with its known position. The GPS system uses the time required for electro-magnetic signals to travel between satellites and the antenna to calculate position. Varying atmospheric conditions cause minute variations in signal speed, giving an error in the position. The deviations found for the reference position are used to correct the raw GPS data trace for these atmospheric irregularities. The reference station is on the TU Delft campus, approximately 40 km north of the test site. The corrected position has a standard deviation of approximately 5 cm. It is assumed to be exact.

Appendix B

Matlab Code

Main Code

```
%-------------------------------------------------------------------------%
delete('config.mat','post.mat')

arc_subD = 25;    %number of links per uturn

am= 1;
r= .048;


rhoa= .707;
dr= r*1.3338069;
sa= r*3.822271062;

Cd= 0.09;
Cf= 0.065;
gain= 1000;


l_rarr= linspace(2,8,5);
pr_= 60;

ltot = 30;                                %absorbent length

U=1;
t_f= 1000;
n_arc= arc_subD;
save('config.mat'); %save('f_reduce.mat');

for w=1:length(l_rarr)

        disp(['freduce: w=' num2str(w)])

r_c = ltot/l_rarr(w);                        %length of pivot arm, radius of turn
n=ceil((ltot/r_c)*(n_arc/pi))

save('config.mat','r_c','n','-append')
```

```
[Y,T]= controlApproach(U,pr_,ltot,n,Cd,Cf,am,r,dr,t_f,rhoa,sa,gain);
[qdq_,f_,t_0]= CpostproApp(Y,T,pr_);
clear T Y DT
au_chek(w)=qdq_(n+2);

pr_U= f_;
[Y,T]= controlUturn(U,r_c,pr_U,ltot,n,Cd,Cf,am,r,dr,qdq_,t_0,t_0+t_f,rhoa,sa,gain);
[qdq_,f_1,t_1]= CpostproU(Y,T,pr_U);
clear T Y DT

f_s(w)=f_;
f_U(w)=f_1;
u_chek(w)=qdq_(n+2)*r_c;

pr_sa= f_1;
[Y,T]=
controlSailAwayf_r(U,r_c,pr_sa,ltot,n,Cd,Cf,am,r,dr,qdq_,t_1,t_1+t_f,rhoa,sa,gain);
[qdq_,t_2,f_2,f_hump]= CpostproSA(Y,T,pr_sa);
clear T Y DT

f_HUMP(w)=f_hump;
f_sa(w)= f_2;
sau_chek(w)=-qdq_(n+2);

close all

run postprobatch.m

run checkT.m
%store results in structured array%
FREDdata.TOWIN.(['i' num2str(w)])= towin';
FREDdata.VTAIL.(['i' num2str(w)])= v_tail;
FREDdata.FORCE.(['i' num2str(w)])= f;
FREDdata.TIME.(['i' num2str(w)])= t;
FREDdata.TIS.(['i' num2str(w)])= tis;
FREDdata.Y.(['i' num2str(w)])= y;
FREDdata.T.(['i' num2str(w)])= Tension;
save('f_reduce.mat','FREDdata','-append')
end
%-------------------------------------------------------------------------
```

U-turn

```
function [Y,T]= controlUturn(U,r_c,pr_U,ltot,n,Cd,Cf,am,r,dr,qdq_,t_,t_f,rhoa,sa,gain)

%% Model Setup
theta_c = 0;                %Initial state of pivot arm

%% Absorbent Properties

rhow =  1000;               %density of sea water
dl = ltot/(n);              %segment length
mass = (1+am)*rhoa*pi*r^2*rhow*dl;   %linear mass density of absorbent
an = dr*dl;                  %Normal Area
at = sa*dl;    %Tangential (surface) Area
At = (1/2)*rhow*at*Cf;
An = (1/2)*rhow*an*Cd;
```

```
%% STAGE I: U:Turn

% Define constant matrices & pre-allocate
L = ones(n).*dl; L(:,1) = ones(n,1).*r_c;
m = zeros(n);
ut = zeros(n);
lt = zeros(n);
for j = 1:n
    m(j,1:j-1) = (n-j+1)*mass;
    m(j,j:end) = (n+1-j:-1:1).*mass;
    lt(j,1:j) = ones(1,j);
    ut(j,j:n) = ones(1,n-j+1);
end
clear j
lt(1,1)=0;
Pr= zeros(n,1);

%% I.C.
q_ = [0,qdq_(2:n),0]';
dq_= qdq_(n+2:end)';
dq_(1)= qdq_(n+2)/r_c;

%% ODE
options = odeset('maxstep',1/30,'OutputFcn',@odeplot,'OutputSel',[1
n+1],'Vectorized','off','Stats','off','Events','EVENTSU');
[T,Y] = ode23s(@uturn,[t_,t_f],[q_;dq_],options);

%-------------------------------------------------------------------------
function dqddq = uturn(t,qdq)
q= qdq(1:n); dq= qdq(n+2:end-1);
%
ep= gain*(U/r_c-dq(1));
Pr(1)= r_c*pr_U*(1+ep);
%
Theta= q;
Th1 = zeros(n);
for k = 1:n
Th1(k,:)= Theta';
end
Th2= Th1.';  delTh= Th2-Th1;

M= m.*L.*L.'.*cos(delTh);

Ps= L.'.*sin(delTh).*ut;
Pc= -L.'.*cos(delTh).*ut;

Ft= At.*(L.*sin(delTh).*lt);
Fn= An.*(L.*cos(delTh).*lt);

dqddq(1:n,1)= dq;
dqddq(n+1,1)= 1+ep;
%
dqddq(n+2:2*n+1,1)= M'*Pr+M'*(Pc*Fn+Ps*Ft)*dq;
dqddq(2*n+2)=0;
%
end
%-------------------------------------------------------------------------
end
```

PostProU

```
function [qdq_,f_1,t_1]= CpostproU(Y,T,pr_U)
qdq_= Y(end,:);
t_1= T(end);

load config.mat; load post.mat;

DT= diff(T);
dimy=size(Y,1);
EPS= Y(:,n+1);
Y=[zeros(dimy,1),Y(:,1:n),zeros(dimy,1),Y(:,n+2:end-1)];

%% make constant sample rate
index= ones(5000,1);
time= 0; nstep= 2;
fps= 30;
frameT= 1/fps;
for i=1:length(DT)
   time= time+DT(i);
   tmark= nstep*frameT;
   if time >= tmark
       index(nstep)=i;
       nstep= nstep+1;
   end
end

index= index(1:nstep-1);
eps=EPS(index);
tis=(Y(index,2)-Y(index,3)-pi/2).*(180/pi);
f= [f;pr_U/2.*(diff(eps)./frameT)];
t= [t;T(index)];
y= [y;Y(index,:)];
f_1=f(end);
clear Y T DT index
save('post.mat','t','y','f','tis','n')
%--------------------------------------------------------------------------
```

Sail-Away

```
function [Y,T]=
controlSailAway(U,r_c,pr_,ltot,n,Cd,Cf,am,r,dr,qdq_,t_,t_f,rhoa,sa,gain)
%% Absorbent Properties

rhow =  1000;                %density of sea water
dl = ltot/(n);               %segment length
mass = (1+am)*rhoa*pi*r^2*rhow*dl;   %linear mass density of absorbent
an = dr*dl;                   %Normal Area
at = sa*dl;    %Tangential (surface) Area
At = (1/2)*rhow*an*Cf;
An = (1/2)*rhow*at*Cd;

%% STAGE II: Sail Away

p = n-1;                %number of angles
L = ones(p).*dl;    l = L(1,:);
```

```
% Define constant matrices & pre-allocate
m = zeros(n);
for j=1:n
    m(j,1:j-1) = (n-j+1)*mass;
    m(j,j:end) = (n+1-j:-1:1).*mass;
end
ut = zeros(p);
lt = zeros(p);
for j = 1:p
    lt(j,1:j) = ones(1,j);
    ut(j,j:p) = ones(1,p-j+1);
end
clear j
Pr= zeros(n,1);

%% I.C.

q_= [0,qdq_(2:n),0]';
dq_= qdq_(n+2:end)';
dq_(1)= -dq_(1)*r_c;
t_i= t_;


%% ODE
options = odeset('maxstep',1/30,'OutputFcn',@odeplot,'OutputSel',[1
n+1],'Vectorized','off','Stats','on','Events','EVENTSSA');
[T,Y] = ode23s(@sailaway,[t_i,t_f],[q_;dq_],options);

%% ---------------------------------------------------------------------
function dqddq = sailaway(t,qdq)
q= qdq(1:n); dq= qdq(n+2:end-1);

%
ep= gain*(U+dq(1));
Pr(1) = -pr_*(1+ep);
%

Theta= q(2:end);
Th1 = zeros(p);
for k = 1:p
Th1(k,:)= Theta';
end
Th2= Th1.';  delTh= Th2-Th1;

M= m.*[1,   l.*cos(Theta'); ...
       l'.*cos(Theta),   L.*L.'.*cos(delTh)];

Ps= L.'.*sin(delTh).*ut;  Ps= [0,  -ones(1,p); ...
                               zeros(p,1),   Ps];

Pc= -L.'.*cos(delTh).*ut;  Pc= [0, -ones(1,p); ...
                               zeros(p,1),   Pc];

Ft= At.*(L.*sin(delTh).*lt);   Ft= [0, zeros(1,p); ...
                                    At.*sin(Theta),   Ft];

Fn= An.*(L.*cos(delTh).*lt);  Fn= [0,zeros(1,p); ...
                                   An.*cos(Theta),   Fn];
%
```

```
dqddq(1:n,1)= dq;
dqddq(n+1,1)= 1+ep;
%
dqddq(n+2:2*n+1,1)= M'*Pr+M'*(Pc*Fn+Ps*Ft)*dq;
dqddq(2*n+2)=0;
%
end
%-------------------------------------------------------------------------
end
```

PostProSA

```
function [qdq_,t_2,f_2,f_hump]= CpostproSA(Y,T,pr_sa)
qdq_= Y(end,:);
t_2= T(end);

load config.mat; load post.mat;

DT= diff(T);
dimy=size(Y,1);
EPS= Y(:,n+1)-Y(1,n+1);
Y=[Y(:,1),pi*ones(dimy,1),Y(:,2:n),Y(:,n+2),zeros(dimy,1),Y(:,n+3:end-1)];

%% make constant sample rate
index=ones(5000,1);
time=0; nstep=2;
fps=30;
frameT= 1/fps;
for i=1:length(DT)
   time= time+DT(i);
   tmark= nstep*frameT;
   if time >= tmark
       index(nstep)=i;
       nstep=nstep+1;
   end
end
index=index(1:nstep-1);
t_ti= T(index);
x_ti= Y(index,1);
ti=(Y(index,2)-Y(index,3)-pi/2).*(180/pi);
s=find(ti<1);
if numel(s) >0
    ti=ti(1:s(1));
    t_ti= t_ti(1:s(1));
    x_ti= x_ti(1:s(1));
end

towi= [x_ti*(-1),t_ti-t_ti(1),ti];
eps=EPS(index);
f_a= smooth(pr_sa*(diff(eps)./frameT),120);
f_hump= max(f_a(6:end/2));
f_2= f_a(ceil(5*end/6));
f= [f;pr_sa*(diff(eps)./frameT)];
t= [t;T(index)];
y= [y;Y(index,:)];
```

```
clear Y T DT index
save('post.mat','t','y','n','f','towi','tis')
```

CheckT

```
%-------------------------------------------------------------------------%
%non-contributing forces
 %clear all;
 load config.mat
n=n-1;
Tension= zeros(size(y,1),n); DDQ= zeros(size(y,1)-1,n);
%% Set up matrices

rhow =  1000;                %density of sea water
dl = ltot/(n);               %segment length
mass = (1+am)*rhoa*pi*r^2*rhow*dl;   %linear mass density of absorbent
an = dr*dl;                  %Normal Area
at = sa*dl;                  %Tangential (surface) Area
At = (1/2)*rhow*at*Cf;
An = (1/2)*rhow*an*Cd;

% Define constant matrices & pre-allocate
L = ones(n+1).*dl; L(:,1) = ones(n+1,1).*r_c;
l=L(1,:);
m = zeros(n);
ut = zeros(n);
lt = zeros(n);
for j = 1:n
     m(j,1:j-1) = (n-j+1)*mass;
     m(j,j:end) = (n+1-j:-1:1).*mass;
    lt(j,1:j) = ones(1,j);
    ut(j,j:n) = ones(1,n-j+1);
end
ut(1,1)=2;
lt= [ones(n,1),lt];

%% find accel

for k=1:n
    ddqraw= diff(y(:,k+n+2))./diff(t);
    DDQ(:,k)= smooth(ddqraw,2);
end

for c= 2:size(y,1)-1
    ddq= DDQ(c,:)';
    dq= y(c,n+3:end)';
    q= y(c,1:n+2)';

Th1 = zeros(n+1);
for k = 1:n+1
Th1(k,:)= q(2:n+2);
end
Th2= Th1.';  delTh= Th2-Th1;

M= m.*L(2:end,2:end).*sin(delTh(2:end,2:end));

Pt= cos(delTh(2:end,2:end)).*ut;
Pn= sin(delTh(2:end,2:end)).*ut;
```

```
Ft= At.*(L(2:end,:).*sin(delTh(2:end,:)).*lt);
Ftdq= [At.*sin(q(3:n+2)),   Ft]*dq;

Fn= An.*(L(2:end,:).*cos(delTh(2:end,:)).*lt);
Fndq= [An.*cos(q(3:n+2)),   Fn]*dq;

tcheck= -(M*ddq+Pt*Ftdq+Pn*Fndq);

Tension(c,:)= tcheck;
end
Tension= Tension(3:end-1,:);
%--------------------------------------------------------------------------
```